A DUAL-POLARISED ARRAY ANTENNA USING AEP-DNN TECHNIQUE FOR BEAM-STEERING IN MILLIMETER WAVE APPLICATIONS

BY

SITI ZAINAB MOHD HAMZAH

A thesis submitted in fulfilment of the requirement for the degree of Doctor in Philosophy in Engineering

Kulliyyah of Engineering
International Islamic University Malaysia

AUGUST 2025

ABSTRACT

Nowadays, the evolution of wireless networks has become increasingly robust due to rising demands. Notably, one key feature of 5G is its capacity to offer broader coverage of received signals. Polarization diversity can be used to improve received signal coverage and mitigate link drop caused by polarization mismatch. In this study, a novel approach uses a single feeding port to simultaneously excite dual linearly polarised patch antenna array (DLPAA) at 28 GHz. Antenna array optimization involves pattern synthesis to achieve the desired radiation pattern of the proposed DLPAA. Currently, full-wave and conventional optimization tools are usually used to synthesise an antenna array, which makes the design slow and computationally expensive. This could lead to high inaccuracy in array synthesis especially when the antenna is highly sensitive in millimeter-waves. Deep learning algorithms map input features and target variables, automatically adjusting parameters based on known pairs. The project aims to develop active element pattern and deep neural network (AEP-DNN) algorithms to improve antenna array synthesis efficiency and reliability. Therefore, this study has led to three research objectives; the work begins with the design of dual-polarised antennas operating at 28 GHz. This is followed by the synthesis of a proposed DLPAA using the AEP-DNN method to enable beam-steering capabilities. This method is proposed because it demonstrates faster convergence, improved pattern prediction accuracy for large input datasets, reduces simulation costs and computational complexity while increasing overall learning efficiency. Finally, the antennas are fabricated and the algorithm is verified through testing. The proposed DLPAA is a 1×4 linear array (62.45 × 23.08 × 1.575 mm^3) with 15.60 mm spacing. Simulated in CST, it achieves S_{11} of –13 dB per port, with measured values ranging from –11.57 dB to –35.23 dB. The proposed DLPAA achieves these values through optimized impedance matching, dual-polarised design, and careful array configuration. The simulated co-polarised gains are improved from 12.10 dBi to 14.40 dBi (elevation) and 12.00 dBi to 13.10 dBi (azimuth). Although some discrepancies exist between simulated and measured results is due to fabrication or instrument errors, the performance remains acceptable. The AEP-DNN method, implemented in MATLAB, successfully steered beams to 0°, 5°, 10°, 15°, and 20°, with the predicted DNN patterns aligning well with the desired main lobe directions. RMSE values converged to approximately 1.5 (training) and 1.3 (validation), while training and validation losses reached minimums of 2.1–2.3 and 1.7–1.9, respectively. The method has been effectively applied for pattern synthesis and verified through both CST simulations and measurements on the fabricated antenna.

ملخص البحث

في الوقت الحاضر، يشهد تطور الشبكات اللاسلكية تقدماً ملحوظاً نتيجة للطلب المتزايد عليها. ومن الجدير بالذكر أن إحدى الميزات الرئيسية لشبكات الجيل الخامس (5G) هي قدرتها على توفير تغطية أوسع للإشارات المستقبلة. ويمكن استخدام تنوع الاستقطاب لتحسين تغطية الإشارة المستقبلة والتقليل من انقطاع الاتصال الناتج عن عدم تطابق الاستقطاب. في هذه الدراسة، تم اقتراح نهج جديد يستخدم منفذ تغذية واحد لتحفيز مصفوفة هوائيات رقعية مزدوجة الاستقطاب الخطي (DLPAA) في الوقت نفسه عند تردد 28 GHz. ويتضمن تحسين مصفوفة الهوائيات توليف الأنماط لتحقيق نمط الإشعاع المطلوب لمصفوفة (DLPAA) المقترحة. ومن المعتاد حالياً استخدام أدوات تحسين الموجة الكاملة وأدوات التحسين التقليدية لتوليف مصفوفة الهوائيات، وهو ما يجعل التصميم بطيئاً ومكلفاً حسابياً، وقد يؤدي ذلك إلى درجة عالية من عدم الدقة في توليف المصفوفة، خاصةً عندما يكون الهوائي شديد الحساسية للموجات المليمترية. تقوم خوارزميات التعلم العميق (Deep learning) بربط خصائص الإدخال ومتغيرات الهدف، مع ضبط المعلمات تلقائياً بناءً على أزواج معروفة. ويهدف هذا المشروع إلى تطوير خوارزميات نمط العنصر النشط والشبكات العصبية العميقة (AEP-DNN) لتحسين كفاءة توليف مصفوفات الهوائيات وموثوقيتها. لذلك، أسفرت الدراسة عن ثلاثة أهداف بحثية؛ إذ يبدأ العمل بتصميم هوائيات مزدوجة الاستقطاب تعمل عند تردد 28 GHz، يلي ذلك تركيب (DLPAA) مقترح باستخدام طريقة (AEP-DNN) لتمكين توجيه الشعاع. تم اقتراح هذه الطريقة لأنها تؤدي إلى تقارب أسرع ودقة أفضل في التنبؤ بالأنماط لمجموعات بيانات الإدخال الكبيرة، كما أنها تقلل من تكاليف المحاكاة وتعقيد العمليات الحسابية، بينما تؤدي إلى زيادة كفاءة التعلم الإجمالية. وأخيراً، تم تصنيع الهوائيات والتحقق من صحة الخوارزمية من خلال الاختبارات. والمصفوفة المقترحة (DLPAA) هي مصفوفة خطية 1×4 (بأبعاد 62.45 × 23.08 × 1.575 مم^3) مع تباعد 15.60 مم. وعند محاكاتها باستخدام برنامج (CST)، تم تحقيق معامل انعكاس (S_{11}) بقيمة 13 dB– لكل منفذ، بينما تراوحت القيم المقاسة بين 11.57 dB– و 35.23 dB–. وقد حققت مصفوفة (DLPAA) المقترحة هذه النتائج من خلال تحسين مطابقة المعاوقة، وتصميم مزدوج الاستقطاب، وتكوين المصفوفة بعناية. كما تم تحسين مكاسب الاستقطاب المتطابق من 12.10 dBi إلى 14.40 dBi (رأسياً) ومن 12.00 dBi إلى 13.10 dBi (أفقياً). وعلى الرغم من وجود بعض التباينات بين نتائج المحاكاة والنتائج المقاسة نتيجةً لأخطاء في التصنيع أو في أدوات القياس، إلا أن الأداء لا يزال مقبولاً. وتم تطبيق طريقة (AEPDNN) باستخدام برنامج (MATLAB)، حيث نجحت في توجيه الشعاع إلى الزوايا 0°، 5°، 10°، 15°، و 20°، وتطابقت أنماط (DNN) المتوقعة مع اتجاهات الشعاع الرئيسي المطلوبة. وصلت قيم الجذر التربيعي لمتوسط الخطأ (RMSE) إلى نحو 1.5 (للتدريب) و 1.3 (للتحقق)، بينما وصلت خسائر التدريب والتحقق إلى حد أدنى يتراوح بين 2.1–2.3 و 1.7–1.9 على التوالي. وقد تم تطبيق هذه الطريقة بفعالية لتوليف النمط وتم التحقق منها من خلال كل من محاكاة (CST) والقياسات الفعلية على الهوائي المصنع.

APPROVAL PAGE

The thesis of Siti Zainab Mohd Hamzah has been approved by the following:

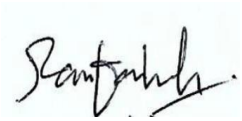

Norun Farihah Abd Malek
Supervisor

Sarah Yasmin Mohamad
Co-Supervisor

Md. Rafiqul Islam
Internal Examiner

Khaizuran Bin Abdullah
Internal Examiner

Mohd Haizal Bin Jamaludin
External Examiner

Akram M Z M Khedher
Chairman

DECLARATION

I hereby declare that this thesis is the result of my own investigations, except where otherwise stated. I also declare that it has not been previously or concurrently submitted as a whole for any other degrees at IIUM or other institutions.

Siti Zainab Mohd Hamzah

Signature  Date 20 AUGUST 2025

INTERNATIONAL ISLAMIC UNIVERSITY MALAYSIA

DECLARATION OF COPYRIGHT AND AFFIRMATION OF FAIR USE OF UNPUBLISHED RESEARCH

A DUAL-POLARISED ARRAY ANTENNA USING AEP-DNN TECHNIQUE FOR BEAM-STEERING IN MILLIMETER WAVE APPLICATIONS

I declare that the copyright holders of this thesis are jointly owned by the student and IIUM.

By signing this form, I acknowledged that I have read and understand the IIUM Intellectual Property Right and Commercialization policy.

Affirmed by Siti Zainab Mohd Hamzah

…….. 20 AUGUST 2025

Signature Date

This thesis is dedicated to my late father for laying the foundation of what I turned out to be in life.

ACKNOWLEDGEMENTS

All praise belongs to Allah, the Most High, whose infinite Grace and Mercy have accompanied me every step of this journey. Though the path was often steep and demanding, His divine favor continually lightened the burden and gave me strength to see this thesis through to completion.

I am profoundly grateful to my supervisor, Assoc. Prof. Dr. Norun Farihah Abd Malek, whose unwavering guidance, patience, and insightful mentorship have been instrumental to this work. Her precision, kindness, and thoughtful inquiries sharpened my focus and enriched the substance of this thesis. I deeply value her timely feedback, constructive suggestions, and the generous time she devoted despite her many responsibilities. Her encouragement, both academic and moral, became a steady force behind my perseverance.

I also extend my sincere appreciation to my co-supervisors, whose valuable input and support played a vital role in shaping the outcome of this research.

My heartfelt thanks go to my family—especially my mother, my husband, and our dear child—whose prayers, love, and quiet sacrifices have been my source of strength. Their patience and support while I was away did not go unnoticed.

Above all, I bow in gratitude to Allah once again—for it is only through His boundless mercy that I have reached this milestone. May this effort be accepted as a small act of devotion. Alhamdulillah!

TABLE OF CONTENTS

LIST OF TABLES

LIST OF FIGURES

LIST OF ABBREVIATIONS

1G	1 Generation
2G	2 Generation
3G	3 Generation
4G	4 Generation
5G	5 Generation
ADAM	Adaptive Moment Estimation
AEP	Active Element Pattern
AF	Array Factor
AI	Artificial Intelligence
ASCII	American Standard Code for Information Interchange
AUT	Antenna Under Test
BSPA	Bone-Shaped Patch Antenna
CATR	Compact-Antenna-Test-Range
CEM	Computational Electromagnetics
CNN	Convolutional Neural Network
CPU	Center Processing Unit
CST	Computer Simulation Technology
DE	Differential Evolution
DLPAA	Dual-Linearly Polarised Antenna Array
DNN	Deep Neural Network
FDTD	Finite-Difference Time-Domain
GA	Genetic Algorithm
GAN	Generative Adversarial Network
GDA	Greedy Algorithm
GUI	Graphical User Interfaces
HFSS	High Frequency Simulation Software
IoT	Internet of Things
LAN	Local Area Network
LMS	Least Mean Square
MA	Metropolis Algorithm
MATLAB	Matrix Laboratory
MGSA	Modified Version of The Gravitational Search Algorithm
MIMO	Multiple-Input-Multiple-Output
MLP	Multilayer Perceptron
MOM	Method of Moments
MPA	Microstrip Patch Antenna
MSE	Mean-Square Error
NLMS	Normalized Least Mean Square
OMP	Orthogonal Matching Pursuit
OTA	Over-The-Air

PALM	Precise Augmented Lagrange Multiplier
PCB	Printed Circuit Board
PIFA	Planar Inverted-F Antenna
PMM	Pattern Multiplication Method
PSO	Particle Swamp Optimization
ReLU	Rectified Linear Unit
RF	Radio Frequency
RLS	Recursive Least Square
RMSE	Root-Mean-Square-Error
SADEA	Surrogate Model Assisted Differential Evolution for Antenna
SCO	Sequential Convex Optimizations
SEP	Single Element Pattern
SIW	Substrate Integrated Waveguide
SMA	Sub Miniature Version A
SMI	Sample Matrix Inversion
SNR	Signal-To-Noise Ratio
VNA	Vector Network Analyzer
WiFi	Wireless Fidelity

LIST OF SYMBOLS

S_{11}	Reflection Coefficient
I	Amplitude
Θ	Theta Angle
Φ	Phi Angle
Φ	Phase Angle
B	Phase Shift Difference
E	Electric Field
H	Magnetic Field

CHAPTER ONE

INTRODUCTION

1.1 BACKGROUND

Wireless communication is essential in enabling simple communication worldwide in the present era. This method of wireless communication transmits data without using wires or electrical cables such as fibre optics. Wireless communication is a convenient way to share information with the technology-savvy generation. A person could move around without fear of losing their internet connection. Wireless communication technology offers many advantages such as cost efficiency, adaptability, convenience, speed, accessibility, and uninterrupted connectivity. Minimal physical infrastructure in wireless networks results in lower costs. Individuals could communicate with each other regardless of their location, like miners in isolated areas who could still connect with others through a satellite phone, showcasing their adaptability. A simple tool like a mobile phone is necessary for staying connected and readily accessible. Network connectivity and accessibility saw noticeable enhancements in both accuracy and speed. Uninterrupted connectivity could also help people quickly deal with emergencies.

Different types of wireless communication technologies consist of radio and TV broadcasting, radar communication, satellite communication, cellular communication, global positioning system, Wireless Fidelity (WiFi), Bluetooth, and radio frequency identification. The main emphasis of this research is on cellular networks. Cellular networks involve a setup of cellular towers, base stations, and mobile users could determine the sending and receiving of signals by triangulating to the preferred antenna. A rapid growth of wireless cellular networks has garnered considerable interest, especially.

The worldwide wireless cellular networks sector has extensively studied fifth-generation wireless technology, also known as "5G", in diverse industries and research institutions. This latest wireless standard follows 1G, 2G, 3G, and 4G networks. 5G enables

a higher level of connectivity that aims to connect nearly everyone and everything, including machines and devices. 5G is a crucial goal for the 21st century, offering benefits and improving multiple areas of our everyday lives such as economic development, schooling, jobs, transportation, electricity networks, healthcare facilities, manufacturing, and so forth (Kaeib et al., 2019). The increasing demand for activities such as watching videos on platforms like "YouTube" and saving data online is fuelling the requirement for 5G, as these activities are not supported by 4G. 2G networks were developed for voice communication, 3G for voice and data, 4G for rapid web browsing, and 5G facilitates extensive connectivity with an emphasis on Internet of Things (IoT). Due to limitations in 4G, 5G wireless technologies have the ability to reduce latency by milliseconds, improve data speed transfer by 10 Gbps, and support connectivity with 100 billion wireless devices (M. Y. Mohamed et al., 2020). 5G is divided into three frequency bands: low band (600-700 MHz), mid band (2.6 GHz & 3.3-4.98 GHz), and high band (26 & 28 GHz) (Ghaderi & Amiri, 2023).

Meeting these requirements could potentially be accomplished by the outstanding performance of the recommended antenna in terms of both design and optimization. Designing an antenna includes the structure of the antenna, method of feeding, selection of materials, and fabrication methods. To meet the requirements of 5G wireless technology, antennas need to be lightweight, cost-effective, compact, high-gain, and efficient (Parchin et al., 2019). The antenna for mobile device users ought to be designed to be small in size. The height and width of a small antenna are relative to its overall size. Moreover, phased antenna arrays are preferred due to their ability to improve gain performance and assist in beam-steering capabilities.

A phased antenna array is made up of radiating elements arranged in an array, enabling electronic adjustment of the shape and direction of the radiation pattern without physically moving the antenna. This happens when every antenna element in the array transmits on one frequency, but with a distinct phase difference among them. Therefore, a large number of antenna elements are arranged closely together to produce a compact antenna array configuration. Giving careful consideration to where antenna elements are positioned is crucial for ensuring optimal performance of the antenna. It is important to

choose inter-element spacing wisely to reduce the effects of mutual coupling. There are problems with the small antenna design caused by the mutual coupling effect. Mutual coupling effect refers to the electromagnetic interaction among antenna elements within an array, where one antenna's receiver absorbs energy when a neighbouring antenna is in operation.

Using machine learning, especially deep neural networks (DNNs), to design antennas is becoming more common because it could save time and handle complex problems better than traditional methods. But designing antennas at 28 GHz, which is in the millimeter-wave range, brings special challenges compared to lower 5G bands like sub-6 GHz. At 28 GHz, the wavelength is very short, so the antennas are small but also more sensitive. Small changes in size, shape, or position could cause big differences in performance. A high gain antenna is required for mobile devices to minimize the high path signal loss in free space at a frequency of 28 GHz in millimeter-wave communication. Phased antenna arrays also help in achieving high gain of radiation through beam steering. Figure 1.1 illustrates how a phased antenna arrays could direct beams to a specific location. The mobile device antenna needs to be able to steer the beam to adjust for its unpredictable positioning. Broad scanning range is preferred to maintain a strong connection in challenging environments like densely populated areas. Broad scanning coverage refers to the wide range of signals emitted and encompassed by the beam radiation coming from the antenna (Deng et al., 2020). Therefore, the antenna should send signals in very focused directions using beam-steering.

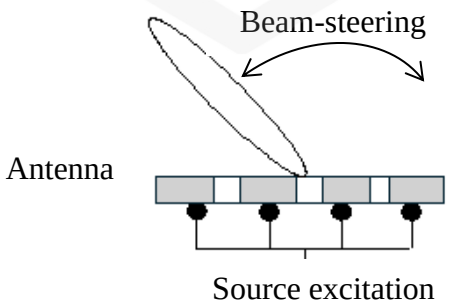

Figure 1.1 Beam-Steering of Four Radiating Elements

(Kouhalvandi & Matekovits, 2024)

Nevertheless, a high gain antenna would lead to a narrower beamwidth pattern, resulting in a decrease in signal coverage within line-of-sight. Design and implementation require consideration of the trade-off between gain and beamwidth coverage, particularly for mobile terminals. Therefore, a narrow beamwidth signal could be overcome by steering the beam in order to achieve broad scanning coverage. This is why phased antenna arrays are favoured, as they are able to cover multiple angular ranges to combat the decreased gain. Nonetheless, utilizing a phased antenna array containing numerous radiating elements would result in higher expenses for the system.

Traditional design methods like full-wave simulations take a long time and require a lot of computing power, especially when dealing with many antenna elements and phase shifts. They are not practical for fast or real-time use. Machine learning helps solve these problems, but it also has some challenges, especially at millimeter-wave frequencies, such as it needs a large and accurate dataset to train the model properly. The model might not work well if used with a different antenna or frequency unless retrained. It is often hard to understand how the model makes its decisions. As the antenna array gets bigger, the model becomes harder to train and manage. At 28 GHz, the environment is much tougher, so machine learning becomes more important. It helps steer the beam quickly and accurately, even when the signal conditions change. In this study, the AEP-DNN method is proposed. It uses active element patterns (AEPs) as input instead of full simulations, which makes it faster and more efficient. This method gives good beam prediction results, uses smaller datasets, and works better with real antenna behavior.

Utilizing dual-polarised antennas could enhance polarization diversity in beam radiation without adding numerous radiating elements and expenses. Most previous antenna designs are limited to transmitting and receiving signals in just one polarization, leading to a loss of signal strength if the polarizations do not align. In contrast, dual-polarised antennas could send and receive signals in two polarizations at the same time, enabling communication with devices of varying polarization orientations. A dual-polarised antenna is an antenna with two distinct polarization directions, which enhance communication reliability and efficiency by adjusting to incoming signal polarization for stronger signal reception. Many research studies have been conducted on dual-polarised

antennas due to their ability to improve signal quality and mitigate link drops that caused by polarization mismatch between the transmitter and receiver.

In this research, a microstrip patch antenna is utilized to design a dual-polarised antenna array at 28 GHz. Microstrip patch antenna (MPA) is commonly used in wireless communication systems due to its low-profile, lightweight, affordable cost, conformal design, limited power handling capability, and simple integration and fabrication processes. Enhanced antenna performance could be achieved by designing them in various shapes (Midasala & Siddaiah, 2016).

Antenna pattern synthesis is when an algorithm is used to optimize the amplitude and phase weights of antenna parameters for radiation pattern synthesis. This research aims to explore and create a millimeter-wave antenna at 28 GHz while also generating a directed main beam to a specific location in order to enhance wide scanning angle and beam-steering capability. Adjusting the coefficient weights to achieve a specific radiation pattern in a preferred main beam direction is known as beam-steering.

In this study, antenna pattern synthesis has been carried out by using machine learning technique of deep neural network (DNN). The traditional optimization approach has encountered less competency in terms of the processing time, and reliability to conduct an enormous data for optimization process. Therefore, the DNN has been integrated with active element pattern (AEP) method to improve the processing time given a large amount of data. This method has been compared to the pattern multiplication method (PMM) and full-wave modelling tool, which is computer simulation technology (CST), to observe the proposed method's performance.

The proposed antenna has been fabricated to verify the simulation results of antenna performance in terms of the reflection coefficient, mutual coupling, and radiation pattern. The fabricated antenna array has also been measured to tune the phases of the antenna using a beamformer to observe the capability of the designed antenna to steer the main beam into a desired location.

1.2 PROBLEM STATEMENT AND SIGNIFICANCE

One way to achieve beam-steering capability, aside from electronic and mechanical methods, is through the use of an optimization technique. The millimeter-wave antenna is very sensitive to obstructions, orientation, and various other influences. It stresses the need for a more accurate optimization technique than the traditional method. Traditional optimization methods like full-wave modelling and pattern multiplication method are slowing down and impractical for handling large amounts of data (Ghaderi & Amiri, 2023). This could lead to significant errors in antenna pattern synthesis, especially in the higher frequency bands of 5G. Deep neural networks (DNNs) have been used for beam steering, standard implementations often require large datasets, have high computational cost, and lack robustness in capturing mutual coupling and active element behavior. These models could struggle with generalization when the array configuration or steering angles vary. The proposed AEP-DNN method, mitigates these issues by incorporating AEP values into the training process. This results in improved prediction accuracy, faster convergence, lower training complexity, and better scalability for large arrays.

The design of high-performance antenna systems for 5G networks is increasingly focused on the millimeter-wave band, particularly the 28 GHz spectrum, due to its potential for ultra-high data rates and low latency. However, antenna design at this frequency presents significant challenges compared to lower-band 5G platforms such as sub-6 GHz. These include increased free-space path loss, greater sensitivity to fabrication tolerances, and reduced signal penetration. As a result, antenna arrays should offer high gain, beam-steering capability, compact form dimension, and excellent polarization performance.

Many existing dual-polarised antennas suffer from poor isolation between ports, complex multi-feed structures, limited gain, and inadequate impedance matching, particularly at millimeter-wave frequencies like 28 GHz (Huang et al., 2022). These limitations lead to inefficient radiation, polarization mismatch, and high reflection coefficients, which degrade system performance. Moreover, most designs rely on multiple feeding ports, which increases fabrication complexity and cost. The proposed dual-linearly

polarised antenna array (DLPAA) addresses these issues by using a simplified single-feed structure, enhanced impedance matching, and improved port isolation which offering better gain and more compact implementation suitable for 5G devices.

There is a gap which further complicate their integration into machine learning frameworks that accounts for realistic antenna behavior while supporting the physical design needs of a dual-linearly polarised antenna array (DLPAA) for beam-steering. According to the explanation, it is required to design antenna that has the beam-steering capability (Younus et al., 2021). This study addresses these challenges by combining the AEP method with a DNN model, aiming to improve learning efficiency and pattern accuracy, while also proposing a practical DLPAA design optimized for 5G applications.

1.3 RESEARCH PHILOSOPHY

Dual-polarised antenna arrays are used to adjust the main radiation beam towards different directions without the need for physically moving the antenna. Beam-steering is vital for 5G and other applications. Training a deep neural network (DNN) in the AEP-DNN requires predicting or optimizing the excitation phase for each array element through data-driven methods. The DNN ensures that the expected beam pattern and prediction are achieved in various operational conditions. The reason from using AEP-DNN is to take advantage of neural networks' pattern recognition and optimization capabilities for complex electromagnetic problems. The AEP-DNN technique provides a new approach to enhance and control beam-steering, surpassing traditional methods in flexibility and efficacy. The DNN-based approach improves the ability to adapt in real-time. By automating beam-steering using artificial intelligence, the reliance on traditional optimization techniques like genetic algorithms or particle swarm optimization is reduced, resulting in faster real-time performance. It continuously enhances and fine-tunes the way the array reacts to fluctuating signal conditions, such as changes in interference or multipath effects, which traditional algorithms might struggle with. The research utilizes a method combining analytical

modelling and empirical testing, including simulations using tools like CST, to confirm the efficiency of the AEP-DNN-driven antenna array. These simulations validate that the DNN is able to effectively learn from training data and demonstrate high performance in challenging scenarios.

This study focuses on creating dual-polarised antenna arrays, crucial for applications needing polarization diversity. The dual-polarised phased antenna array enhances antenna performance by allowing for a wide beam scanning angle and array pattern synthesis, all while being cost-effective for 5G networks. The proposed idea could decrease the excessive path loss and interference occurring in the 28 GHz band. Dual polarization helps decrease signal loss caused by mismatched polarizations between the transmitter and receiver, thus avoiding lost connections. The modularity of the dual-polarised array, along with the flexibility of DNN-based optimization, allows this design approach to be easily scaled to larger, more complex arrays needed for upcoming communication systems such as 6G and beyond. The research philosophy acknowledges the increasing demand for flexible, smart systems in ever-changing surroundings, getting ready for upcoming uses like intelligent urban areas, Internet of Things, and artificial intelligence-based communication networks.

1.4 RESEARCH QUESTIONS

1. What types of dual polarization techniques are suitable for high-frequency bands in 5G?
2. What are the limitations of the conventional optimization techniques for pattern synthesis?
3. How could the reliability of the proposed method and preferred antenna design be justified?

1.5 RESEARCH OBJECTIVES

The dual-polarised phased antenna array is able to achieve optimal performance of antennas in promoting a wide beam scanning angle and array pattern synthesis while reducing the cost and time-consuming for 5G networks for beam-steering capability. This study comes up with three objectives as follows:

1. To design and develop a single dual-polarised antenna and the dual-linearly polarised antenna array (DLPAA) with a simple single layer structure at 28 GHz.
2. To develop an algorithm using the AEP-DNN method for pattern synthesis and validate it using the conventional method (pattern multiplication method) and full-wave modelling (CST tool).
3. To fabricate and perform measurement setup in order to validate the simulation results and AEP approach.

1.6 RESEARCH HYPOTHESES

The AEP-DNN technique could greatly enhance the accuracy and efficiency of beam-steering for dual-polarised antenna arrays when compared to conventional methods. Using the AEP-DNN method, dual-polarised antenna arrays could enhance signal-to-noise ratio (SNR) and decrease interference through polarization diversity, particularly in settings with multi-path interference. The optimized and adaptive neural network configurations of the AEP-DNN method allow for quicker response times in real-time beam-steering applications. Antenna arrays designed using the AEP-DNN method could sustain high gain and performance over a broad range of steering angles, enhancing coverage area without compromising signal quality. These theories consider important elements of designing dual-polarised antenna arrays, concentrating on the quality of signals, efficiency of response, and versatility needed for modern beam-steering applications in areas such as wireless network systems. It also highlights that dual-polarised systems could scale more

easily without increasing the number of physical elements, making the solution compact, cost-effective, and flexible, especially important in 5G mobile terminals.

1.7 RESEARCH SCOPE

The research focuses on creating the AEP-DNN technique for the DLPAA at 28 GHz. The focus of the AEP-DNN algorithm's focus is to generate an array pattern synthesis that steers the main beam towards a specific location without reducing the sidelobes levels. The algorithm could only utilize 4 samples of the desired main beam to test the AEP-DNN model that was created. This research does not include additional 5G frequency bands. The antenna is specifically designed for mobile applications. It is widely recognized that the antenna for mobile devices needs to be small to accommodate various elements positions and movements, thus, the linear array configuration is chosen. Patch antennas are known for being lightweight and easy to fabricate into a compact and flat design. The proposed antenna would be designed and analysed using the Computer Simulation Technology Microwave Studio (CST MWS) 2023, and the Matrix Laboratory (MATLAB) computing language would be used to optimize antenna phase excitations for array pattern synthesis through the implementation of the AEP-DNN method.

1.8 RESEARCH METHODOLOGY

In this work, the research approach designs a single and 1 x 4 antenna array, develops the AEP-DNN algorithm, fabricates it, measures the antenna, and validates the simulation results. Figure 1.2 shows a flowchart summarizing the research methodology.

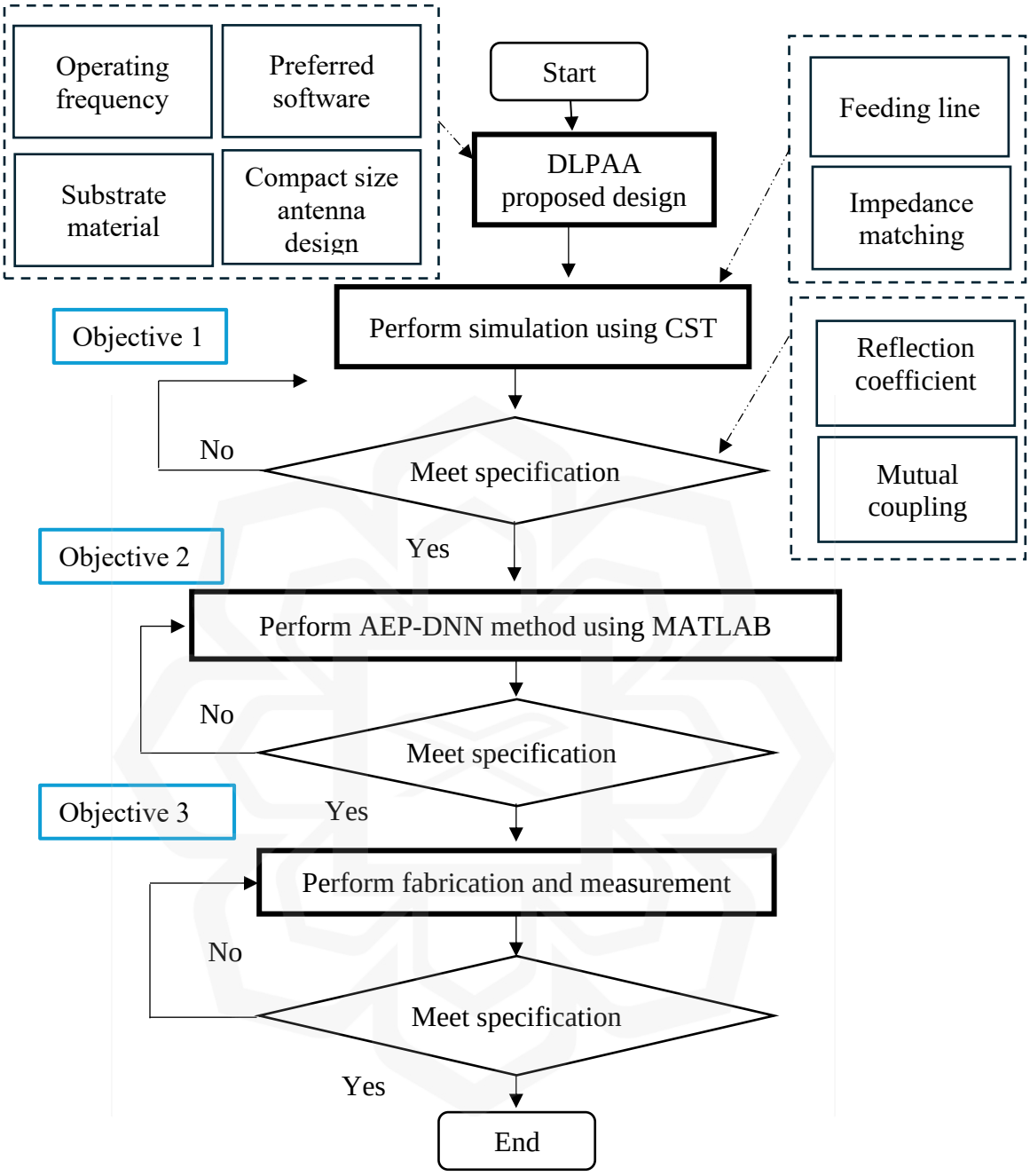

Figure 1.2 The Flowchart of Research Methodology

1.9 THESIS ORGANIZATION

Figure 1.3 summarizes the chapters of the thesis.

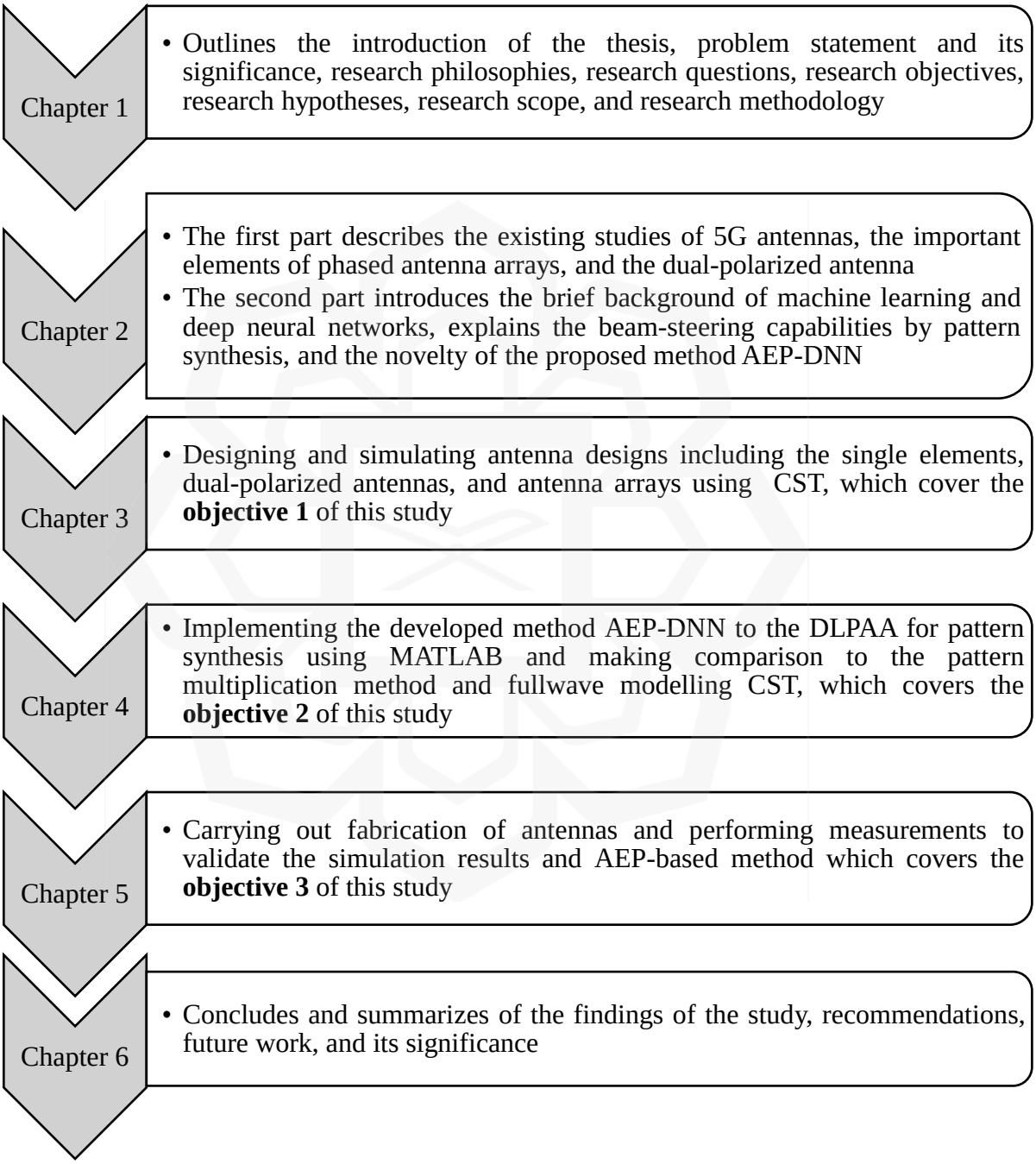

Figure 1.3 The Summary of Thesis's Chapters

CHAPTER TWO

LITERATURE REVIEW

2.1 INTRODUCTION TO ANTENNA

Chapter 2 consists of two parts: The first part describes the background of antennas, their parameters, phased antenna arrays including inter-element spacing, active element pattern (AEP), and dual linear polarization antennas. The second part discusses on the machine learning, beam-steering capability through pattern synthesis, deep neural networks, and implementation of the AEP-DNN algorithm.

2.2 THE ANTENNA PARAMETERS

Antennas are employed for the transmission and reception of electromagnetic waves in a particular direction. An effective antenna ought to be capable of efficiently transmitting and receiving power. To design an effective antenna, it is necessary to understand the fundamental properties listed below. This study focuses on the reflection coefficient, mutual coupling, impedance bandwidth, radiation pattern, gain, and Friis transmission as key properties.

2.2.1 Reflection Coefficient

The reflection coefficient (S_{11}) of an antenna is a measure of how much of the power sent to the antenna is reflected back instead of being radiated. It is a key parameter in assessing antenna performance, as it indicates the effectiveness of power transfer from the transmission line to the antenna. The reflection coefficient, theoretically denoted by Γ, is defined by the ratio of the reflected voltage wave, V_{ref} to the incident voltage wave, V_{inc}:

$$\Gamma = \frac{V_{ref}}{V_{inc}} \tag{2.1}$$

All power is deflected from the antenna and nothing is radiated if S_{11} equals 0 dB. If S_{11} is equal to -10 dB, then -7 dB of power is reflected back when 3 dB of power is applied to the antenna.

2.2.2 Mutual Coupling

Mutual coupling of antennas refers to the interaction or coupling between nearby antennas due to their electromagnetic fields. When antennas are placed close to each other, the current on one antenna could induce currents on the neighboring antennas, affecting their performance and radiation characteristics. This phenomenon is particularly important in antenna arrays and multi-antenna systems, as mutual coupling could significantly influence array patterns, impedance matching, and overall efficiency.

The strength of mutual coupling between two antennas is often quantified using a coupling coefficient, which describes the degree of energy transfer between the antennas. This could be expressed in terms of the S-parameters, S_{21} or S_{12}, which represent the transmission between two ports (port 1 and 2) of antenna in a network.

2.2.3 Impedance Bandwidth

The bandwidth of an antenna is the range of frequencies over which the antenna could operate effectively while meeting certain performance criteria. It is typically defined as the frequency range where the antenna maintains acceptable impedance matching. Impedance bandwidth is the range of frequencies over which the antenna's input impedance matches well with the source impedance. The bandwidth could be expressed either as:

$$Impedance\ Bandwidth\ (-10\ dB) = upper\ frequency - lower\ frequency \quad (2.2)$$

2.2.4 Radiation Pattern

The radiation pattern of an antenna is a graphical representation of the distribution of the radiated power as a function of direction in space. It illustrates how an antenna transmits or receives energy in different directions, typically depicted in two or three dimensions. In most cases, this radiation pattern is normalized and shown in decibels (dB or dBi). The radiation field's three-dimensional (3D) pattern is depicted in Figure 2.1.

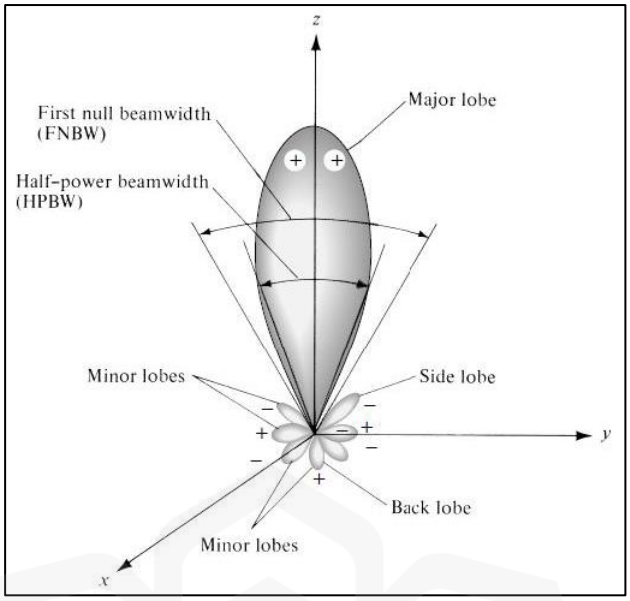

Figure 2.1 The 3D Radiation Pattern (Tan, 2019)

Main lobe is the main region in the radiation pattern where the antenna radiates the strongest power, typically in the desired direction. Minor lobes refer to any lobe that is not the main lobe. Minor lobes represent regions where the antenna radiates energy, but at a lower intensity compared to the main lobe. They typically include sidelobes and the back lobe. Sidelobes that radiate in directions other than the main lobe. Sidelobes are often unwanted because they represent power radiated in directions that might cause interference or wasted energy. The back lobe is a lobe opposite the main lobe direction, usually smaller in amplitude. High-performance antennas typically have a minimized back lobe. Beamwidth is the angular width of the main lobe, measured between the half-power (-3 dB) points. Narrow beamwidth indicates high directivity.

Commonly, there are three types of radiation patterns. Firstly, the omnidirectional pattern. It radiates power uniformly in all directions in one plane with minimal variation, like a dipole antenna. Secondly, the directional pattern radiates power more strongly in one or specific directions, often used in applications requiring high gain and directivity, like a parabolic dish. Lastly, the isotropic pattern is a theoretical point source that radiates power

equally in all directions in three-dimensional space, used as an ideal reference for real antennas. In this study, the desired antenna aims for a directional pattern. The radiation pattern is crucial for understanding an antenna's directional properties and for ensuring effective coverage in the desired directions, while minimizing interference in others.

2.2.5 Gain

Gain of an antenna is defined as "the ratio of the intensity, in a given direction, to the radiation intensity that would be obtained if the power accepted by the antenna were radiated isotropically. The radiation intensity corresponding to the isotropically radiated power is equal to the power accepted by the antenna divided by 4π".

$$Gain = 4\pi \frac{radiation\ intensity}{total\ input\ power} \tag{2.3}$$

2.2.6 Friis Transmission

The Friis transmission equation is a fundamental formula in wireless communications that calculates the power received by an antenna from another antenna that is transmitting, given the distance between them and the characteristics of both antennas. It is particularly useful for understanding the behavior of signals in free space (without obstacles or interference). The situation is depicted in Figure 2.2. A transmitter sends power, P_T to an antenna with gain, G_T towards the receiver. The antenna of the recipient has a gain factor of G_R. Antenna gain equals directivity multiplied by radiation efficiency, with losses from impedance

mismatch not accounted for by G_T and G_R considering only internal losses of the antenna. Equation 2.4 represents the Friis transmission equation.

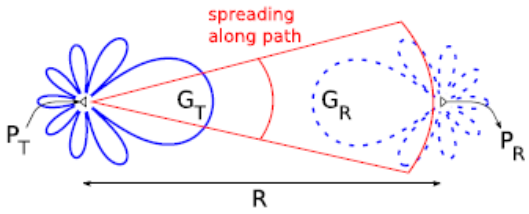

Figure 2.2 Radio-Waves Transmission (Cai et al., 2021)

$$P_{R,max} = P_T G_T \left(\frac{\lambda}{4\pi R}\right)^2 G_R \tag{2.4}$$

where P_R is the received power at the receiving antenna (watts), P_T is the transmitted power from the transmitting antenna (watts), G_T is the gain of the transmitting antenna, G_R is the gain of the receiving antenna, λ is the wavelength of the transmitted antenna ($\lambda = c/f$), c is the speed of light (meter/seconds), f is the frequency (hertz), and R is the distance between the transmitting and receiving antenna (meters).

2.3 MICROSTRIP PATCH ANTENNA

A microstrip patch antenna is a type of low-profile antenna that is commonly used in wireless communication systems due to its compact size, light weight, and ease of fabrication. It typically consists of a rectangular or circular "patch" of metal (often copper or gold) on top of a grounded dielectric substrate, and the lower conductor is the ground plane as shown in Figure 2.3.

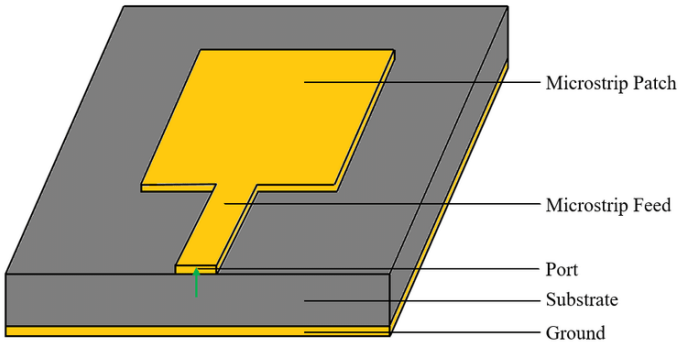

Figure 2.3 The Structure of Microstrip Patch Antenna (Chowdhury et al., 2019)

The microstrip patch antenna is usually made up of four components: patch, ground plane, dielectric substrate, and feed line, arranged in a single-layer design.

1. Patch: The metallic patch is the radiating element of the antenna. It usually has a length that is approximately half of the wavelength of the frequency it is designed to transmit or receive. Common shapes include rectangles, circles, and other configurations that affect its radiation characteristics and polarization.

2. Dielectric Substrate: The patch is placed on top of a dielectric substrate, which is a non-conductive material that supports the patch. The dielectric constant of the substrate affects the resonant frequency and radiation efficiency of the antenna.

3. Ground Plane: Beneath the dielectric substrate is a conductive ground plane. This acts as a reflective surface to ensure that most of the radiation is directed away from the substrate rather than into it.

4. Feed Line: The patch is usually connected to a feed line that delivers power to the antenna. Common feeding techniques include microstrip line feed, coaxial probe feed, aperture coupling, and proximity coupling, each affecting the antenna's impedance matching and bandwidth.

The thickness of the substrate has a significant effect on the resonant frequency and the bandwidth of antenna (Paul et al., 2015). The substrate material should have a low insertion loss, with a loss factor of less than 0.005. This study focuses on the Rogers RT5880 substrate material with a dielectric constant of 2.2, tangent loss of 0.0009, and thickness of 1.575mm. It is selected because of its robustness and appropriate for the smaller antenna size, and increases efficiency.

2.3.1 Transmission Line Model

There are numerous techniques for microstrip patch antenna analysis; however, transmission lines are the most common and simplest for the patch antenna. This method uses a low-impedance transmission line of specific length. In this study, the scenario to investigate the theory of microstrip transmission line is W/h <<1 and ε_r>1 (small transmission line) as shown in Figure 2.4.

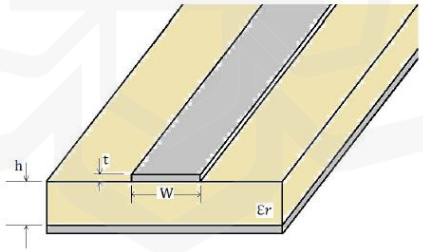

Figure 2.4 The Microstrip Transmission Line (Zhang et al., 2023)

The empirical formulas here that only depend on the dimensions of the line: the width, *W*, the length, *L*, the height of substrate, *h*, and the dielectric constant, ε_r, of the substrate. As a first approximation, we assume that the thickness of the conductor, *t* which

forms the line, does not affect our calculations because it is very thin compared to the substrate thickness ($h >> t$). The characteristic impedance of the microstrip line could be expressed as follows (Zhang et al., 2023):

$$Z_O = \left\{\frac{60}{\sqrt{\varepsilon_r}} ln\left(\frac{8h}{W} + \frac{W}{4h}\right)\right\} \tag{2.5}$$

ε_{reff} is the effective dielectric constant. The width of the microstrip line is given by:

$$W = \frac{c}{2f_o\sqrt{\frac{(\varepsilon_r+1)}{2}}} \tag{2.6}$$

where f_o is the resonant frequency, and c is the speed of light. The edge effect causes the microstrip patch antenna in Figure 2.5 to appear longer than its actual length. ΔL separates the effective length (L_{eff}) from the physical length as a result. The following formula could be used to approximate the linear extent of the patch very well:

$$\frac{\Delta L_{eff}}{h} = 0.412\frac{(\varepsilon_{reff}+0.3)(\frac{W}{h}+0.264)}{(\varepsilon_{reff}-0.258)(\frac{W}{h}+0.8)} \tag{2.7}$$

Equation 2.7 shows that the extension of the length ΔL is a function of the ratio $\frac{W}{h}$ and ε_{reff}. To calculate the effective length (L_{eff}), we add the length (L) to the extension of the length ΔL as shown:

$$L_{eff} = (L + 2\Delta L_{eff}) \tag{2.8}$$

The resonant frequency is given by:

$$f_o = \frac{c}{2L\sqrt{\varepsilon_r}} \tag{2.9}$$

Where c is the speed of light in free space.

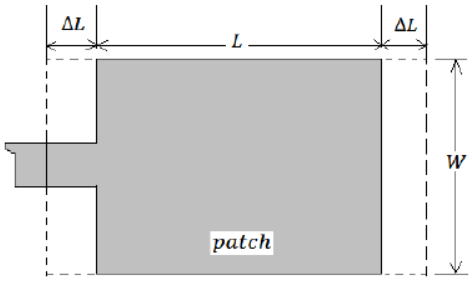

(a)

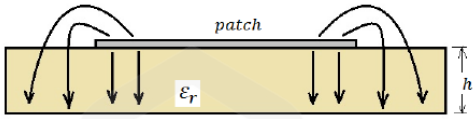

(b)

Figure 2.5 (a) The Front View of Model and (b) The Transmission Line of Model (Zhang et al., 2023)

The approximate characteristic impedance provided in Equations 2.5 to 2.9 should be acknowledged. It is assumed that the radiation spot is positioned within the dielectric, as illustrated in Figure 2.6, to calculate the effective dielectric constant.

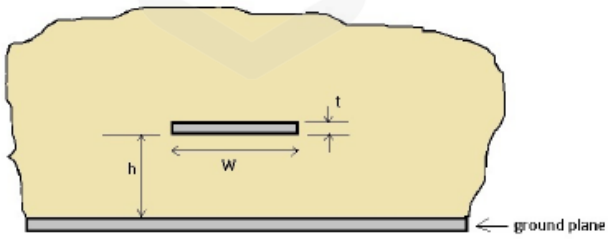

Figure 2.6 The Medium of Effective Dielectric Constant (Zhang et al., 2023)

2.3.2 Rectangular Patch Antenna

The microstrip patch antenna is compact, inexpensive, integrates well, flexible, offers various polarizations, and is easily able to steer beams. However, it has drawbacks such as low gain and narrow bandwidth compared to other antennas, which could be challenging for wireless systems, especially at millimeter-wave frequencies. Recently, researchers have conducted numerous investigations to address the limitations of microstrip patch antennas. Proposed techniques for improvement include designing patches with multiple antennas and enhancing the overall antenna structure. Various designs of microstrip patch antennas exist, each tailored to specific characteristics. The rectangular, square, and circular shapes are the most frequently used patch designs for millimeter-wave frequencies. In this study, a rectangular patch design is selected.

Compared to other previous patch antenna designs in recent researches, the rectangular microstrip patch antenna has demonstrated significantly better performance in gain and radiation efficiency. Therefore, it is a viable candidate antenna type for upcoming 5G wireless communication applications (Fante & Gemeda, 2020). According to the research conducted by Razak and Shah (2022), a rectangular microstrip patch is recommended for 5G mobile communications, featuring single-element and array configurations with two and four elements, utilizing Rogers RT5880 substrate material. The simulation results show that the gain and directivity increase as the number of elements in the antenna array for the rectangular microstrip patch antenna, regardless of the feeding method used.

Due to the growing demand for mobile data and handheld devices, Darboe et al. (2019) has proposed a rectangular microstrip patch antenna for use in 5G technology. This antenna proposal is a suitable choice for 5G mobile communication that requires high bandwidth and gain. The antenna is very small in size and is therefore ideal for devices with limited space.

2.4 PHASED ANTENNA ARRAY

Phased antenna arrays are currently undergoing significant research by both academia and industry, broadening their appeal beyond specific interest groups. Initially, they were solely used for military purposes, aiming to direct the radiation beam for identifying targets. Nonetheless, they are currently utilized for civilian applications like sonars, satellites, radio stations, radars, and numerous other uses.

A phased antenna array is an antenna system that consists of multiple individual antennas (or radiating elements), each of which could be individually controlled in terms of its phase and amplitude. By adjusting these parameters, the phased array could steer the direction of the radiated signal without physically moving the antenna structure. This is done through constructive and destructive interference, allowing the system to focus the signal in specific directions or scan across a range of angles. However, creating arrays faces challenges like high sidelobes level and mutual coupling, as well as low gain.

To maintain the performance of an antenna array pattern, a feeding network is essential to deliver the signal from the source ports to every single antenna element port. Each antenna element receiving the signal would be excited. The radiation pattern of the antenna array is shaped by the excitations, spatial locations, and the individual radiation patterns of each antenna element. In this study, the active scattering parameters are analysed with all elements being excited simultaneously. In this study, the arrangement of radiating antenna elements is in a linear form.

2.4.1 Linear Array Characteristic

To illustrate a simple concept of a linear array radiation pattern, a uniform linear array composed of N elements aligned along the x-axis with a phi angle of zero (ϕ=0°) for

scanning in the θ direction is used. Assume each antenna element has an identical radiation pattern; the array pattern could be expressed as:

$$F(\theta) = \boldsymbol{f_i}(\theta) \sum_{n=1}^{N} e^{j(n-1)\varphi} \tag{2.10}$$

where phase, $\varphi = kd\ cos\ \theta + \beta$, $\boldsymbol{f_i}$ is the isolated element pattern of the array, k is the wave number of $2\pi/\lambda_g$, d is the inter-element spacing, and β is the phase difference. Based on this formula, the array pattern is simply the product of the isolated element pattern and array factor. This traditional array pattern calculation is also called as pattern multiplication method (PMM) which it does not include mutual coupling factors.

The array factor of this uniform array could be altered by changing the inter-element spacing or by introducing a phase difference between elements using transmitter and receiver modules or different phase-shifting methods. The purposeful application of phase-shifting determines the main beam's direction and steer it toward a desired angle $\theta°$. It could be calculated for the uniform linear array using the expression (Alam et al., 2024):

$$\beta = kdcos\theta_0 \tag{2.11}$$

Figure 2.7 visualizes uniformly separated elements by some distance d. In order to find the phase difference based on the figure, it is simply a multiplication of $dcos(\theta)$ by the propagation wave number k.

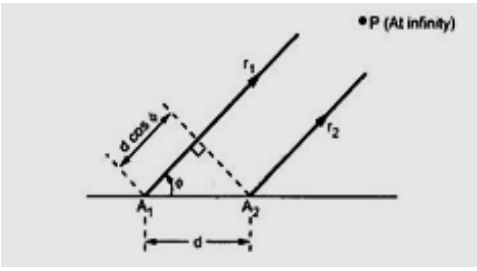

Figure 2.7 The Phase Difference between Radiating Antenna Elements in a Uniform Linear Array (Alam et al., 2024)

The typical approach to generate a phase difference involves employing a series-fed phased array method, where each source port of the antenna array is fed individually by one source. In this study, coaxial edge feeding of Sub Miniature version A (SMA) connectors with 50 Ω impedance matching is used for source excitations. This is because coaxial edge feeding could reduce mismatched impedance and create a simpler antenna design for fabrication, especially at millimeter-wave frequencies.

2.4.2 Factors Affecting Radiation Pattern in Antenna Array

There are several factors affecting the radiation pattern of an antenna array such as the inter-element spacing and mutual coupling.

2.4.2.1 Inter-Element Spacing

Element spacing refers to the lambda distance separating adjacent radiating antenna elements. Element spacing could manipulate the visible area of the antenna array. In theory, when the distance between elements expands, the radiation of sidelobes increases while the power of the main beam decreases (Kummer, 1992):

$$\frac{d}{\lambda} \leq \frac{1}{1+|cos\theta_0|} \tag{2.12}$$

where θ_0 is the angle that the sidelobes would occur. For half lambda spacing, the sidelobes would occur at θ=+90° when the array is scanned to 90°. As explained by Balanis (2016),

d>1 λ would generate sidelobe and introduce mutual coupling which leads to undesired changes to radiation pattern. A balance should be made to compromise and optimize the design. However, in this study, the spacing has been set to 2.159 λ . When antenna elements are spaced more than one wavelength apart (d>1 λ), unwanted radiation called grating lobes could appear in directions other than the main beam. These lobes reduce the performance of the antenna array. Although grating lobes mainly depend on the spacing, frequency, and scan angle, the use of ±45° slanted polarization could also affect them indirectly. Slanted polarization produces electric fields in both horizontal and vertical directions, which could change how signals from different elements interact. This might increase or reduce the strength of the sidelobes. It could also affect mutual coupling between elements and modify the radiation pattern slightly. While slanted polarization could not remove grating lobes caused by large spacing, it could influence their strength and direction, which is important to consider when designing beam-steering capability on 5G antennas. The spacing 2.159 λ also could not be further reduced due to the RF 2.92 mm SMA connector with dimension of 1.27 cm (in practical).

2.4.3 Mutual Coupling

Mutual coupling of antennas refers to the interaction or coupling among nearby antennas due to their electromagnetic fields. When antennas are placed close to each other, the current on one antenna could induce currents on the neighbouring antennas, affecting their performance and radiation characteristics. This phenomenon is particularly important in antenna arrays, as mutual coupling could significantly influence array patterns, impedance matching, and overall efficiency. To reduce mutual coupling effects on the antenna array radiation pattern, it is recommended to have an inter-element spacing that is larger than half a wavelength. Researchers investigated how mutual coupling affects the performance of antenna arrays in transmit mode when all elements are excited simultaneously, using a study by Pralon et al. (2017) as reference. The results show that the mutual connection

lowers their overall benefit and leads to a shift from the intended direction of the steering angle. Mutual coupling also affects the polarization purity of the components. This explains why mutual coupling is an essential element of the total radiation pattern.

2.4.4 Review on Phased Antenna Array

Researchers commonly utilize the linear and planar array configurations to study antenna performance. As mentioned in the work carried out by Yadav et al. (2021), a compact size antenna has been a promising candidate for millimeter-wave frequency antenna specifically at 28 GHz. The design size is 16 x 39 mm^2 operates in the frequency band of 27.089-28.856 GHz is shown in Figure 2.8. A tree structure is designed to improve gain and size reduction by using tilting method where branches are tilted at 30°. A tree structure design is configured in linear array with one feeding port. It managed to produce outputs of 9.04 dBi gain and 76.01% radiation efficiency.

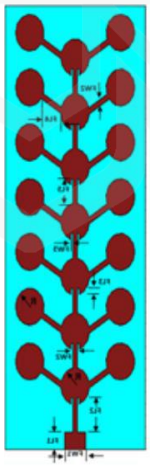

Figure 2.8 A Linear-Tree Structure Design (Yadav et al., 2021)

Besides, antenna features with low cost, light weight, low profile, and compatible with monolithic microwave integrated circuit are used widely in mobile communication. A microstrip patch antenna with overall dimension of single patch is 14.71 x 7.9 x 0.254 mm^3 is designed by Mungur and Duraikannan (2018) as shown in Figure 2.9, to investigate the millimeter-wave antenna performance as well as their 2 x 1 and 4 x 1 antenna array. They managed to get gain value of 10.20 dB and 13.55 dB for respective antenna array, meanwhile, the bandwidth for all antennas achieved more than 500 MHz. In their previous study, it was demonstrated that as the number of patches increases, the gain also increases. This results in a narrower and more directional beam with higher radiation efficiency.

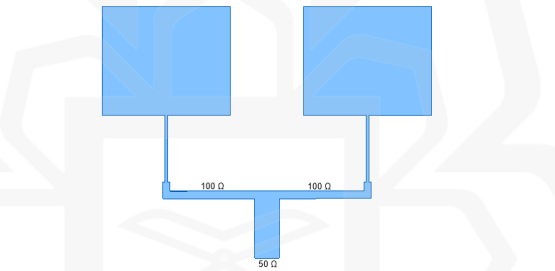

(a)

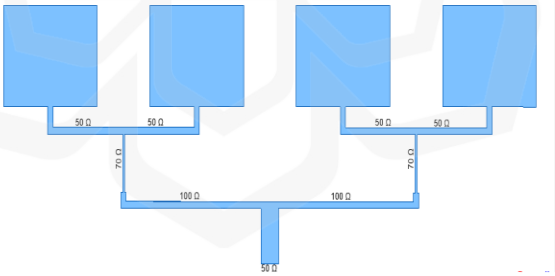

(b)

Figure 2.9 (a) The 2 x 1 and (b) the 4 x 1 Antenna Array (Mungur & Duraikannan, 2018)

In comparison with the mentioned previous works, the work investigated by Pant et al. (2020) has distinctive design as it might looked like a planar array but it is actually a series-fed linear antenna array configured with 16 elements. This design is appropriate to modern antenna technologies like massive Multiple-Input-Multiple-Output (MIMO) and millimeter-wave band to achieve data rate up to 10 Gbps. The 1 x 16 elements tapered antenna array feed with tapered microstrip lines and employing bending lines between the patches are designed to operate at 28 GHz and achieved gain and bandwidth of 17.9 dBi and 1 GHz respectively is shown in Figure 2.10. The bending transmission line between the patch antennas elements help to boost the antenna gain, return loss, bandwidth, and radiation efficiency.

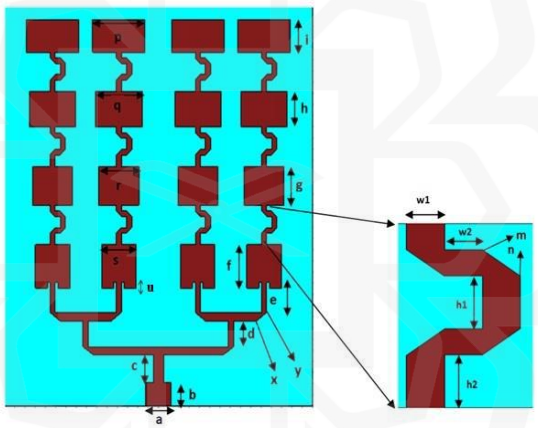

Figure 2.10 The 1 x 16 Tapered Antenna Array Feed (Pant et al., 2020)

Another most common array configuration used is planar configuration. As shown an example of 2 x 2 planar array configuration in previous work investigated by Johari et al. (2018), a compact size of 26.5 x 20.37 mm^2 operates at 28 GHz is designed and successfully improve the antenna gain up to 8.39 dB, efficiency 82.85%, and bandwidth 400 MHz. The 2 x 2 planar array design is shown in Figure 2.11 below.

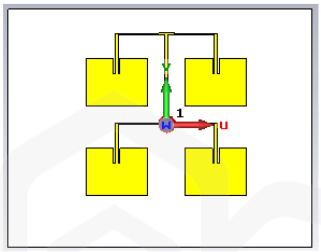

Figure 2.11 The 2 x 2 Planar Array Configuration (Johari et al., 2018)

A similar design of 2 x 2 planar array configuration shown in Figure 2.12 to previous work by Johari et al. (2018), however, adding on two slots on single patch elements carried out by M. Mohamed et al. (2020), with a total dimension of whole antenna 42.63 x 44.10 mm^2. The gain, bandwidth, and efficiency value outputs 23.9 dBi, 4 GHz, and 99% in which significantly high.

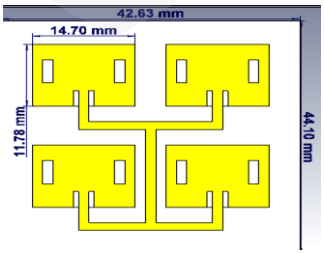

Figure 2.12 The Slotted 2 X 2 Planar Array Configuration (M. Mohamed et al., 2020)

Besides, a 2 x 2 planar array configuration designed by Soliman et al. (2019), also has similar design with the previous works done, except that they used different substrate material and thickness, and the feeding method. Figure 2.13 illustrates the design and it successfully produces output value of bandwidth, gain, and efficiency of 1.3 GHz, 15.31 dB, and 97.3%.

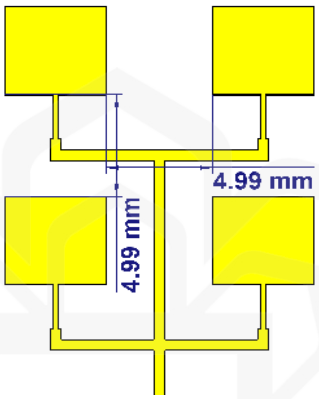

Figure 2.13 The 2 X 2 Planar Array Configuration (Soliman et al., 2019)

Nonetheless, this study focuses solely on the linear array configuration due to its simplicity compared to other antenna designs. Additionally, this study specifically aims for the dual polarization feature of an antenna. Thus, choosing the array configuration is a careful process since the linear array is the most straightforward way to implement dual polarization. The fundamental idea behind dual polarization of an antenna is that the radiating elements on a patch antenna need to be symmetrical or perpendicular to each other in order to achieve dual polarization. Implementing dual polarization feature into an antenna array is more difficult when using a planar array configuration. Table 2.1 shows the summary of previous works on the array configuration at 28 GHz.

Table 2.1 The Summary of Previous Works on Array Configuration at 28 GHz

Author(s)/Title	**Configuration and Number of Antenna Elements**	**Size (mm)**	**Reflection Coefficient (dB)**	**Bandwidth (GHz)**	**Gain (dB)**
(Yadav et al., 2021)	Linear, 6 elements	16.00 x 39.00	-33.50	1.70	6.89
(Mungur & Duraikannan, 2018)	Linear, 2 and 4 elements	Not reported	-23.43 (1 x 2 array) 28.11 (1 x 4 array)	0.50	10.07 (1 x 2 array) 13.55 (1 x 4 array)
(Pant et al., 2020)	Linear, 16	35.00 x 28.00	-50.35	1.00	17.90
(Johari et al., 2018)	Planar, 4	26.51 x 20.37	-30.00	0.40	8.39
(M. Y. Mohamed et al., 2020)	Planar, 4	42.63 x 44.10	-74.00	4.00	21.75
(Soliman et al., 2019)	Planar, 4	Not reported	-61.19	1.30	13.16

2.5 DUAL LINEAR POLARIZATION

Antenna polarization is the positioning of electromagnetic energy transmitted or received by an antenna. A radio electromagnetic signal consists of electric and magnetic fields traveling at right angles. Polarization is determined by the alignment and movement of the electric field. There are three classifications of antenna polarity: linear, circular, and elliptical polarization. Slant polarization, also referred to as diagonal polarization, happens when the electric field is oriented at a 45° angle to the wave's perpendicular plane. Dual-polarised antennas, in contrast to single-polarised ones, serve distinct purposes despite their similar appearance. By utilizing simultaneous polarization diversity, antennas could provide the functions of two separate antennas in a single device. For instance, multiple antenna elements arranged orthogonally or a pair of linearly polarised radiating elements could be formed by dipoles, planar elements, or slots positioned at right angles or at +45° or -45° to each other and placed in front of a reflector to enhance directivity.

Implementing dual linear polarization in an antenna offers numerous benefits, including wide bandwidth, low cross-polarization, high port isolation, low output correlation, increased channel capacity, and high polarization diversity (Feng et al., 2020). Positioning the antenna elements at a 45° angle from each other could enhance coverage in congested areas, decreasing interference and boosting antenna efficiency. In the next section, we would talk about previous studies on designing dual linearly polarised antennas.

2.5.1 Review on Dual-Linearly Polarised Antenna Design

This section would explain the examples of previous works that implement dual linear polarization to patch antennas. Many researchers have adopted the stacked patch antenna design to enhance antenna performance and incorporate dual polarization into the antenna. The research conducted by Stanley et al. (2019) demonstrated a stacked capacitive coupled patch antenna with bent parasitic elements that could operate with dual polarization at frequencies of 28 GHz and 39 GHz. The dimensions of the antenna are 3.8 mm in length, width, and height as shown in Figure 2.14. The lower band shows simulated bandwidth and gain output of 4.5 GHz and 7.14 dBi. This antenna size is highly suitable for implementing antenna arrays in mobile phones.

Figure 2.14 The Stacked Capacitive Coupled Patch Antenna (Stanley et al., 2019)

Studies conducted using a similar capacitive coupling method as demonstrated by Chu et al. (2019) also utilized three stacked patches for a dual-polarised dual band antenna operation. Feed via is used to generate signals both vertically and horizontally through coupling as shown in Figure 2.15. It produces simulated gain exceeding 8.5 dBi for the 27.48-28.50 GHz frequency range.

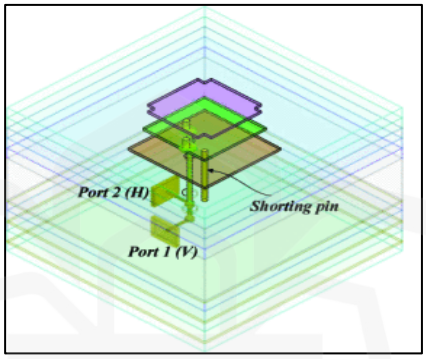

Figure 2.15 The Stacked Patch Antenna (Chu et al., 2019)

Research conducted by Yong (2019), a dual band dual-polarised stacked patch antenna was developed to meet the needs of 5G smartphones as shown in Figure 2.16, operating at 28 GHz and 39 GHz with a simulated gain of 11-12 dBi.

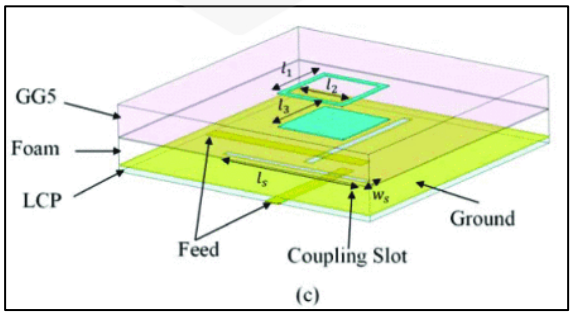

Figure 2.16 The Stacked Patch Antenna (Yong, 2019)

The dual polarization feature was achieved using a proximity fed method, similar to the design proposed by Lee et al. (2019). This design involved stacking a proximity fed square ring and a square patch, with two microstrip transmission lines placed orthogonally to create dual polarization as shown in Figure 2.17. The authors achieved a simulated array bandwidth of 400 MHz and a simulated array gain of 15.2 dBi. Phase shifters are utilized to change the main beam direction, allowing for up to 60 scanning angles with a peak gain exceeding 10 dBi.

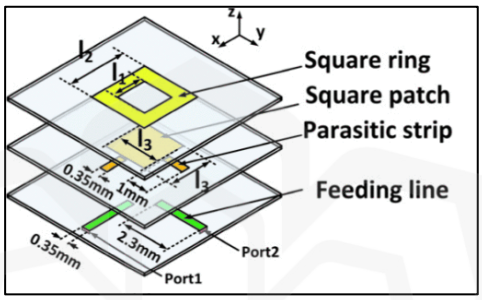

Figure 2.17 The Stacked Proximity Fed Patch Antenna (Lee et al., 2019)

Also referred to as emerging antennas, shared aperture antennas offer the distinct advantage of supporting dual band or multiband frequency as well as dual polarization capability. In a study by Mei et al. (2021), a shared aperture antenna was suggested by merging a folded transmit antenna array in Ka band with a Fabry-Perot cavity antenna in X-band as shown in Figure 2.18. The 2.5 GHz bandwidth and 23.6 dBi gain are achieved.

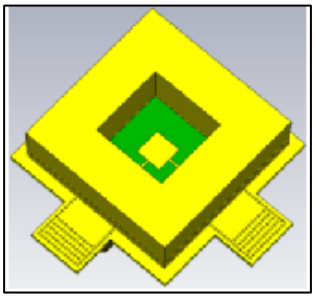

Figure 2.18 The Shared Aperture Antenna (Mei et al., 2021)

Nevertheless, all of the aforementioned prior research focused solely on a single antenna design. Designing an antenna array with dual polarization is becoming increasingly difficult as the length and width dimensions of both vertical and horizontal transmission lines ought to be identical, and even a small change to the design could have a significant impact on the dual polarization feature. There have been limited studies on an array design that incorporates dual polarization functionality and operates at 28 GHz. According to the research conducted by Hwang et al. (2019), the writers have used a substrate-integrated cavity made up of via walls for a stacked patch antenna with 8 elements and 12 layers of printed circuit board (PCB) lamination as shown in Figure 2.19. It suggested using vertical beam-steering for active antenna base station use. Simulated results show a bandwidth of 4 GHz and gain of 16.5 dBi, with minimal gain variation throughout the frequency range.

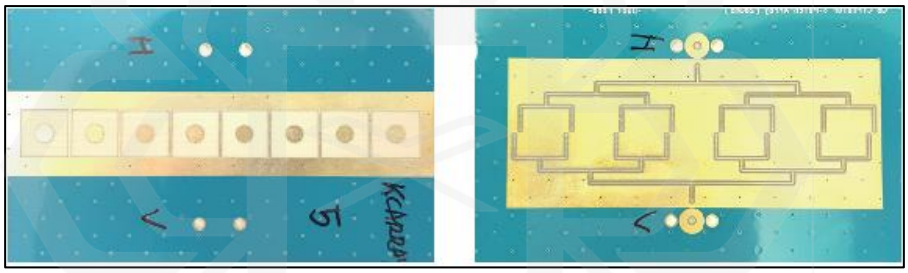

Figure 2.19 The Substrate-Integrated Cavity Stacked Patch Antenna (Hwang et al., 2019)

In addition to creating an array for dual polarization signals, Elhabbash and Skaik (2019) also developed a base station octagonal prism structure to position sub-antenna arrays along the sides of the prism for creating multi-beam radiation patterns with 12 sub-arrays on each side as shown in Figure 2.20. The sub-arrays antenna is switched between vertical and horizontal polarizations to trigger dual-polarised signals using phase shifters. The ability to steer the pattern in specific directions is present, but this beam scanning range is restricted to fixed positions of -10°, 0°, and +10° at both 28 GHz and 38 GHz. While the 12.6 dBi gain was attained and the entire setup supports dual polarization, it required

incorporating the base station configuration and phase shifters to enable both polarizations rather than relying solely on the antenna design.

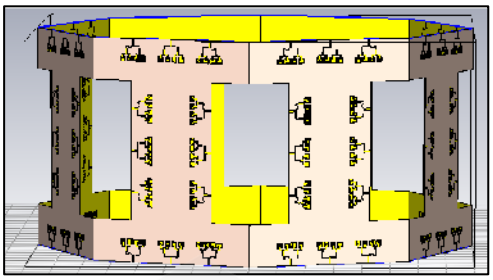

Figure 2.20 The Octagonal Prism Structure Patch Antenna (Elhabbash & Skaik, 2019)

Furthermore, another method to implement the dual polarization feature into an antenna is by designing slanting 45° of patch elements. A dual-polarised 45° antenna is a type of antenna that could transmit and receive signals with two different polarizations simultaneously. It could be used to transmit and receive two separate signals or data streams on the same frequency band. Based on research carried out by Lv et al. (2021), it presents an antenna array that is both dual-polarised and single-layered, designed specifically for millimeter-wave (mm-wave) technologies as shown in Figure 2.21. The array operates at ±45° polarization and is geared towards enhancing applications in fields such as 5G communications, automotive radar, and imaging sensors. This design employs orthogonal circular polarization to achieve high polarization purity and directional radiation, providing flexibility and efficiency critical for mm-wave systems. The antenna feeds equal signal amplitudes to each port, resulting in a linearly polarised wave while maintaining a compact single-layer structure, reducing complexity and integration costs.

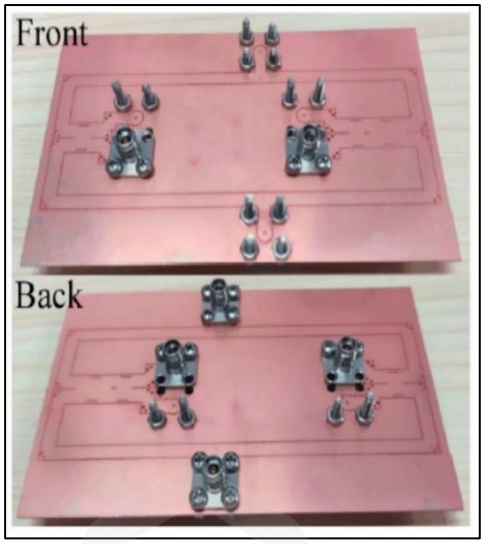

Figure 2.21 Multiple Feeding Ports on Single Layer Antenna (Lv et al., 2021)

The design by (Lv et al., 2021) used a single-layer ±45° dual-polarised antenna that was simple and easy to build. However, it had several drawbacks. The design required external phase shifters to achieve dual polarization, adding extra cost and complexity. While the antenna tried to reduce unwanted cross-polarization by arranging the elements side by side, it still faced issues with mutual coupling and signal interference. In this study, a new improved design is proposed using slanted ±45° patch elements with separate feeds. This new approach helps to reduce interference, and improve beam direction stability, while keeping the structure simple and suitable for 28 GHz 5G systems.

Therefore, considering the drawbacks of previous studies, in this research, we suggest a dual-polarised antenna slanted at ±45° on a single layer and operating at a resonant frequency of 28 GHz. Its small and uncomplicated antenna arrangement sets it apart from previous studies as it does not involve stacked patches for the antenna configuration. In the past, dual-polarised antennas operating at 28 GHz were typically made with a multilayer structure, making it difficult to create one without multilayer patches. Moreover, just one feeding port is needed for this antenna to excite dual polarization signals (+45° and -45°) at the same time.

This research project involves the development of a simpler dual-polarised antenna design operating at 28 GHz. Initially, the slanted patch antennas radiating at both +45° and -45° angles were designed individually. Next, the two are merged to achieve dual polarization capability and analyze how it affects return losses and radiation patterns. Because of its emphasis on mobile applications, the design is much simpler and less complex than the previous works. Table 2.2 summarizes the previous works on dual-polarised antennas.

Table 2.2 The Summary of Previous Works on Dual-Polarised Antenna

Article(s)	**Method**	**Dimension (mm)**	**Reflection Coefficient (dB)**	**Bandwidth (GHz)**	**Gain (dB)**
(Stanley et al., 2019)	Capacitive-coupled patches	3.80 x 3.80	<-10.00	4.50	4.99
(Chu et al., 2019)	Capacitive coupling	Not reported	-12.00	1.02	4.15
(Yong, 2019)	Capacitive orthogonal ports	75.00 x 156.00	<10.00	6.00	8.85
(Lee et al., 2019)	Proximity fed orthogonal ports	Not reported	<-10.00	0.40	13.05

(Mei et al., 2021)	Shared aperture-substrate integrated waveguide	85.00 x 85.00	<-10.00	2.50	22.25
(Hwang et al., 2019)	Substrate-integrated cavity made up of via walls	Not reported	<-10.00	4.00	14.35
(Elhabbash & Skaik, 2019)	Phase shifter	Not reported	-29.00	1.00	10.45
(Lv et al., 2021)	Feeding network of multiple ports	Not reported	-19.00 (at 30 GHz)	7.50	6.85

2.6 INTRODUCTION TO MACHINE LEARNING

In recent years, machine learning has become increasingly popular for its ability to automate routine tasks and provide innovative ideas in various fields of science and engineering. Even though it might still be considered early days, machine learning has completely transformed the technology sector. Machine learning experts have been able to change the basic structure of various industries and academic areas, such as recently in the creation and enhancement of antennas. Given the current big data era, machine learning has become an increasingly popular topic within this industry. Machine learning offers significant potential in the field of designing antennas and predicting their behavior, allowing for faster results without compromising accuracy.

Famous for their complex forms, antennas generally lack closed-form solutions. Computational electromagnetics (CEM) is used to simulate how electromagnetic fields interact with antennas by employing Maxwell's equations. Rough estimates are commonly employed to understand the physical aspects of antenna design. Advances in numerical techniques have enabled the use of integral equations for solving linear antenna problems. Afterwards, as computers advanced, it became feasible to solve Maxwell's equations by utilizing integral and differential equation solving methods. The introduction of the method of moments (MoM) allowed for the solution of integral equations as well. More unknowns are introduced to the equations when dealing with a more complex antenna structure. Then, simpler implementations of differential equation solvers were created despite having more unknowns. Memory and Central Processing Unit (CPU) usage increase as the antenna size grows, presenting significant challenges for integral and differential equation solvers. Subsequently, rapid integral equation solvers were created that utilize iterative techniques to solve integral equations, resulting in decreased memory demands.

Due to the presence of nonlinearities, machine learning is widely studied as a supplementary method to CEM for enhancing the design and optimization of various antennas, presenting numerous advantages. Machine learning, a wide area within artificial intelligence (AI), focuses on deriving valuable knowledge from data, which is why it is

frequently associated with statistics and data science. Using a machine learning's data-driven approach, truly autonomous systems that could match, compete, and sometimes surpass human capabilities and intuition are closer to being developed.

However, the success of machine learning techniques relies heavily on the availability of data, both in terms of its quality, quantity, and accessibility, which could be challenging to obtain in certain situations. Using CEM simulation software to model the preferred antenna on different values could achieve this goal. The outcomes could be utilized to generate a dataset divided into training, validation, and testing subsets for training and assessing a machine learning model's capacity to generalize on unfamiliar data. The designer is now tasked with using their foresight and skills to recognize and improve the model's performance. Two common actions to consider in this scenario include plotting the learning curves and analyzing the bias and variance metrics. Typically, a model's success depends greatly on the designer's instinct, especially when working with neural networks, as determining the best architecture and hyperparameters is vital for achieving peak performance. Although machine learning algorithm accuracy depends on sufficient data and expertly handling the model and hyperparameters, it is becoming more popular among researchers looking for an affordable and time-saving solution (Pandey & Singh, 2024).

Machine learning methods have been widely utilized in various areas of communication technology, including antenna selection, smart grid networks for detecting potential threats, predicting user behaviors, speech recognition, context aware computing in Internet of Things (IoT) and more (Mohri, 2018).

In supervised learning, the desired results are provided beforehand. Once the learning algorithm has been applied to the provided data set, it could successfully predict outcomes for any future input with high precision. This algorithm includes linear regression, as well as artificial neural networks and support vector machines, among other components. This research is based on artificial neural networks. This method would be applied to the array configuration of a patch antenna. This involves developing a continuous linear function across the data in order for the program to predict results for unfamiliar data.

In this study, supervised learning was chosen because the goal is to predict specific beam-steering output patterns based on known input data, such as the AEP values and desired steering angles. Supervised learning is suitable when the dataset includes both the inputs and the correct outputs (labels), which is the case here, each set of excitation phases is associated with a specific radiation pattern or beam direction.

In contrast, unsupervised learning is used when there are no output labels and the goal is to find hidden patterns or groupings in the data. This is not appropriate for beam prediction, where precise direction control and quantitative accuracy such as RMSE are critical. The task requires the model to learn a mapping between input features (AEP) and the correct output (excitation phase), which is exactly what supervised learning is designed for. Furthermore, supervised learning enables the use of performance metrics such as MSE and RMSE to evaluate how well the model is performing which something unsupervised learning could not do directly.

2.7 BEAM-STEERING CAPABILITIES BY ARRAY PATTERN SYNTHESIS

Beamforming and beam-steering, though related, are distinct concepts within the same field. Beamforming involves generating beam signals from a phased antenna array towards a specific angle using specific antenna characteristics, materials, and element count. On the other hand, beam-steering involves adjusting the main beam pattern by altering the weight coefficients without modifying the antenna structure. Beam-steering is a specific aspect of beamforming where beams could be directed to a specific angle based on the amplitudes and phases of feed sources. Weight coefficients for phased antenna array could be adjusted through electronic means, mechanical methods, or machine learning techniques. Utilizing machine learning for beam-steering could result in time and cost savings through the implementation of optimization techniques within the machine learning framework.

Optimization is evident in various practical situations such as job scheduling, data mining, truss structures design, and image processing. Limited computing resources are found in many traditional optimization techniques such as the Dolph-Chebyshev method, Taylor method, least mean square (LMS) algorithm, genetic algorithm (GA), orthogonal matching pursuit (OMP) algorithm, and convex optimization.

Optimization algorithms are essential in machine learning as they help find the optimal weight and bias parameters for the model. They are used to train a machine learning model in order to minimize the cost function and find the optimal parameter values. The optimization algorithm chosen for the machine learning model after training has a direct impact on its performance, and it is selected based on the type and amount of data available.

Ali and Hassan (2014) propose using a combination of the least mean square (LMS) algorithm and the sample matrix inversion (SMI) algorithm to steer the main beam towards the desired signal and create a null in the direction of interference for a microstrip antenna array. A blend of normalized least mean square (NLMS) and recursive least square (RLS) algorithm, introduced by Khalaf et al. (2018), is utilized on various patch antenna arrays for directing the main beam towards the desired signal and eliminating interference from other directions. In Fabiani et al. (2018), researchers are also employing the LMS algorithm to control the main beam direction, polarization, sidelobes level, and nulls positioning of elements in a circularly-polarised microstrip antenna array. Additionally, the study conducted by Kamath et al. (2019) employed the same LMS algorithm with antenna arrays consisting of 8, 16, 32, and 64 elements. Some researchers utilized an algorithm for beam-steering applications on a high gain substrate integrated waveguide (SIW) antenna array, as demonstrated in Khattak et al. (2017). Three algorithms, including greedy algorithm (GDA), metropolis algorithm (MA), and genetic algorithm (GA), are utilized in combination for antenna array beampattern synthesis in IoT applications in Gorman (2015). An enhanced orthogonal matching pursuit (OMP) algorithm and precise augmented lagrange multiplier (PALM) algorithm were developed for sparse array pattern synthesis with a minimal number of elements by Buttazzoni et al. (2020).

Moreover, employing multiple-input-multiple-output (MIMO) in digital beam-steering applications is appealing. In a study by Krishna et al. (2018), *SystemVue's W1720*

phased array beamforming kit was used to integrate the built-in LMS algorithm into a microstrip planar array for flexible radiation patterns and beam-steering capabilities. According to Truong et al. (2019), the OMP algorithm integrated with beam-steering technique, improves the performance of dual-polarised large scale antenna array. A different algorithm named sequential convex optimizations (SCO) has been utilized in antennas with linear and planar arrays by Qi et al. (2019). According to the study by Fuchs and Rondineau (2016), they utilized comparable convex optimization techniques to create antenna array patterns while managing the phase excitations. According to research conducted by Tokan and Gunes (2008), SVM could also be utilized to optimize the design of a rectangular microstrip antenna. The outcome indicated that utilizing optimization algorithms in antenna design results in improved and more precise characterization compared to theoretical findings.

Additionally, Gianfagna et al. (2015) also explores the implementation of the bayesian regularization algorithm along with the configuration of a planar inverted-F antenna (PIFA). It was concluded that optimization methods could greatly help reduce errors and speed up the process of synthesizing new materials, as well as predict antenna behavior without needing lengthy simulations. Increasing the amount of data samples used with the algorithm could lead to improved results.

In addition to traditional algorithms, blending optimization with evolutionary algorithms has been shown to achieve quicker convergence rates and comparable solution quality when compared to optimization methods like self-adaptive differential evolution and wind-driven optimization (Gregory et al., 2011) and (Bayraktar et al., 2013). The research article by Liu et al. (2013) examines the optimization of inter-chip antenna design, a four-element linear antenna array, and a 2-dimensional array. They utilized surrogate model-assisted differential evolution for antenna synthesis (SADEA) which merges Gaussian process with a differential evolution (DE) algorithm. Research demonstrated that SADEA improved the design and optimization process speed by over four times in comparison to DE.

The use of evolutionary algorithms was successful in improving the distribution network for planar antenna arrays. Research conducted by Chen et al. (2007) utilized a

genetic algorithm to enhance the excitation weights of planar arrays in satellite communications. Optimizing each element in large planar arrays would result in complex feeding networks and increased system expenses. This describes how the extensive array is divided into various separate subarrays that are controlled by a single node. Afterwards, the issue is addressed using a clustering technique called the K-means method. As proven by the study conducted by Shi et al. (2021), the generated pattern shows significant amplification towards the target signal direction and displays reduced peak-sidelobe-level when compared to the current best method.

In today's world, with the fast advancement of computer technology, a greater number of optimization algorithms are being used in antenna optimization. These adaptable algorithms could be utilized to address complex and non-linear optimization issues, resulting in improved optimization performance and increased flexibility in synthesizing antenna array patterns. Only a small number of optimization problems are solvable, including sidelobe suppression, null depth, and main beam-steering. Controlling sidelobe levels and positioning nulls in the interference signal direction allows for beam-steering in phased antenna arrays.

Array pattern synthesis plays a crucial role in array processing as array weights are utilized to shape the antenna's beam pattern to align with a specific desired pattern. By utilizing machine learning, beam pattern synthesis could manage large amounts of data in a more efficient manner. Earlier studies have demonstrated the utilization of traditional optimization techniques for incorporating array pattern synthesis into beam-steering functionalities. Furthermore, it could be inferred that machine learning enables a quicker antenna design process without sacrificing accuracy, reduces errors and saves time, predicts antenna behaviour, improves computational efficiency, and decreases the need for extensive simulations. These benefits could be utilized for the aim of this research, which involves optimizing the weight coefficients of a patch antenna array for the ability to steer beams, using deep neural networks.

Studies like (Alam et al., 2024) and (Kim & Choi, 2020) faced scalability issues because dataset generation involved considering all combinations of phase excitations, making them non-scalable for large arrays. AEP-DNN uses fixed phase differences and

active element patterns to build a more efficient dataset, significantly reducing training complexity while maintaining predictive accuracy for beam pattern synthesis.

(Liang et al., 2023) and others used DNNs trained on ideal array factor theory, which ignored mutual coupling effects, causing main lobe could not be steered accordingly during real-world testing. In contrast, the AEP-DNN approach incorporates mutual coupling via active element patterns, leading to more realistic and accurate beam predictions.

Many previous studies focus only on linear or circular arrays without dual polarization (Montaser & Mahmoud, 2021), or do not fully address 5G-relevant 28 GHz operation. This proposed method integrates dual-linearly polarised array design, AEP modeling, and DNN to achieve wide-angle scanning, low RMSE, and low computation time, while maintaining accuracy at millimeter-wave frequencies.

Compared to encoder-decoder structures (Cui et al., 2021) or ConvNets (Shan et al., 2021), AEP-DNN is simpler, lightweight, and faster. Once trained, it could instantly predict optimal phase shifts, making it highly suitable for real-time 5G applications where delay is critical.

Therefore, integrating beam-steering capability to the antenna array at 28 GHz is showing to be a challenging task in this study. The primary objective of optimization is to attain the desired main beam in a particular direction while maintaining an acceptable average level of sidelobes according to simulated results. This means that the primary objective is not to reduce sidelobes beyond -30 dB, but to attain the desired main beam direction while taking into account the ideal level of sidelobes.

2.7.1 Full-Wave Modelling and Pattern Multiplication Method

Full-wave modelling with Computer Simulation Technology (CST) involves using CST's specialized electromagnetic simulation software to solve Maxwell's equations in three dimensions. This approach simulates electromagnetic fields in complex environments, capturing the full "wave" behaviour of the fields, including phase, amplitude, and interference. CST provides several solvers and methods to support various types of full-wave modelling, commonly used in applications like antenna design, microwave circuits, radar, and biomedical simulations.

Full-wave simulations use Maxwell's equations to accurately predict the behaviour of electromagnetic fields. This includes solving for electric and magnetic fields (*E* and *H*) as they propagate and interact with objects. CST Studio Suite uses a variety of numerical methods for electromagnetic simulations, each suited to specific types of problems. In this study, the CST has been used to simulate the antenna design using a numerical technique that solves Maxwell's equations in the time domain to simulate electromagnetic pulses such as the finite-difference time-domain (FDTD) method. FDTD is a popular method for simulating complex electromagnetic devices because it could assign a different electric and magnetic properties to the grid, supports different boundary conditions, simulates various types of materials, and covers a wide frequency range with a single simulation run.

However, CST simulations could be computationally expensive, especially for large, complex models or high-resolution meshes. The time and memory required to solve full-wave problems could grow quickly with the size of the model, leading to long simulation times and significant hardware requirements. For large-scale problems, such as simulating entire radar systems or large antenna arrays, CST simulations could take a long time to complete. Despite optimizations in parallel computing, the solution time increases with model complexity and the size of the problem. While CST has optimization capabilities, running parameter sweeps or optimization algorithms on complex models could be time-consuming. This becomes a challenge in real-time applications where fast

iteration is required. Its drawbacks primarily stem from the cost, complexity, and computational demands.

The pattern multiplication method (PMM) in antenna theory is a technique used to predict the overall radiation pattern of a composite antenna system that consists of multiple antenna elements, such as an array of antennas. It involves multiplying the individual radiation patterns of the antennas in the array to obtain the combined radiation pattern. The total radiation pattern is the product of the single element pattern and the array factor. It does not directly account for mutual coupling or interaction between elements when determining the element pattern. The method treats the element radiation pattern as if it is unaffected by the presence of other elements in the array. It provides an approximation of the overall radiation pattern assuming that elements do not interact strongly with each other. It is less accurate when mutual coupling is significant.

2.7.2 Active Element Pattern

AEP is defined as one element in the array that needs to be excited while the rest are terminated with matching loads. AEP only impacts some of the array and spreads the modified loads across all elements except one. Consider first a uniform linear array with N numbers that are all the same, as shown in Figure 2.22. The radiation pattern is derived by multiplying an element factor by an array factor in conventional array theory, which ignores the mutual coupling effect between elements. It is also called the pattern multiplication method (PMM). The pattern of one element from the array, isolated, is the element factor, $f_i(\theta)$ (Pozar, 1994). This is because it is assumed that all elements follow the same patterns. These factors would result in inaccuracies when designing antenna arrays. Mutual coupling occurs when neighbouring elements in an array interact electromagnetically due to their close placement. The radiation pattern of the entire array would be greatly impacted as the distance between the elements decreases. Each element's current is influenced by its own

excitation and the current induced by adjacent antenna elements. This could be overcome by using the AEP method (Pozar, 1994).

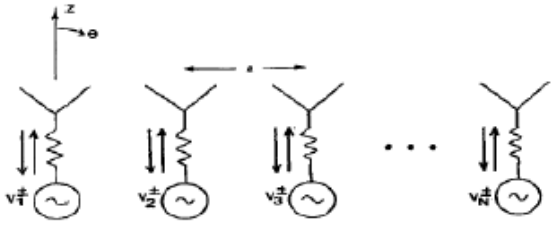

Figure 2.22 The Configuration of a Uniform N-Element Linear Array (Pozar, 1994)

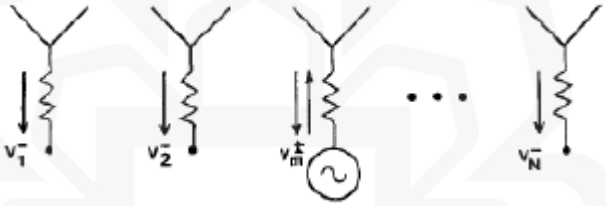

Figure 2.23 The Configuration for the AEP of a Uniform N-Element Linear Array (Pozar, 1994)

To determine the AEP, $F_e(\theta)$, the array in Figure 2.22 is swapped out for the array in Figure 2.23. All other elements with matched loads have been ended, as indicated in Figure 2.23, in place of the N feeds in Figure 2.22, which were replaced with a feed on a single array element. Because of this, the isolated element pattern, $f_i(\theta)$, and the AEP, $F_e(\theta)$ are different. Table 2.3 shows the summary of comparison between the full-wave modelling (CST), PMM, and AEP methods.

- Because of mutual coupling with the feed element, the AEP consists of radiation from nearby elements.

- The AEP, $F_e(\theta)$, changes depending on the position of the feed element within the array; edge elements have a distinct AEP compared to those in the centre. The proportion of edge elements compared to other array elements is very small and could be ignored in large arrays, so the AEP could be estimated as being the same for all array elements. The pattern of the fully excited array in Figure 2.23 is determined by the AEP and the array factor when assuming the AEP is consistent across all elements.

Table 2.3 The Summary of Comparison between the Full-Wave Modelling, PMM, and AEP Method

Aspect	**Full-wave Modelling (CST)**	**PMM**	**AEP**
Concept	Full-suite simulation tool for electromagnetics	Multiplying element pattern and array factor	Accounting for mutual coupling and active currents on each element
Coupling consideration	Fully accounted for in complex systems	Assumes independent elements, no mutual coupling	Accounts for mutual coupling between elements
Use case	Broad (antenna arrays, circuits, waveguides, etc.)	Suitable for non-interacting or well-separated arrays	Suitable for arrays with significant mutual coupling

Mathematical complexity	High complexity, could simulate large systems with arbitrary geometries	Simpler, less computationally intensive	More complex, requires solving mutual impedance and coupling
Accuracy	Very high accurate, could simulate realistic environments	Less accurate in arrays with strong coupling	Accurate, especially for closely spaced elements
Computational cost and time	Very high	Low	Low

2.8 DEEP NEURAL NETWORK

Artificial neural networks (ANNs) are seen as the artificial version of the human brain in terms of both their structure and function. The human brain is a complex and interconnected system of nerve cells. The complex design could efficiently perform difficult and complex tasks with surprising ease. This structure's creativity greatly impacts how the brain performs different tasks. The brain effortlessly performs a range of nonlinear tasks such as math, logic, decision-making, and more. The ability of the human brain and neural system to acquire knowledge and create new concepts through experience is a essential characteristic.

Scientists have been researching the structure of the human brain for a long time, but it was not until the 1950s that efforts were made to replicate biological neuron structures. In 1943, McCulloch and Pitts demonstrated the fundamental structure of neurons and utilized them as representations for real neurons. During the 1950s, artificial neural networks became widely utilized (Fyfe, 2005). Artificial neural networks are widely recognized and highly popular in the scientific community. ANNs are utilized in various

fields to perform extremely complicated tasks. ANNs are predominantly utilized in medical applications for image processing, as indicated by Khashman et al. (2020). Artificial neural networks are also utilized in communication systems, weather forecasting, prediction of forecasting and pricing, control techniques, and systems. In the field of communication, particularly in smart antenna applications, artificial neural networks are also applicable (Sadiq et al., 2022) and (Shi et al., 2022).

ANN are models of data processing that are based on the structure and behaviour of biological neurons. They consist of connected units called artificial or formal neurons. An artificial neuron communicates with neighbouring neurons using weights and could activate itself by processing received signals, enabling simultaneous decision-making while considering the network's collective state. Neurons are connected and organized in layers to form a network. Compared to the desired outcome, the network links outputs to a particular input setup. The network alters the synaptic weights (key components of neurons) to minimize the error that has been accumulated.

By manipulating radioelectric or geometric aspects and considering established criteria, the neural network could design and enhance antenna arrays. The neural network allows for great flexibility between the input and output system parameters while also creating important analytical equations for optimization. Because of the clear connection established by the neural network, this optimization stage is now possible. Multi-layer back propagation network is a frequently utilized neural network for antenna array synthesis. Yu-Chi Ho and others introduced this method in 1969, and it was later utilized by Rumelhart, Werbos, and others in ANN applications in 1974.

Figure 2.24 illustrates the three fundamental layers which include the input layer, the hidden layer, and the output layer. The input layer presents data to the network which the neurons interpret. An uncertain quantity of inner layers is known as the "hidden" layer. The number of neurons in the output layer is equal to the number of expected responses. The neurons within a layer do not have connections to each other.

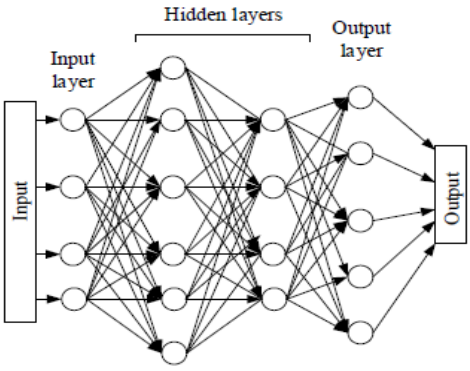

Figure 2.24 The Multi-Layers Perceptron Networks (Singh & Banerjee, 2019)

There are two steps for back-propagation learning algorithm that includes:

1. A propagation step includes developing an input configuration for the network, then gradually propagating this configuration from the input layer through the hidden layers up to the output layer.
2. A back-propagation step includes the process of propagation, in order to minimize the obtained error during the entire process. This error is considered a function of the synaptic weights (*W*). The error represents the squared sum of distances between the determined responses (*S*) and the desired ones (*Y*) for all samples contained in the learning process. This process continues to recalculate the synaptic weights of the network until the number of epochs is reached or the error is less than the desired goal. Figure 2.25 illustrates the back-propagation learning.

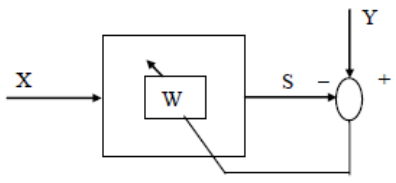

Figure 2.25 The Back-Propagation Learning (Singh & Banerjee, 2019)

ANN has one hidden layer while a neural network with two or more hidden layers is referred to as a deep neural network (DNN). The DNN includes a wide range of network structures such as the multilayer perceptron (MLP), convolutional neural network (CNN), and generative adversarial network (GAN). MLP is an ANN type consisting of multiple layers of neurons. CNN is a specialized neural network type designed primarily for processing grid-like data such as images. CNNs are particularly effective for tasks like image recognition, object detection, and visual classification as they could automatically learn hierarchical features from raw input data. GAN is a class of machine learning models used for generative tasks, like creating new data resembling existing data.

According to the study conducted by Bianco et al. (2020), researchers introduced a deep CNN algorithm that uses an image of radiation pattern as the input pattern to calculate the optimal currents for achieving a new beam specification through the CNN structure. By implementing a smart CNN architecture and avoiding excessive iterative optimizations, this technique could reduce the amount of time needed by up to 1700 times to find the desired currents.

Furthermore, research conducted by Shan and Li (2019) has explored the forecasting of phase shift in an antenna array, demonstrating remarkable precision using a deep CNN-based *AlexNet*. The model uses the radiation pattern and beam direction to forecast the phase shift with an error margin of under 0.4%. The CNN methodology was demonstrated in Lovato and Gong (2019) to forecast the phase angle based on a 2D radiation pattern, achieving precise phase calculations for synthesizing the radiation pattern.

According to the research conducted by Cui et al. (2021), the study aims to use the MLP neural network with forward and back propagation structure in both the encoder and decoder design. The objective is to create a focused beam pattern constrained by masks for any linear array geometry using an encoder-decoder ANN framework. This technique efficiently completes computational tasks in a significantly shorter amount of time and is considered a promising choice for real-time array synthesis.

In the case of the extensive array's use, there might be hundreds or even thousands of components in an antenna that require multiple rounds of iterations to reach a final array design resulting in the desired radiation pattern. When multiple parameters need to be taken into account, these computational iterations become both complex and time-consuming. Hence, optimization methods are implemented to enhance the effectiveness of the array synthesis procedure. The optimization method assesses a radiation pattern by varying excitation weights and element positions. Each step of the automated process helps determine how closely the obtained pattern matches the desired one. To achieve the objectives of the procedure, it is crucial to have a thorough grasp of the various design possibilities and limitations involved. The factors that would dictate the radiation or beam pattern features include the amplitude and phase excitation coefficients assigned to each element, as well as the element's position or spacing within the array.

Optimization methods could offer a broader approach to generating desired patterns under stricter requirements and constraints. Although optimization-based algorithms are highly adaptable, they might require an extended period to reach the optimal solution when dealing with large arrays. When it comes to dynamic situations, it becomes more difficult to create a specific beam pattern in real-time.

Traditional methods like local or global optimization or matrix inversion are not appropriate for use in a short-term project. Traditional optimization methods might require numerous iterations or complicated calculations to reach an optimal or suboptimal solution, leading to a lengthy convergence process. Current neural network architectures have proven to serve as universal approximators as their parameters approach infinity, enabling them to calculate complex relationships between inputs and outputs and improving performance across a range of tasks. Therefore, using a DNN could help in resolving the problem.

2.8.1 Deep Neural Network Structure

Every neural network requires three key attributes and a specific training algorithm in order to carry out a given task effectively. The primary components include the weights, transfer functions, and layers. These are the primary functional components of a neural network structure. The algorithm used to adjust the neural network in order to accomplish the necessary task is known as the learning process.

The weights are the adaptive memory within the neural network that stores knowledge. During the learning process, the weight values are adjusted repeatedly until the optimal values are determined. These perfect values are achieved when the neural network produces output that matches the desired output. Next, storage parameters are used to store expert networks for future tasks. The weights of a neural network are vital in determining the network's performance.

Transfer functions quantify how well artificial neurons process inputs. Upon receiving inputs from various layers weighted by specific values, the transfer functions determine the strength of the output signal for the subsequent layer. The importance of transfer functions lies in their ability to determine the significance of a specific input. Different applications require various types of transfer functions.

The new and latest reliable transfer functions in neural network, Rectified Linear Unit (ReLU) function is typically used in all hidden layers (Arora et al., 2016), the ReLU function is a rectified linear unit function shown in Figure 2.23 and defined as follows in Equation 2.13 and 2.14.

$$f(x)= 0 \qquad x<0 \tag{2.13}$$

$$f(x)> 0 \qquad x>0 \tag{2.14}$$

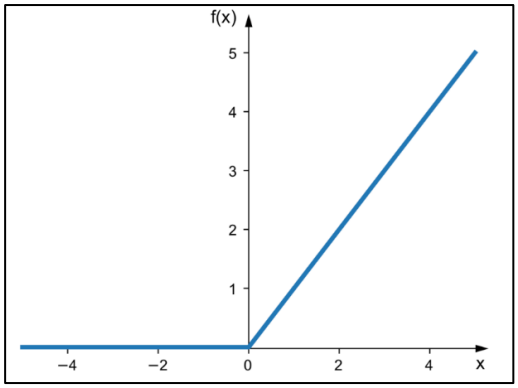

Figure 2.26 The ReLU Activation Function (Arora et al., 2016)

ReLU is a piecewise linear function that outputs the input directly if it is positive, otherwise it outputs zero. It has become the default activation function for many types of neural networks because a model using it is easier to train and often achieves better performance. The simplest activation function is linear activation, involving no transformation at all. Linear activation functions are still used in the output layer of networks that predict a size.

Traditionally, the sigmoid and hyperbolic tangent activation functions are two commonly used nonlinear activation functions. These nonlinear activation functions do not offer valuable gradient information for deep layers in extensive networks. The error is passed through the network to adjust the weights. Given the derivative of the selected activation function, the error propagates through layers at a significantly reduced rate. The issue of the vanishing gradient is what makes it challenging for deep (multilayer) networks to learn effectively (Goodfellow, 2016).

An activation function with linear behaviour is needed for training deep neural networks with stochastic gradient descent and error back-propagation, despite being nonlinear. This allows for the establishment of very complex connections within the data. The function should prevent mild saturation and provide increased sensitivity for the activation sum input as well. The beginning of ReLU could be seen as one of the key moments in the advancement of deep learning, alongside the techniques enabling the

routine development of highly complex neural networks. Training a neural network with backpropagation results in the function displaying similar characteristics to a linear activation function, as it shows linearity for values above zero. Since negative values are consistently shown as zero, it becomes a non-linear function. The rectified function is called a piecewise linear or joint function as it is linear for one half of the input range and non-linear for the other half (Goodfellow, 2016).

The rectifier function looks and acts like a linear activation function. Usually, if a neural network exhibits linear or near-linear behaviour, the process of optimization becomes easier. As long as the node activations remain proportional to the gradients, networks using this activation function could largely prevent the problem of vanishing gradients. Significantly, the identification and implementation of the rectified linear activation function enabled the effective training of deep multilayer networks with a nonlinear activation function using backpropagation, with the advancements in hardware technology (Goodfellow, 2016).

According to the paper by Hammad (2024), the ReLU function is computationally simple because it eliminates the need to calculate the exponential function in activations. Furthermore, the important advantage of the rectifier function is its ability to produce an actual zero value. The *tanh* and *sigmoid* activation functions, however, aim to approximate a zero output, meaning a value that is nearly zero but not exactly zero. Consequently, the hidden layers of neural networks might be activated to incorporate one or multiple actual zero values. This implies that negative inputs could produce genuine zero values as output. Sparse representation, a key aspect of representational learning, is desirable as it could facilitate learning and simplify the model (Goodfellow, 2016).

Layers are a crucial component in the structure of all neural networks. The main function of the neural network is derived from the connections between successive layers. Information is moved through various levels from one layer to the next during processing. Every tier gets information from the tiers before it, works on that information, and passes it on to the next tier. Layers are split into three distinct types: input layers receive data from systems, output layers show results or communicate with other systems, and hidden layers in between facilitate data flow.

1. Input layers: The input layer serves as the entry point in a neural network configuration. It transfers the signal from the inputs to the hidden layers.
2. Output layer: Final stage of processing in a network is known as the output layer, which produces the result of the processing. The outcomes of this level should align with the desired outcomes in a network that has been properly trained.
3. Hidden Layers: The core of the neural network lies in the hidden layers. It might consist of one, two, or multiple layers with varying weight patterns. In contrast to the input and output layers, that depend on the data set for their size, the size of the hidden layers is only restricted by the processing power available. Weights in the hidden layers are iteratively adjusted until a satisfactory result is achieved.

2.8.2 Deep Neural Network Hyperparameters

Hyperparameters are the variables that build the network structure and influence the method of network training. They are set before the process of network training. In this study, there is a nonlinear regression problem that needs to be solved using a deep learning network and involves a few hyperparameters within a network structure. The hyperparameters involved are layers, number of hidden units or neurons, epochs, batch size, learning rate schedule, and others.

There are many types of interconnected layers consisting of input layers, convolutional and fully connected layers, sequence layers, activation layers, normalization, dropout, and many others. However, the nonlinear regression network in this study only consists of a sequence input layer, ReLU layers, dropout layers, and fully connected layers.

The '*sequenceInputLayer*' function is used as the input layer of a deep neural network (DNN) since the input is a set of sequences. It serves as an input layer for sequences in a network. An activation function within a neural network explains how a

node or multiple nodes within a network layer convert the sum of the input's weights into an output. The transfer function is a different term for the activation function. When the range of the activation function's output is limited, it could be called a squashing function. The nonlinearity present in the layer or network structure is due to most activation functions being nonlinear. The utilization of different activation functions in different parts of the model could have a significant effect on the neural network's capacity and effectiveness. ReLU layers are utilized for both the input and hidden layers in this research. The MLP network consists of connected layers that multiply the input by a weight matrix and then add a bias vector. The '*fullyConnectedLayer*' function serves as the regression layer in the output layer. It calculates the loss of half the mean squared error for regression tasks.

For the hidden layers that consist of fully connected layers, the output size of neurons that passed to the next layers is returned. The number of neurons ought to be adjusted to the complexity of the problem at hand. More neurons are required for predicting tasks with higher levels of complexity. The values produced by one layer are subsequently used as the input values for the following layer. Next, the following layer processes the values to generate output values for yet another layer. The dropout layer labelled as '*dropoutLayer(0.5)*' is originally configured with a default value of 0.5. The dropout layer is included within the hidden layers to prevent the overfitting of data.

Epochs represent how many times a full set of data is processed by the neural network model. The training dataset is sent back and forth through the neural network only once during an epoch. Underfitting could happen when there are not enough epochs because the neural network is still in the learning process. Multiple iterations through the training dataset or epochs are required. However, excessive epochs lead to overfitting, which means the model could predict existing data well but struggles with new, unseen data. To attain the best results, the number of epochs should be adjusted.

Giving a batch size would help the model learn faster by not processing all training data at once. The batch size is the amount of training data subsamples for the input. Even though the smaller batch size accelerates learning, it also causes higher accuracy variance in the validation dataset. Although it takes more time to learn with a larger batch size, the validation dataset's accuracy is more stable.

The learning rate is a hyperparameter of the optimizer, and it would speed up learning. The learning rate controls the size of the step needed for a model to achieve the minimum loss function. The model learns faster when the learning rate is higher, but it might not reach the minimum loss function and only approach it. Discovering a function with minimal loss is more with a decreased learning rate. A slower learning rate requires extending epochs or allocating additional time and memory resources.

Weight decay is a regularization technique commonly used in deep learning. Weight decay works by adding a penalty factor in the cost function of a neural network, resulting in the reduction of weights during backpropagation. Furthermore, this prevents the network from overfitting the training data and avoids the issue of the inflating gradient problem. Neural networks have two adjustable parameters, biases, and weights. Because the weights are multiplied by the inputs, they directly influence the neural network's understanding of the connection between inputs and outputs. The distortions are the only imbalance mathematically corresponding to the relationship originating from the junction point. Therefore, we typically only standardize the weights. The L2 penalty is the term most used for regularizing neural networks. By incorporating L2 regularization, a manually chosen hyperparameter lambda that scales the error term by adding the squared sum of the weights to it is included.

The dataset utilized for training a neural network usually contains random fluctuations without explanatory value and patterns related to the problem being addressed. Our goal is to acquire as much knowledge as possible about the patterns by training the network to avoid of random fluctuations. As our weights increase, our neurons become more active. With this added power, they would make the most accurate modifications to the training data. Therefore, they are more inclined to detect additional background noise.

Reducing the weights of certain neurons to almost zero essentially deactivates them. The weights decrease as the Lambda regularisation value is increased. Weights do not get fully reset following L2 regularization. Even though the neurons remain theoretically active with L2 regularisation, they play a minimal role in the overall learning process. Because of its reduced performance, the network needs to prioritize patterns that are widespread in the dataset and closely resemble the actual problem it aims to predict. Therefore, the model

also becomes more gradual in response to changing inputs, resulting in smoother output changes.

The learning rate schedule aims to adapt the learning rate throughout training by decreasing it based on a predetermined schedule between epochs or iterations. In this study, the default learning rate schedule is used, which is a constant learning rate. The starting learning rate is preset and remains constant during training. This timetable maintains a consistent learning rate during the training process.

The gradient threshold is set to "1" because the highest input scalar value of the DNN model is 1. Hence, the gradient curve would be limited by the learning process if it surpasses this threshold. The default values for the gradient decay factor and squared gradient decay factor are 0.9 and 0.99, respectively. ADAM is an optimizer that involves incorporating a momentum factor in the parameter update.

In this study, ADAM is being used to train the neural network model as it is more recent, computationally efficient, and faster algorithm where the learning rates are computed for each parameter. This algorithm is especially useful in the case of optimization problems with relatively huge amounts of data or with big numbers of parameters. It could improve the performance of DNN model (Jais et al., 2019).

2.9 AEP-DNN METHOD

Machine learning advancements have significantly enhanced electromagnetic research, as demonstrated in previous sections. However, there are certain drawbacks associated with machine learning techniques. Since machine learning methods depend on data, significant constraints arise when there is not enough data to adequately train the model. Additionally, because machine learning makes it easy to make predictions, the accuracy might decrease in unfamiliar situations, necessitating ongoing evaluation and improvement of the model. Surrogate modelling has significant potential, but it requires adequate empirical data and

precise hyperparameter tuning to achieve the desired outcomes. It frequently functions ineffectively when faced with higher dimensions and significant nonlinearities. The accuracy of the model depends heavily on the amount of data used during training, with additional factors such as learning rate, batch size, and others playing a crucial role in improving and optimizing results (Shrestha & Mahmood, 2019).

In summarizing the uses of neural networks in synthesis, the main drawback is the need for a large dataset to achieve high accuracy, which could lead to increased computational complexity in deeper models. Nevertheless, the benefits of utilizing neural networks in synthesis applications outweigh the drawbacks as they offer higher accuracy, high adaptability, fast estimation, and are also efficient in handling large feature space. In this study, the dataset samples for training are quite large, however, it is not a significant challenge to compute the desired outputs as the computational tasks are being handled by a large and sufficient disk space of CPU processor, AMD Ryzen 3 3200U with Radeon Vega Mobile Gfx 2.60 GHz, and 8 GB RAM. In this study, the elements' positions and amplitudes weight coefficient are fixed, hence this study only involves optimization of phases weight coefficient of the 4 elements of proposed dual-linearly polarised antenna array (DLPAA) to get the desired direction of the main beam pattern.

He et al. (2022) proposed an amplitude-only technique that combines genetic algorithms (GA) and artificial neural networks (ANN) to generate a uniform linear array pattern with deep zeros and low sidelobes. This approach offers faster convergence, prevents local optima, and has minimal computational complexity compared to current methods. The technique effectively generates desired patterns in challenging situations by leveraging the efficient data adaptability and fast computation speed of ANN. It could address diverse optimization challenges in array signal processing without significant performance decline.

Montaser and Mahmoud (2021) developed a DNN-based bone-shaped patch antenna (BSPA) for 5G applications operating at 28 GHz and 38 GHz. A DNN model with adaptive learning rate was trained on a dataset of 150 BSPAs using a combined particle swarm optimization (PSO) and modified version of the gravitational search algorithm (MGSA) optimization approach. The model was tested on BSPAs with different geometries

to establish a database for training and testing. The antenna array's main beam shape was adjusted using DNN and weighted MGSA-PSO algorithms to minimize sidelobe levels.

A novel array synthesis technique using artificial neural networks (ANN) is proposed based on Cui et al. (2021). The encoder-decoder-based framework successfully synthesises mask-constrained beam patterns for linear arrays with focused or shaped beams. The encoder predicts array activations for a specific radiation pattern, while the pre-trained decoder generates the real radiation pattern. Simulations demonstrated that the ANN-based method performs better in computational efficiency and pattern accuracy compared to traditional methods. The framework was validated on different array types and configurations, showing flexibility in adapting to amplitude and phase control requirements, including mutual coupling effects.

The study by Iye et al. (2022) introduces a new method for estimating inter-element phase using a neural network and linear phased array radiant power pattern. The proposed method only requires one measurement of the radiation pattern, making it more efficient in terms of time. The study also suggests a way to reduce estimation errors by repetitively inputting patterns into the neural network model. This method is crucial for calibrating experimental phase in a linear array.

Authors investigated using deep learning for reflectarray antenna phase synthesis. They created a *ConvNet* with *AlexNet* architecture to forecast the phase distribution based on the beam pattern. The *ConvNet* was trained using an array-theory method dataset. It could quickly and accurately predict with less than 0.7% error, showing deep learning's potential for reflectarray phase synthesis (Shan et al., 2021).

Liang et al. (2023) proposed a new algorithm using DNN to compute the array factor and AEP for beam-steering on antenna arrays. Deep learning calculates amplitudes and phases for pattern synthesis, but predicted phases are based on the main lobe direction, not the overall pattern, leading to a mismatch in the main lobe direction due to neglect of mutual coupling effects in the array factor theory. AEP is used instead of full-wave modelling (CST) for simulation to confirm the main lobe direction.

Recent research has found ways to improve radiation patterns in a closely connected antenna array with a 0.5 λ inter-element spacing. The method involves using neural network-based techniques to determine complex antenna weights for each element, training on different input radiation patterns from high frequency simulation software (HFSS) simulation. A study by Kim and Choi (2020) applied DNN to a 4-element antenna array to create a radiation pattern resembling an ideal one, yielding precise and adaptable results. However, limitations exist due to the non-scalable dataset generation method, necessitating extensive training even for small arrays. As the array size increases, the training dataset grows rapidly, hindering practicality for larger arrays. To address this, future research aims to explore diverse array structures and sizes while managing dataset size to prevent increased computational complexity and advance 1-dimensional radiation pattern synthesis knowledge.

Alam et al. (2024) studied the application of deep neural machine learning in creating radiation patterns for 8-element active electronically scanned antenna arrays. The study focused on providing 181 points of a desired radiation pattern as input to the DNN, which then generated the phases of the array elements as outputs. The research showed that traditional neural network methods were not effective for higher-order arrays due to the large dataset size. By utilizing the constant phase-shift feature of the antenna, the dataset size was significantly reduced, improving speed and complexity, especially for real-time applications. The effectiveness of the techniques was validated through MATLAB and CST simulations, using benchmark inputs and testing datasets. Instead of considering all possible combinations of phases of each element, the second approach creates the dataset by focusing on the fixed phase difference between array elements. This method is beneficial because knowing the phase-shift allows for easily determining the phases of individual elements. Therefore, by utilizing the consistent phase difference among array elements, this approach could efficiently execute the suggested AEP-DNN method.

Based on previous works investigating pattern synthesis using traditional and combination of traditional and machine learning, it shows that these works rely on the initial estimation of weight coefficients using optimization conventional methods. This method contributes to a redundant process to execute optimal results. In aiming to reduce

complexity and time-consuming of neural network structure, a novel technique is introduced and named an integration of active element pattern and deep neural network (AEP-DNN) algorithm method to carry out the pattern synthesis of proposed DLPAA. AEP has been used to calculate the initial input radiation pattern of training and validation datasets for DNN algorithm. The input radiation pattern of test datasets is obtained using phase difference between array elements. The predicted DNN pattern is also calculated using AEP computation inside MATLAB as shown in Appendix A.

Integrating an AEP with a DNN for pattern synthesis in 5G networks offers several advantages, especially given the complex beamforming and adaptive antenna requirements of modern 5G applications. It allows dynamic adaptation of beam patterns in response to real-time environmental changes, such as user location, interference, and multipath effects. This is essential for 5G networks, where mobile users require focused and directional beams. The DNN could learn from previous data and real-time feedback to optimize the pattern synthesis, enabling low-latency, highly adaptable beamforming, which is critical for 5G's high-speed, low-latency applications.

Additionally, by combining the AEP with a DNN, it is possible to synthesise complex beam patterns that might be challenging to achieve through traditional methods. The DNN could handle multiple inputs (like phase and amplitude shifts across different elements), managing the complexity to produce optimal patterns for different scenarios. The approach could support advanced functions like multi-user beamforming, where multiple beams are directed to different users simultaneously, a requirement for 5G's massive MIMO (multiple-input, multiple-output) systems.

Traditional optimization methods for antenna array pattern synthesis could be computationally intensive, particularly for real-time beamforming. With a trained DNN, once the network has learned the optimal synthesis patterns, it could quickly generate solutions, reducing computational load and allowing near-instantaneous adjustments. This faster convergence is beneficial in 5G, where maintaining connectivity and quality for mobile applications users is essential. Table 2.4 shows the summary of previous works on the pattern synthesis for antenna array at 28 GHz using DNN algorithm.

Based on the table, techniques like encoder-decoder models (Cui et al., 2021) or MGSA-PSO-DNN (Montaser & Mahmoud, 2021) required long processing times which up to 210 minutes in some cases. AEP-DNN achieves beam-steering in just 2 to 3 minutes with RMSE as low as 1.3 to 1.5, making it significantly faster and more efficient. Previous studies (Kim & Choi, 2020), (Iye et al., 2022), and (Alam et al., 2024) required large, non-scalable datasets or considered all combinations of phase excitations, which made them impractical for large antenna arrays and real-time deployment. AEP-DNN reduces dataset size by using fixed phase differences and AEP data, enabling more efficient training without compromising pattern accuracy. Prior works like Liang et al. used idealized array factor models, which ignored mutual coupling, leading to main lobe direction errors. AEP-DNN incorporates realistic AEPs into DNN training, ensuring greater pattern accuracy.

Table 2.4 The Summary of Previous Works and this Study on the Pattern Synthesis for Antenna Array at 28 GHz Using DNN Algorithm

Ref.	**Aim**	**Method**	**Type of Polarization and Number of Elements**	**Computational Time (minutes)**	**Training/Validation RMSE or Loss**
(Montaser & Mahmoud, 2021)	Pattern synthesis (phase)	Simulations using CST for DNN database and linked to MGSA-PSO algorithm, MATLAB coded for initial phases	Circular	Not reported	Not reported

		to feed DNN model			
(Cui et al., 2021)	Synthesizing beampatterns in linear antenna arrays including on non-ideal array conditions	Encoder-decoder	Linear 149 (ideal array) 32 (microstrip array) 50 (dipole array)	24.60 (ideal array) 27.00 (microstrip array) 16.20 (dipole array)	Training loss: 0.0003 (ideal array) 0.0008 (microstrip array) 0.0002 (dipole array)
(Iye et al., 2022)	Pattern synthesis using one measurement of the radiation pattern	Inputs the measured radiation power pattern of the antenna array into a neural network to estimate phase errors	Linear 8	210.00	Training and validation RMSE: 0.000176, 0.00801
(Liang et al., 2023)	Pattern synthesis using AF and AEP	CST for input phases	Linear 12	18.05	Not reported

2.10 SUMMARY OF CHAPTER

Chapter 2 presents a comprehensive review of existing literature related to antenna design and pattern synthesis techniques, laying the foundation for the proposed dual-polarised array antenna using the AEP-DNN method. The chapter begins with an overview of

important antenna parameters, including reflection coefficient, mutual coupling, impedance bandwidth, radiation pattern, and gain. It discusses the characteristics and advantages of microstrip patch antennas, particularly the rectangular patch, for millimeter-wave applications at 28 GHz. The concept and challenges of phased antenna arrays are explored, emphasizing the effects of inter-element spacing and mutual coupling on beam performance. Dual linear polarization is reviewed as a method to enhance signal reliability and polarization diversity using a single-layer structure, which is especially beneficial in compact antenna designs for 5G. The second part of the chapter focuses on machine learning approaches for antenna pattern synthesis, introducing deep neural networks (DNN) and their architectural components, including layers, activation functions, and hyperparameters. A critical comparison is made between traditional synthesis methods of full-wave modelling and pattern multiplication with the proposed (AEP-DNN) technique. This integration method is positioned as a more efficient, scalable, and accurate alternative for beam-steering predictions in 5G. Unlike previous works that depend on complex optimization or complex models, the AEP-DNN method in this study offers a balanced, efficient, and realistic approach. It incorporates realistic radiation behavior using AEP, supports dual-polarization, scales well for larger arrays, and delivers accurate beam-steering with reduced computational cost, making it superior to earlier methods.

CHAPTER THREE

DESIGN OF DUAL POLARISED ANTENNA ARRAY

3.1 INTRODUCTION

Living in the realm of advanced wireless technology, there are techniques to enhance antenna capabilities for achieving high gain antennas necessary to combat low-quality received signals in mobile applications. Realizing high gain and directive main beam antenna for mobile applications at 28 GHz is a challenging task. One technique is implementing dual polarization signals feature in the antenna. The significant advantage of microstrip patch antennas due to their low profile, light weight, and ease of fabrication has been widely used in wireless communication systems. Therefore, in this chapter, a millimeter-wave dual slant ±45° polarised patch antennas with low profile and simple structure have been designed and simulated by using the CST Studio simulation tool corresponding to the first objective of this study. The aim is to design a high performance dual-polarised antenna array with S_{11} less than -10 dB and a directive main beam pattern. Additionally, the radiation pattern of the dual-polarised antenna array would be verified with the AEP coding from Chapter four. This chapter consists of four sections; dual-polarised patch antenna design 1, dual-polarised patch antenna design 2, dual-polarised antenna arrays, and a summary of the chapter. The dual-polarised patch antenna designs 1 and 2 are based on substrate thickness 0.254 mm and 1.575 mm, respectively. These antennas are designed using Rogers RT5880 substrate material with a dielectric substrate of 2.2 and a loss tangent of 0.0009. The dual-polarised patch antenna designs 1 and 2, as well as the antenna arrays consist of a few antennas listed as follows:

1. A single antenna polarised at +45° (slanting to the right of normal plane) and -45° (slanting to the left of normal plane).
2. A dual-polarised antenna (combination of antenna elements slanting at +45° and -45°).

3. A 1 x 4 dual linearly polarised antenna array (four source ports).

3.2 ANTENNA DESIGN FLOWCHART

The design process of the proposed dual-polarised antenna array was carried out in several steps to ensure it met the required performance as shown in Figure 3.1. The first design used a substrate with a thickness of 0.254 mm. After testing through simulation and measurement, it was found that the antenna did not meet the expected performance as the substrate is too thin, fragile, and easily bent that would cause difficulty in achieving directive main beam's pattern during measurement. In order to improve the results, a second design was created using a thicker substrate of 1.575 mm. This helped improve bandwidth and gain, but the performance was still not fully satisfactory as the main beam pattern is not directional. To enhance the power distribution and polarization performance, an improved T-junction power divider was introduced. The design was tested again, and if it still failed to meet the specification, further adjustments were made to the divider. Finally, a new antenna structure was proposed, combining all the best features from the earlier designs. It was tested through simulation and measurement to confirm it met all requirements, including good S-parameters, radiation pattern, and polarization. This step-by-step method helped to refine the antenna until the final version was ready for fabrication and measurement. The dotted line in the flowchart is excluded from this chapter as the measurement would be carried out in the Chapter 5.

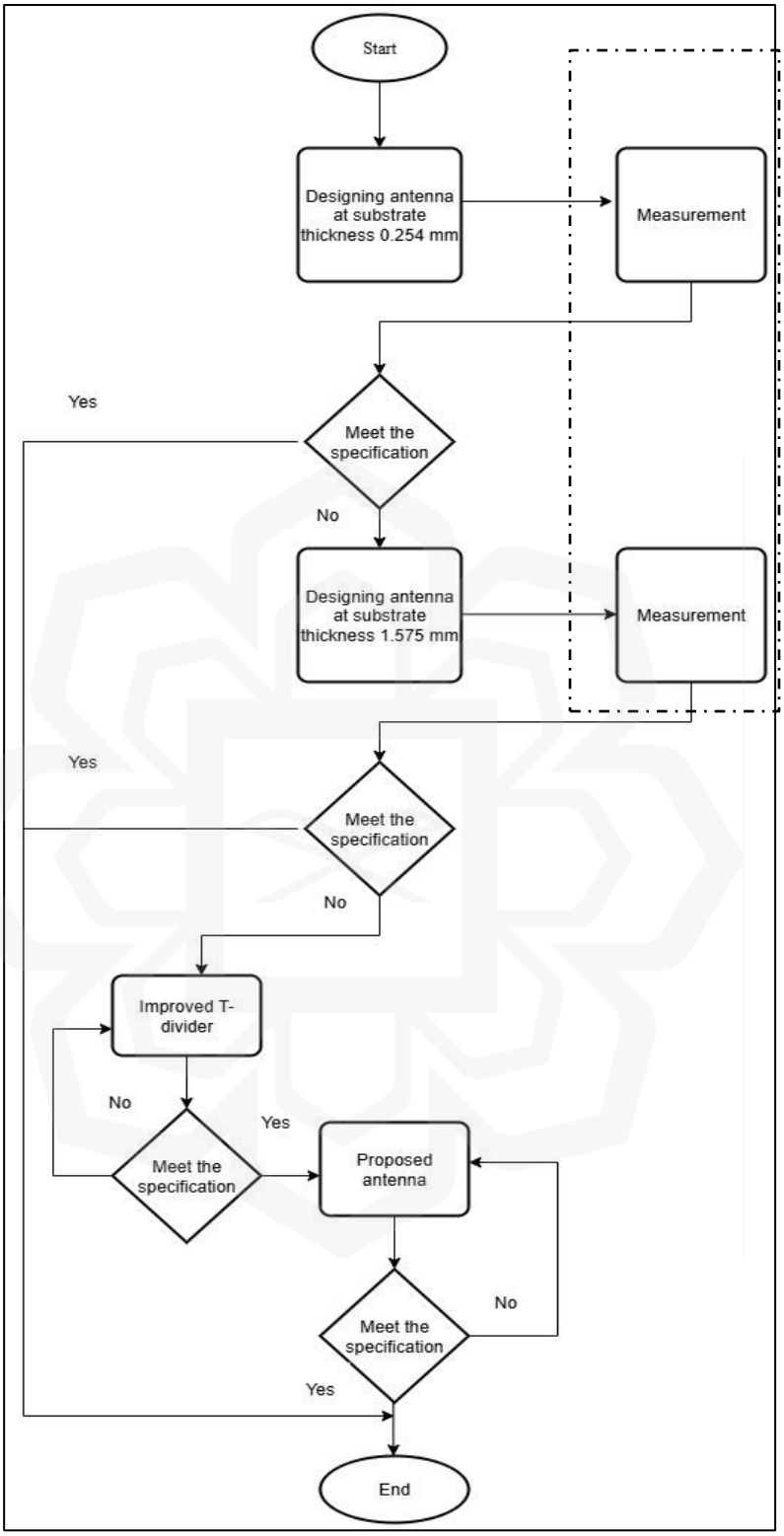

Figure 3.1 Flowchart of Antenna Design

3.3 DUAL-LINEARLY POLARISED ANTENNA DESIGN 1 (SUBSTRATE THICKNESS OF 0.254 MM)

The conventional rectangular patch antenna was mostly applied to singular polarization of transmitted beam signals. In this study, an antenna employing dual polarization transmitted signals has been designed and simulated. The patch elements slanted at +45° would emit the beam at a 45° slant to the right direction of the normal plane, while the patch elements slanted at -45° would emit the beam at a -45° slant to the direction of the normal plane. A combination of these +45° and -45° patch elements by T-power divider with one feed port would emit two transmitted signals simultaneously. This design is chosen to improve the capability of reaching wide transmitted signals angle with the configuration of an antenna array. This sub-chapter of antenna design 1 involves a few simulations on single antennas, combination of single antennas, and its array at a substrate thickness of 0.254 mm.

3.3.1 Rectangular Patch Antenna Elements

The rectangular patch shape is specifically chosen for the dual slant ±45° polarised antenna design of this study. The rectangular shape design for the patch elements is chosen due to its compact size and ease of manufacturing at high frequency. Microstrip patch antenna feeding could be operated in many ways, but this work adopts an inset feeding technique with a coaxial probe at the edge of the antenna instead of coaxial probe feeding via the ground plane. This is because the inset feeding is much easier to implement as the pin of the SMA connector is very small at 28 GHz and works the best for the inset feeding technique. It is also done to reduce the possibility of load impedance mismatch. The impedance matching ought to be set to 50 Ω to minimize signal reflection or maximize power transfer. The formulas for the length and width of the patch, substrate, and ground dimensions are shown in Equation (3.1) to Equation (3.7) below (Darboe et al., 2019).

Calculation of the width of the patch:

$$W = \frac{\lambda_0}{2\sqrt{0.5(\varepsilon_r+1)}} \tag{3.1}$$

Calculation of the effective dielectric constant:

For (W/h>1)

$$\varepsilon_{eff} = \frac{\varepsilon_r+1}{2} + \frac{\varepsilon_r-1}{2}\left(\frac{1}{\sqrt{1+12h/w}}\right) \tag{3.2}$$

where h is the thickness of the substrate.

Calculation of the length extension due to fringing:

$$\Delta L = 0.412h\frac{(\varepsilon_{eff}+0.300)\left(\frac{W}{h}+0.264\right)}{\varepsilon_{eff}-0.258\left(\frac{W}{h}+0.813\right)} \tag{3.3}$$

Calculation of the length of the patch:

$$L = \frac{c_0}{2f_r\sqrt{\varepsilon_{eff}}} \tag{3.4}$$

$$L_{eff} = L - 2\Delta L \tag{3.5}$$

where L is the length of patch before fringing correction and L_{eff} is the effective length of patch after fringing correction.

Calculation of the width of the substrate and ground plane:

$$W_g = W + 6h \tag{3.6}$$

Calculation of the length of the substrate and ground plane:

$$L_g = L_{eff} + 6h \tag{3.7}$$

3.3.2 Single Antennas Design

In this section, a simulation is conducted on the single antenna elements and combination of these single antenna elements at frequency 28 GHz. The aim is to evaluate their performance in terms of reflection coefficient, bandwidth, and radiation pattern. The details regarding the antenna dimensions for both single and dual-polarised antennas are summarized in Table 3.1. All the antenna design simulations are illustrated in Figure 3.2.

Table 3.1 The Single Antenna Elements and Dual Linearly Polarised Antenna Dimensions at 28 GHz (Substrate Thickness = 0.254 mm)

Microstrip patch antenna / **Antenna dimension**	**Single ±45° Patch Antenna**	**Dual-linearly Polarised Antenna**
Width of patch, Wp (mm)	4.20	4.20
Length of patch, Lp (mm)	3.40	3.40
Width of substrate and ground, Ws and Wg (mm)	18.00	56.71
Length of substrate and ground, Ls and Lg (mm)	15.35	15.92
Length of inset feedline, Lif (mm)	1.25	1.25
Gap of feedline, Gf (mm)	0.12	0.12
Length of feedline, Lf (mm)	7.80	7.80
Diameter of the inner conductor, Di (mm)	0.30	0.30
Diameter of the outer conductor, Do (mm)	0.99	0.99

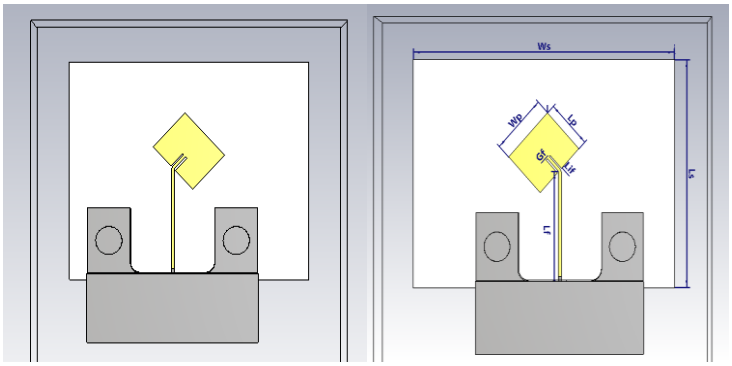

(a) (b)

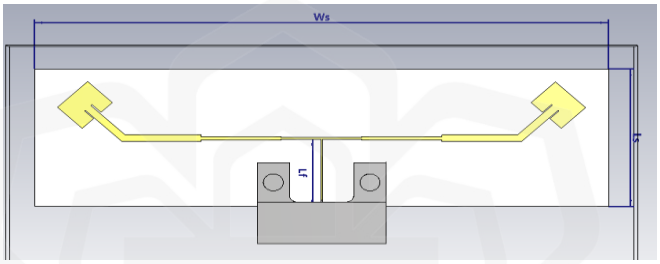

(c)

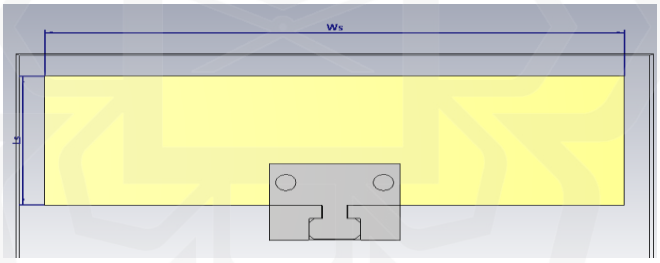

(d)

Figure 3.2 The Antenna Design 1 Simulation of (a) The Front View of a Single +45° Antenna (b) The Front View of a Single -45° Antenna (c) The Front View of a ±45° Dual-Polarised Antenna and (d) The Back View of a ±45° Dual-Polarised Antenna

3.3.3 The T-Power Divider

A T-power divider features a single feed port to uniformly divide the input power and distribute it to each +45° and -45° antenna patch elements has been designed. The impedance of the input transmission line and output lines in the T-power divider is 50 Ω, while for the two-way divider, the impedance between the input and output ports is 70.7 Ω and 100 Ω, calculated using formulas in Ochoa et al. (2017). Figure 3.3 illustrates the T-power divider. The transmission lines were bifurcated into two branches based on the number of patch elements. The T-power divider dimensions are summarized in Table 3.2. The only difference in the T-power divider between antenna designs 1 and 2 is its feeding length L7.

In Table 3.2, the values of L7 are different because of the change in substrate thickness, which affects how signals travel through the transmission line. A thicker substrate causes the signal to slow down, resulting in a longer guided wavelength. To achieve the same phase shift or electrical length, the physical length of the transmission line (L7) should be increased accordingly. All other parameters of the T-power divider are kept the same to maintain consistent impedance matching and signal division. Changing only L7 allows the design to stay simple while still tuning it for better results.

Table 3.2 T-Power Divider Dimensions

Microstrip Patch Antenna / **T-Power Divider Dimension (mm)**	**Substrate Thickness 0.254 mm**	**Substrate Thickness 1.575 mm**
L1	4.84	4.84
L2	5.16	5.16
L3	7.48	7.48
L4	7.80	7.80
L5	7.90	7.90
L6	8.00	8.00
L7	7.80	40.25
W1	0.78	0.78
W2	0.40	0.40
W3	0.20	0.20
W4	0.20	0.20

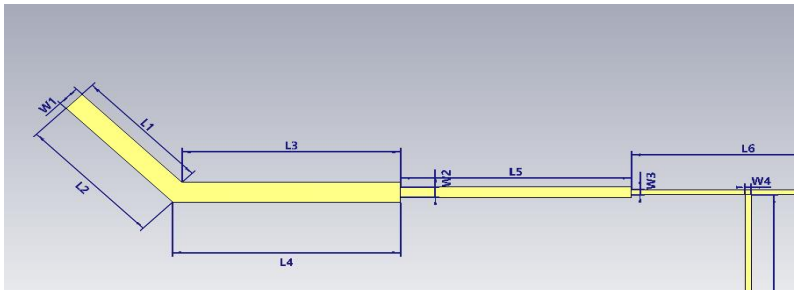

(a)

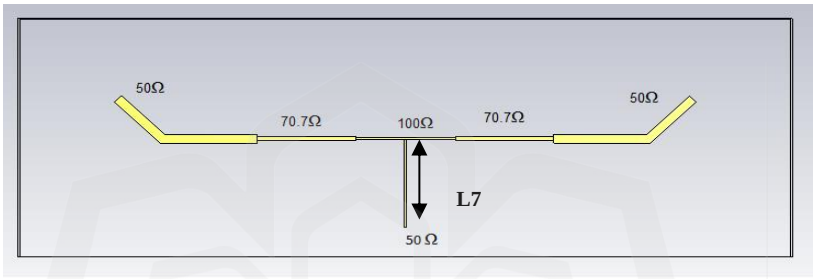

(b)

Figure 3.3 The T-Power Divider of (a) Close-Up Junction Dimensions and (b) Impedance Input and Output of the Transmission Feedline

3.3.4 Simulation Results

Figure 3.4 shows the reflection coefficient (S_{11}) and bandwidth of single antennas. Figure 3.5 and 3.6 show the axial ratio and directivity of single antennas. Both single antenna elements show a good performance of S_{11} with approximately -12 dB at 28 GHz. Both single antenna elements exhibit 0.4 GHz bandwidth. Based on the axial ratio, it proves that the antennas are emitting linear polarization signals. The directivity of both single antenna elements illustrates high gain of main beam pattern by approximately 8 dBi.

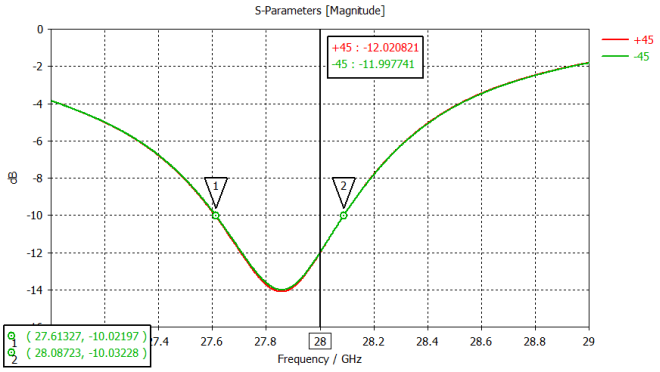

Figure 3.4 Reflection Coefficient (S_{11}) and Bandwidth of +45° and -45° Single Antenna Elements

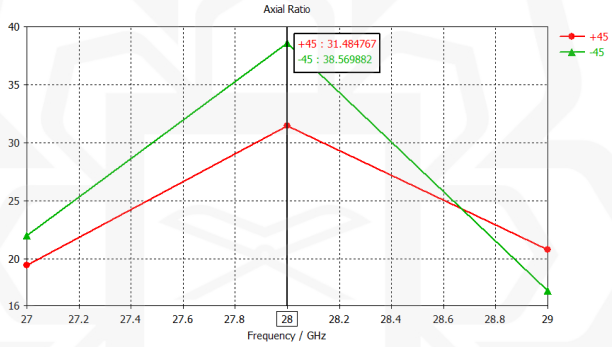

Figure 3.5 Axial Ratio of +45° and -45° Single Antenna Elements

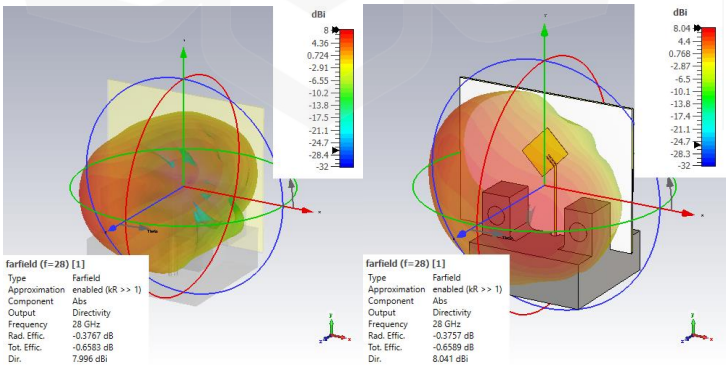

Figure 3.6 Directivity of +45° and -45° Single Antenna Elements

The realized gain of co-polarization elevation pattern of both single antennas is around 4.9 dBi. Meanwhile, the realized gain of co-polarization azimuth pattern is around 5 dBi and 3 dBi. The antenna gain is not high because it is just a single antenna, however, the radiated main beam signal is unidirectional and has a broader beamwidth. In order to determine a good antenna performance in delivering the transmitted signals into a location, usually the realized gain of co-polarization signals is set as the indicator. The co-polarization signals are the desired polarization which it maximizes signal strength and minimizes interference. On the other hand, the cross-polarization signals are unwanted polarization which it causes a reduction in signal strength and an increase in interference.

The comparison of realized gain co-polarization and cross-polarization of elevation and azimuth patterns of each +45° and -45° single antenna element is shown below in Figures 3.7 and 3.8. It shows that the levels of maximum beams of co-polarization signals are almost at the same level as the cross-polarization signals for both elevation and azimuth patterns.

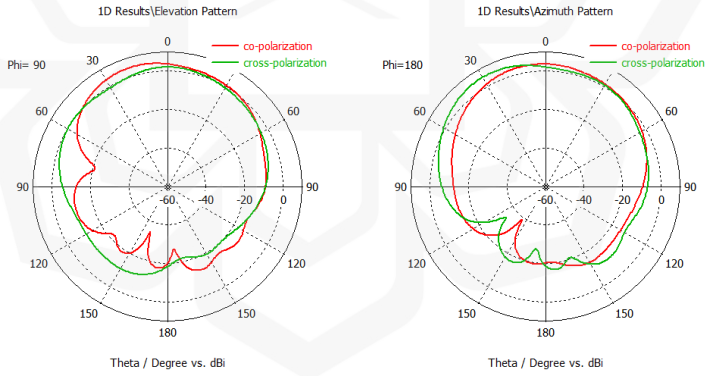

(a) (b)

Figure 3.7 The Comparison of the Realized Gain Co-Polarization and Cross-Polarization of (a) Elevation and (b) Azimuth Patterns of a +45° Single Antenna Element

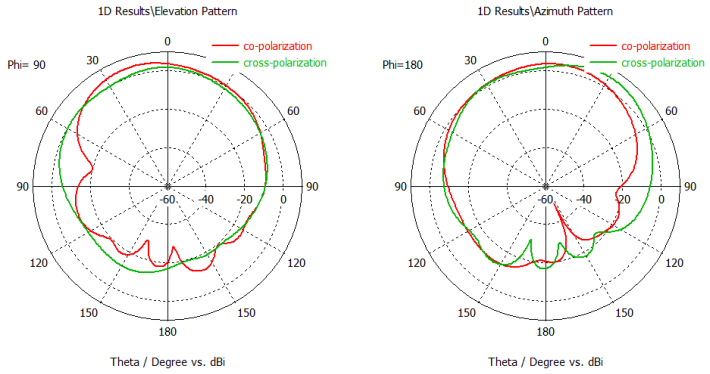

(a) (b)

Figure 3.8 The Comparison of the Realized Gain Co-Polarization and Cross-Polarization of (a) Elevation and (b) Azimuth Patterns of a -45° Single Antenna Element

Figure 3.9 shows the reflection coefficient (S_{11}) and bandwidth of the ±45° dual-polarised antenna. Figures 3.10 and 3.11 show the axial ratio and directivity of the ±45° dual-polarised antenna. The reflection coefficient of the dual-polarised antenna is satisfied by -10 dB, however there is a slight shifting of the resonant frequency to 27.6 GHz. This slight change in the resonant frequency might be due to possible factors such as the drilling of the SMA connector, or the insertion cable loss during the measurement. The bandwidth of the dual-polarised antenna is low with only 0.1 GHz. Based on the axial ratio, it proves that the antennas are emitting linear polarization signals. For the dual-polarised antenna, the directivity of the main beam reaches 7.9 dBi.

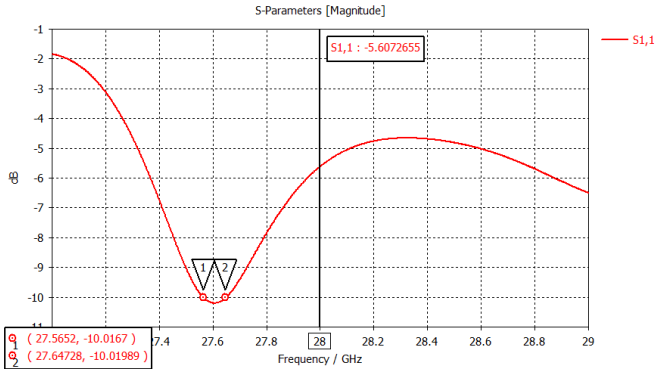

Figure 3.9 Reflection Coefficient (S_{11}) and Bandwidth of the ±45° Dual-Polarised Antenna

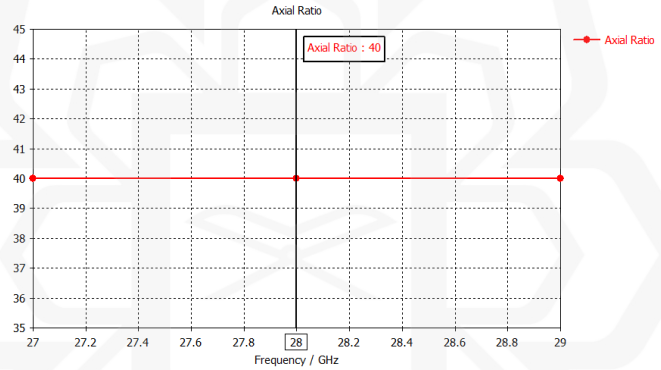

Figure 3.10 Axial Ratio of the ±45° Dual-Polarised Antenna

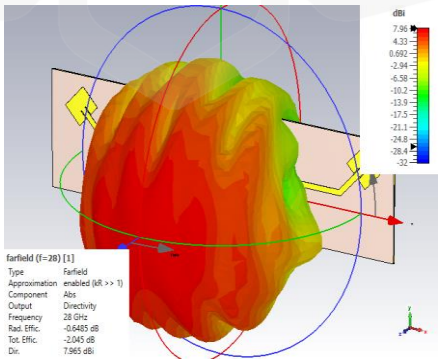

Figure 3.11 Directivity of the ±45° Dual-Polarised Antenna

For the dual-polarised antenna, the realized gain of co-polarization elevation and azimuth patterns show 5.91 dBi. Meanwhile, the realized gain of cross-polarization of both elevation and azimuth patterns is -77.2 dBi and 5.63 dBi, respectively. The comparison of realized gain co-polarization and cross-polarization of elevation and azimuth patterns of the ±45° dual-polarised antenna is shown below in Figure 3.12. It shows that the realized gain in co-polarization of elevation is much higher than the cross-polarization. However, the realized gain in co-polarization and cross-polarization of azimuth is almost identical to each other.

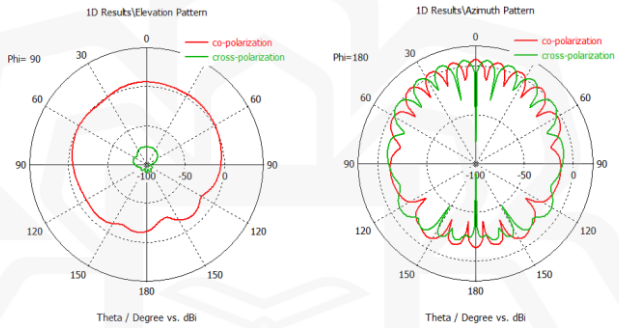

(a) (b)

Figure 3.12 The Comparison of Realized Gain Co-Polarization and Cross-Polarization of (a) Elevation and (b) Azimuth Patterns of the ±45° Dual-Polarised Antenna

3.4 DUAL LINEARLY POLARISED ANTENNA DESIGN 2 (SUBSTRATE THICKNESS OF 1.575 MM)

It was observed that the antenna design 1 (t=0.254 mm) is easily influenced by bending effects due to its thin substrate dimension. Therefore, the antenna performance at a substrate thickness of 1.575 mm is also designed and simulated.

3.4.1 Single Antennas Design

Adjustments were made to the length of the feeding transmission line (L_f), and the width and length of the substrate and ground plane (W_s, W_g, L_s, L_g) as shown in Table 3.3. The antenna patch elements dimensions and other dimensions are similar to antenna design 1 as shown in Table 3.1. Figure 3.13 displays the antenna design simulation using the CST Simulation tool. The T-power divider of antenna design 2 has similar dimensions to antenna design 1 except for the transmission length of the feedline, L7 as shown in Table 3.2. The modified T-power divider of the proposed dual-polarised antenna is explained in the next subsection. The patch elements dimensions are similar for both antenna design 1 and 2, due to the position of the patch elements on the substrate. The dimensions of the patch elements follow the rectangular patch formula from Equation (3.1) to Equation (3.7), and the position of the patch elements slanted to the normal plane on the antenna would cause the changes in the resonant frequency. Therefore, the effective length of the patch is 2.45 mm, and the maximum length is 3.93 mm (Equation 3.1-3.7). The length of the patch for a 1.575 mm antenna should be within this length to obtain optimal S_{11} performance. Due to the slanting position of the patch elements, the length has been adjusted in order to achieve the desired resonant frequency of 28 GHz. The aim is to evaluate their performance in terms of reflection coefficient, bandwidth, and radiation pattern.

Table 3.3 The Single Antenna Elements and Dual Linearly Polarised Antenna Dimensions at 28 GHz (Substrate Thickness = 1.575 mm)

Microstrip Patch Antenna / **Antenna Dimension**	**Single ±45° Patch Antenna**	**Dual-linearly Polarised Patch Antenna**	**A Dual-linearly Polarised Proposed Patch Antenna**
Width of substrate and ground, Ws and Wg (mm)	70.00	70.00	15.65
Length of substrate and ground, Ls and Lg (mm)	70.27	70.27	23.08
Length of feedline, Lf (mm)	39.14	40.25	17.00

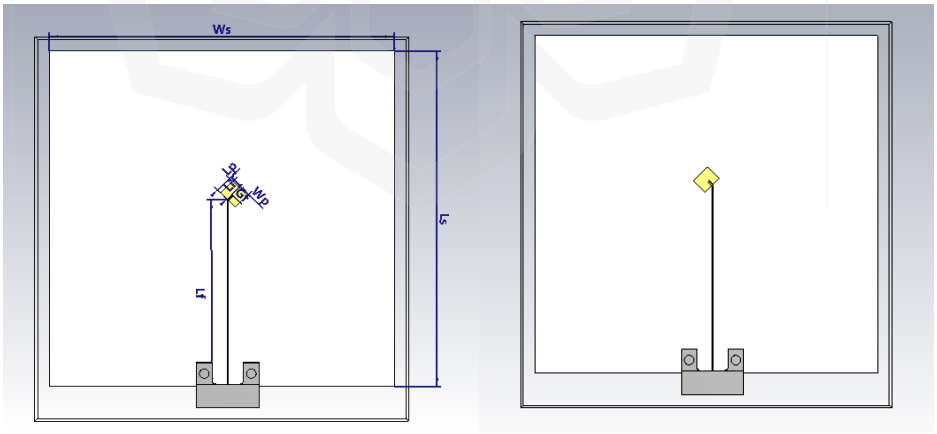

(a) (b)

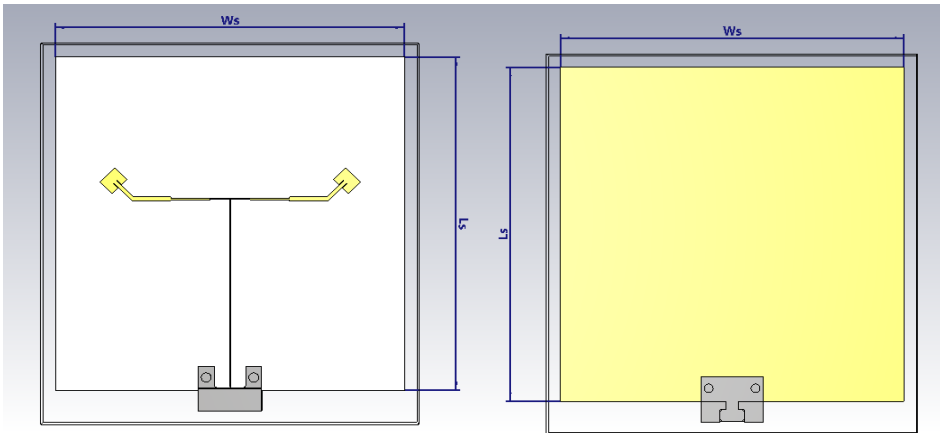

(c) (d)

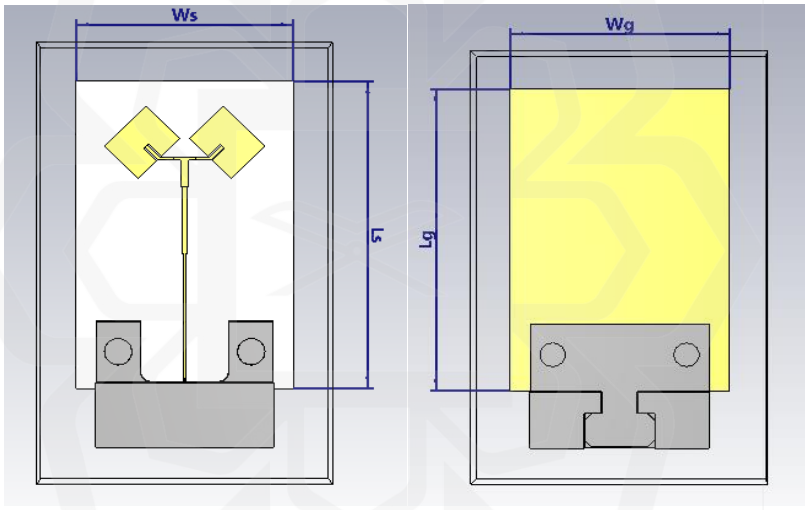

(e) (f)

Figure 3.13 The Antenna Design 2 Simulations of (a) the Front View of a Single +45° Antenna (b) the Front View of a Single -45° Antenna (c) the Front View of a ±45° Dual-Polarised Antenna (d) the Back View of a ±45° Dual-Polarised Antenna (e) the Front View of a Proposed Array Antenna and (f) the Back View of a Proposed Array Antenna

3.4.2 The Modification on T-Power Divider

The primary objective of this chapter is to investigate the dual-polarised antenna array's capability to direct its main beam towards a specific desired angle. Therefore, it is crucial to have a clearly visible directional main beam in order to observe steering angles. Therefore, the T-power divider is modified to reduce the spacing between elements of the antenna. Reducing the spacing between elements might decrease the sidelobe levels, resulting in a unidirectional main beam pattern. The modified T-power divider is designed using the CST Simulation tool as depicted in Figure 3.14 and Table 3.4 summarizes the modified T-power divider dimension value.

Table 3.4 Dimensions of the Modified T-Power Divider
(Substrate Thickness = 1.575 mm)

Parameters	**Dimension (mm)**
Microstrip Step width1 and length1 (MSW1, MSL1)	0.4 and 5.0
Microstrip Step width2 and length2 (MSW2, MSL2)	0.2 and 10.0
Microstrip T junction width1 and length1 (MJW1, MJL1)	0.2 and 0.5
Microstrip T junction width2 and length2 (MJW2, MJL2)	0.2 and 0.5
Microstrip T junction width3 and length3 (MJW3, MJL3)	0.6 and 2.0
Microstrip bend optimal mitered1 width, length1, length2, and angle (MB1W, MB1L1, MB1L2, MB1A)	0.2, 1.0, 1.25, and 45°
Microstrip bend optimal mitered2 width, length1, length2, and angle (MB2W, MB2L1, MB2L2, MB2A)	0.2, 1.25, 1.0, and 45°

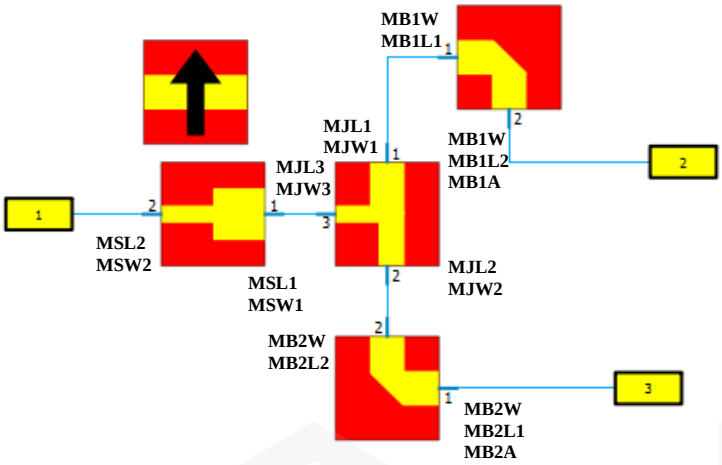

(a)

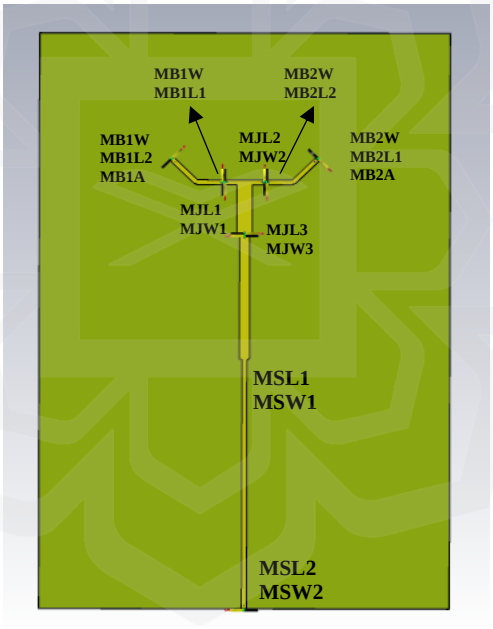

(b)

Figure 3.14 (a) The Schematic Diagram and (b) 3D Assembly of the Modified T-Power Divider

3.4.3 Simulation Results

Figure 3.15 shows the reflection coefficient (S_{11}) and bandwidth of single antennas. Figures 3.16 and 3.17 show the axial ratio and directivity of single antennas. The S_{11} of single antennas is approximately -15 dB. The achieved bandwidth of the single antennas is relatively low due to the patch antenna characteristic with only 0.2 GHz. The axial ratio values shown indicate that the polarization of the antenna is linear. The directivity for respective antennas approximately 8 dBi for single antennas.

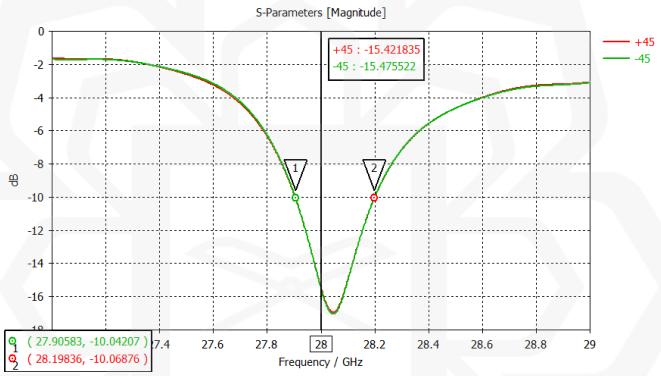

Figure 3.15 Reflection Coefficient (S_{11}) and Bandwidth of +45° and -45° Single Antenna

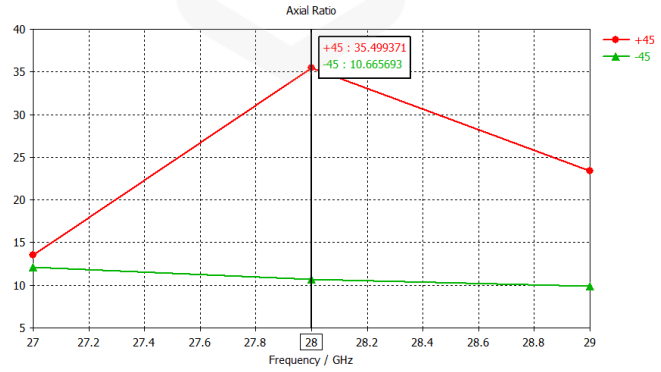

Figure 3.16 Axial Ratio of +45° and -45° Single Antenna Elements

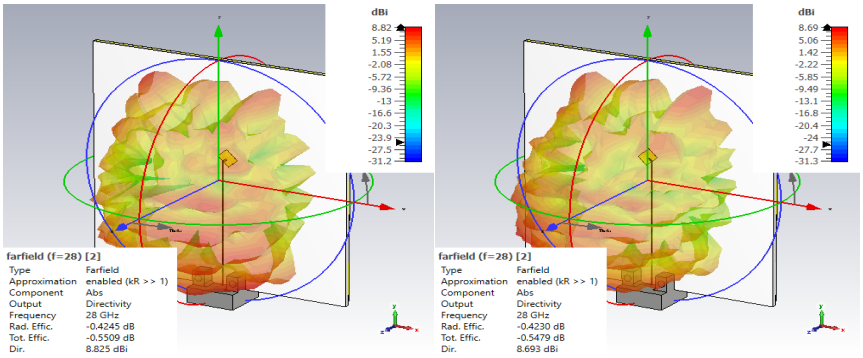

Figure 3.17 Directivity of +45° and -45° Single Antenna Elements

The realized gain of co-polarization elevation pattern of both single antennas is around 5 dBi. Meanwhile, the realized gain of co-polarization azimuth pattern is around 3 dBi and 3.8 dBi. The radiation pattern looks like a fan-shaped pattern. The comparison of realized gain of co-polarization and cross-polarization of elevation and azimuth patterns of each +45° and -45° single antenna element is shown below in Figure 3.18 and Figure 3.19. It shows that the level of maximum beams of co-polarization signals is almost at the same level as the cross-polarization signals for both elevation and azimuth patterns.

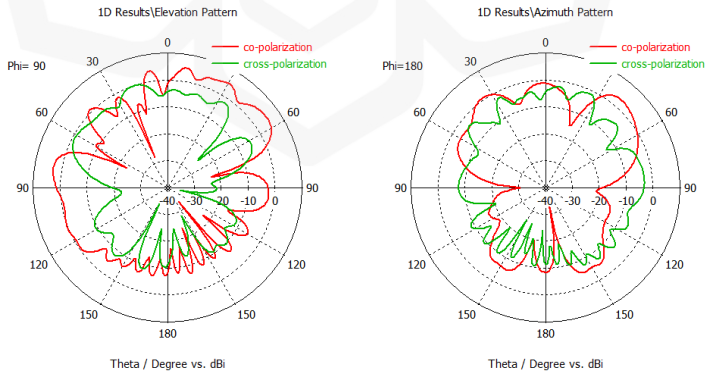

(a) (b)

Figure 3.18 The Comparison of Realized Gain Co-Polarization and Cross-Polarization of (a) Elevation and (b) Azimuth Patterns of a +45° Single Antenna Element

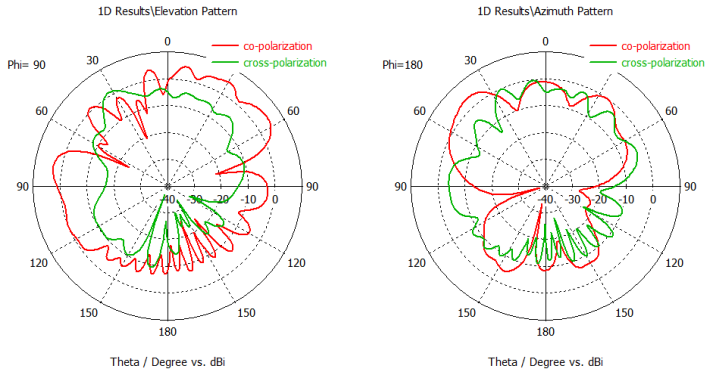

(a) (b)

Figure 3.19 The Comparison of Realized Gain Co-Polarization and Cross-Polarization of (a) Elevation and (b) Azimuth Patterns of a -45° Single Antenna Element

Figure 3.20 shows the reflection coefficient (S_{11}) and bandwidth of the ±45° dual-polarised antenna and ±45° proposed dual-polarised antenna. Figures 3.21 and 3.22 show the axial ratio and directivity of both antennas.

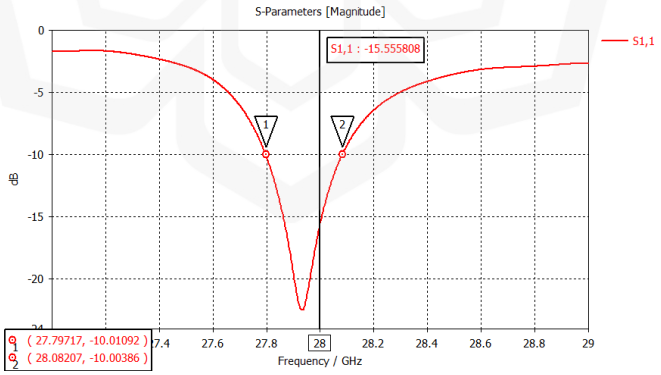

(a)

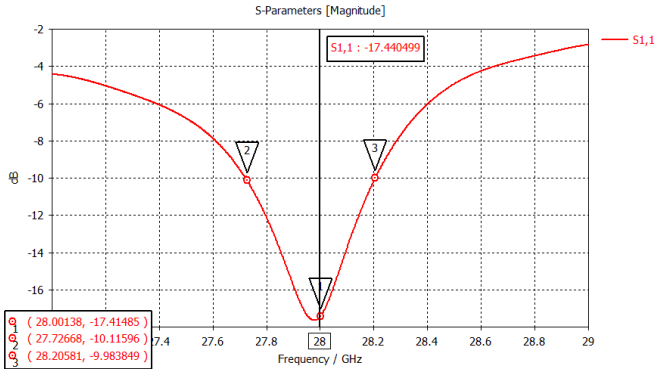

(b)

Figure 3.20 Reflection Coefficient (S_{11}) and Bandwidth of (a) the ±45° Dual-Polarised Antenna and (b) the ±45° Proposed Dual-Polarised Antenna

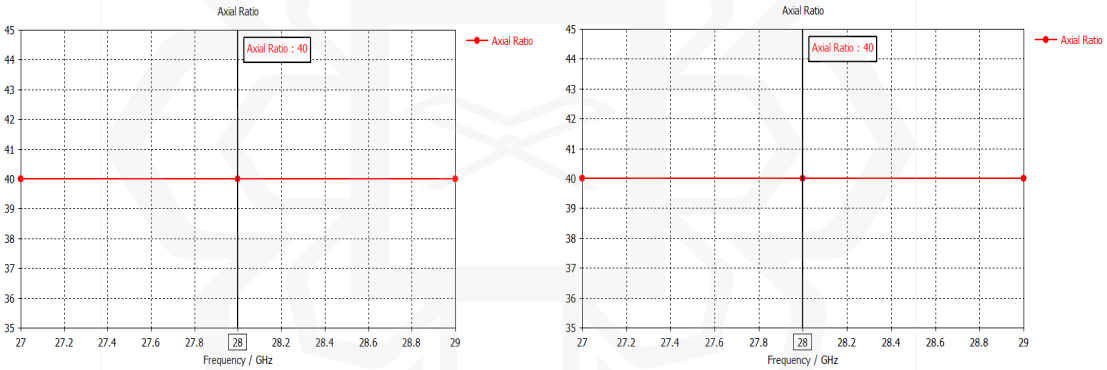

(a) (b)

Figure 3.21 Axial Ratio of (a) the ±45° Dual-Polarised Antenna and (b) the ±45° Proposed Dual-Polarised Antenna

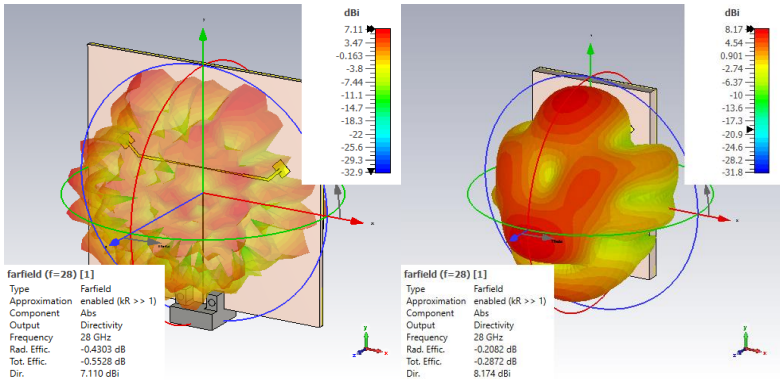

(a) (b)

Figure 3.22 Directivity of (a) the ±45° Dual-Polarised Antenna and (b) the ±45° Proposed Dual-Polarised Antenna

The comparison of realized gain in co-polarization and cross-polarization of elevation and azimuth patterns of both antennas is shown below in Figure 3.23. It shows that the realized gain of co-polarization in the elevation pattern is much higher than in cross-polarization. However, the realized gain in the azimuth pattern is almost identical for both co-polarization and cross-polarization signals.

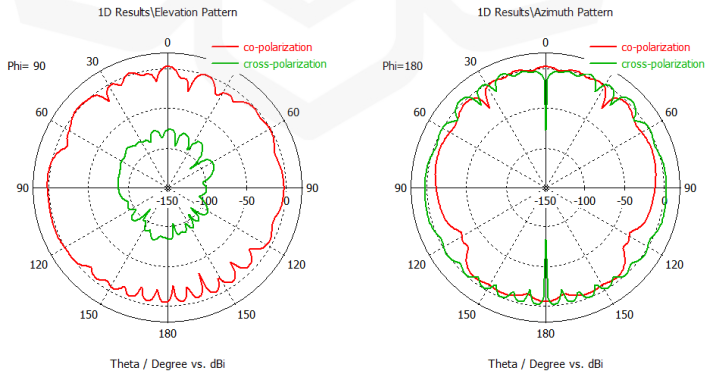

(a) (b)

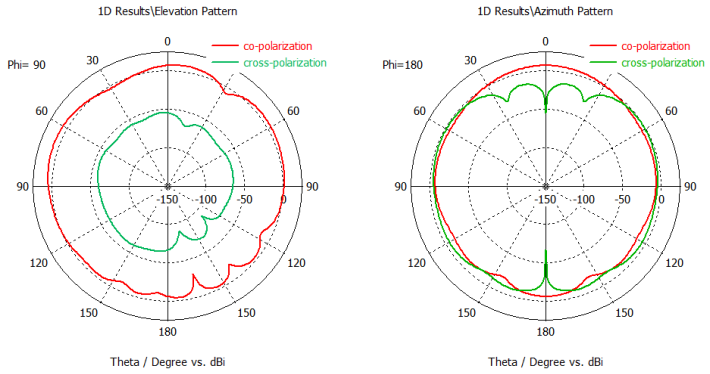

(c) (d)

Figure 3.23 The Comparison of Realized Gain Co-Polarization and Cross-Polarization of (a) Elevation and (b) Azimuth Patterns of the ±45° Dual Linearly Polarised Antenna (c) Elevation and (b) Azimuth Patterns of the ±45° Proposed Dual Linearly Polarised Antenna

A modification was made to the T-power divider by reducing the length between the two output ports to improve the main beam pattern. The overall dimension of the T-power divider is also changed into a smaller size. Figure 3.24 shows the reflection coefficient (S_{11}) performance of the modified T-power divider.

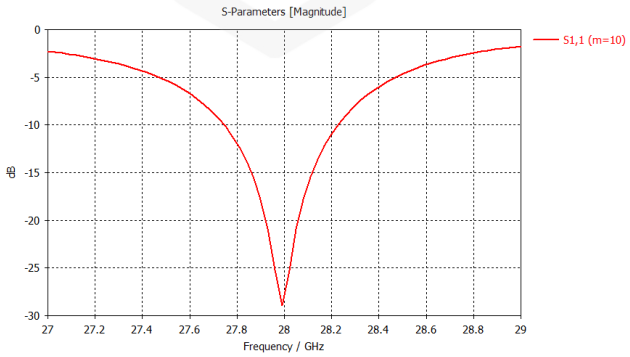

Figure 3.24 The Reflection Coefficient (S_{11}) of the Modified T-Power Divider

From the figure above, it shows that the S_{11} resonates at 28 GHz is -29 dB. It shows that the improvement made to the T-power divider gives a better S_{11} performance. The modified T-power divider is attached to each radiating element and then configured it to linear array arrangement of 1 x 4.

3.5 DUAL-LINEARLY POLARISED ANTENNA ARRAYS DESIGN

For the antenna array configuration, it consists of 8 antenna elements with four T-power dividers, and four feed ports. Port one to port four are the feeding ports to excite both +45° and -45° polarizations of antenna elements simultaneously. Each feed port is connected to an equal power divider and two radiating patch elements. The antenna elements are simultaneously excited with the same amplitude and phase by tuning the amplitude to '1' and phase input to '0°' to obtain its radiation pattern.

3.5.1 Design 1 (Substrate Thickness of 0.254 mm)

Based on the single antenna of design 1 (substrate thickness 0.254 mm), a 1 x 4 ±45° dual-polarised antenna array is designed to improve the antenna's performance. The inter-element spacing is 56.71 mm (7.85 λ). The overall dimensions of the antenna array are 226.84 x 15.92 x 0.254 mm^3. Ws and Wg represent the width of the substrate and ground plane, while Ls and Lg represent the length of the substrate and ground plane. Figure 3.25 depicts the simulation of antenna array design 1.

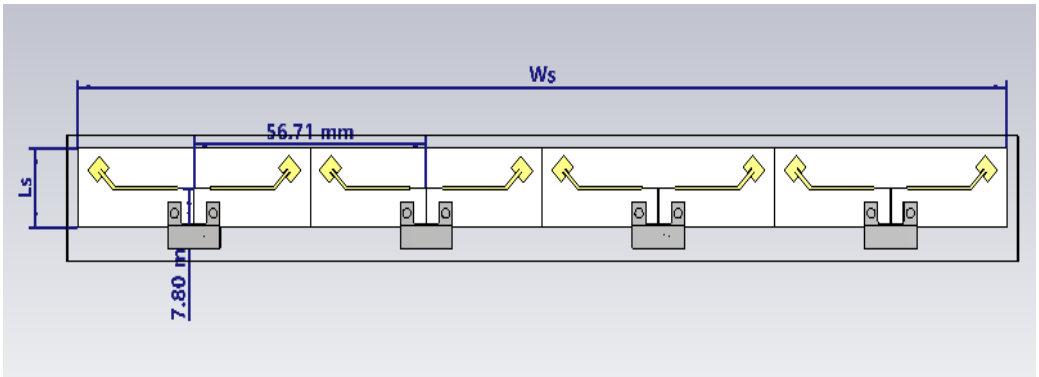

(a)

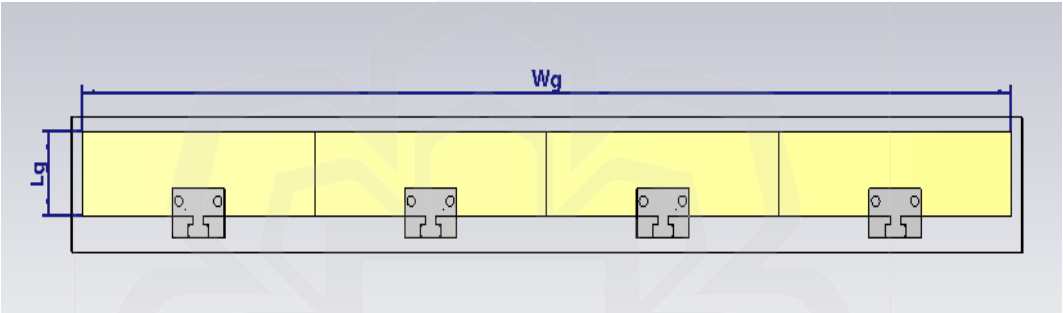

(b)

Figure 3.25 The Antenna Array Design 1 Simulation of (a) the Front View and (b) the Back View

3.5.2 Design 2 (Substrate Thickness of 1.575 mm)

Based on the single antenna of design 2 (substrate thickness 1.575 mm), a 1 x 4 ±45° dual-polarised antenna array is designed to improve the antenna's performance. The inter-element spacing is 70 mm (9.69 λ). The overall dimensions of the antenna array are 280 x 70.27 x 1.575 mm^3. Ws and Wg represent the widths of the substrate and ground plane, while Ls and Lg represent the lengths of the substrate and ground plane. Figure 3.26 depicts the simulation of the antenna array design 2.

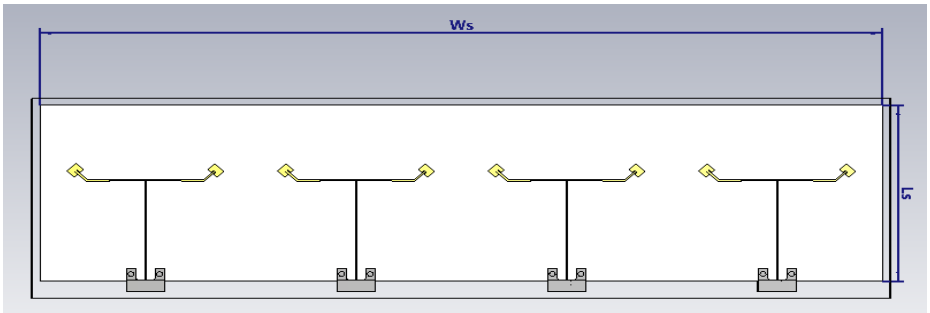

(a)

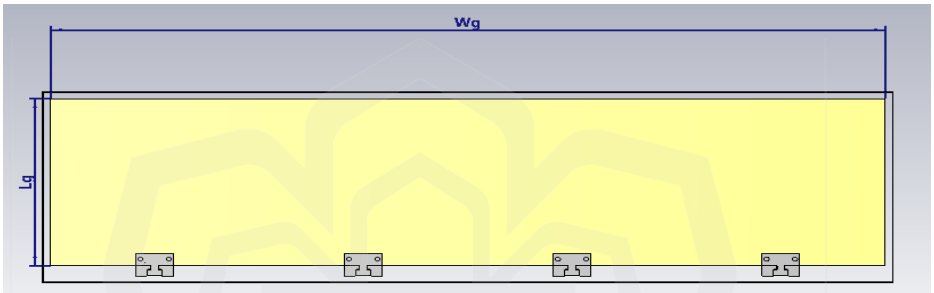

(b)

Figure 3.26 The Antenna Array Design 2 Simulation of (a) the Front View and (b) the Back View

3.5.3 Proposed Antenna Array Design

The proposed dual-polarised antenna array with substrate thickness of 1.575 mm is designed using the same patch dimensions and connected to a modified T-power divider. The antenna's radiating patch elements are configured similarly to the previous antenna array design 2 except that the inter-element spacing is reduced to 15.60 mm (2.159 λ). The overall dimensions of the antenna array are 62.45 x 23.08 x 0.254 mm^3. Figure 3.27 shows the front and back views of the proposed dual-polarised antenna array design simulation.

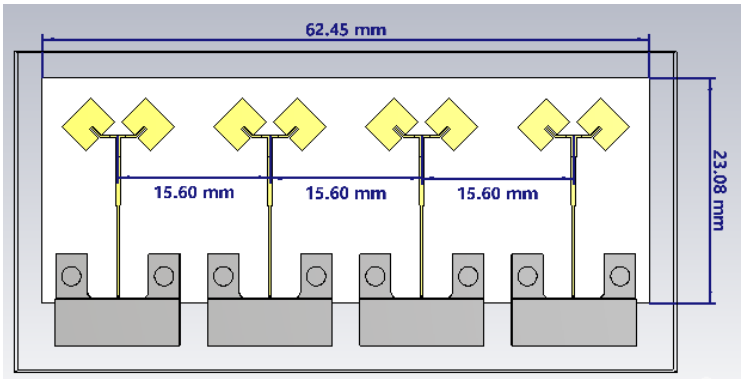

(a)

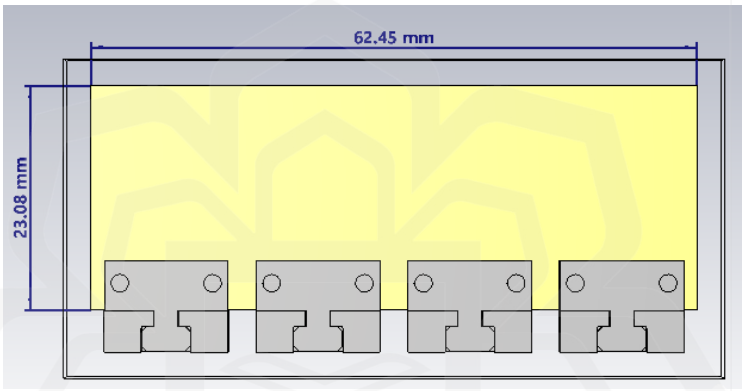

(b)

Figure 3.27 The Proposed Antenna Array Design Simulation of (a) the Front View and (b) the Back View

3.5.4 Simulation Results

Legend 'AD1' indicates the antenna array design 1, legend 'AD2' indicates the antenna array design 2, and legend 'IMPROVED' indicates the proposed antenna array. Figure 3.28 shows the reflection coefficient of each port (S_{11}), (S_{22}), (S_{33}), (S_{44}), and bandwidth of the ±45° antenna arrays. The reflection coefficient of each port for antenna array design 1 is -5.6 dB, antenna array design 2 is -11.9 dB and -12.8 dB, and for the proposed antenna array

is -13.3 dB and -13.6 dB, respectively. The reflection coefficient is better on the proposed antenna array. A slight change in resonant frequency is also observed. The bandwidth of each port for antenna array design 1 is close to 0 GHz, for antenna array design 2 is 0.28 GHz and 0.29 GHz, and for the proposed antenna array is 0.51 GHz. The bandwidth is better on the proposed antenna array.

Figure 3.29 shows the mutual coupling between port 1 and 2, port 1 and 3, and port 1 and 4, for respective antenna array. The inter-element spacing is uniform therefore, mutual coupling between each port is approximately the same. All antenna arrays show a good performance of mutual coupling which is less than -20 dB. Figure 3.30 shows the axial ratio of the antenna arrays. The axial ratio of the antenna arrays shows 40 and 20 indicating that the antenna arrays are linearly polarised. The improved design introduces intentional or unintentional phase difference or imbalance between the ±45° elements due to adjusted L7 line lengths. These changes could affect the relative amplitude and phase of the orthogonal field components, reducing the polarization linearity and thereby lowering the axial ratio. However, 40 and 20 value of axial ratio remains a desirable axial ratio indicates that the radiated field is confined to a linear polarization state. Figure 3.31 shows the directivity of the antenna arrays. The directivity of antenna array design 1, design 2, and the proposed antenna array is 14.01 dBi, 11.80 dBi, and 14.89 dBi. The proposed antenna array has better directivity performance.

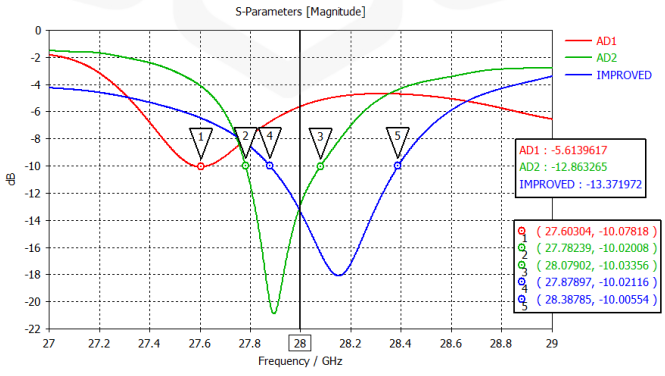

(a)

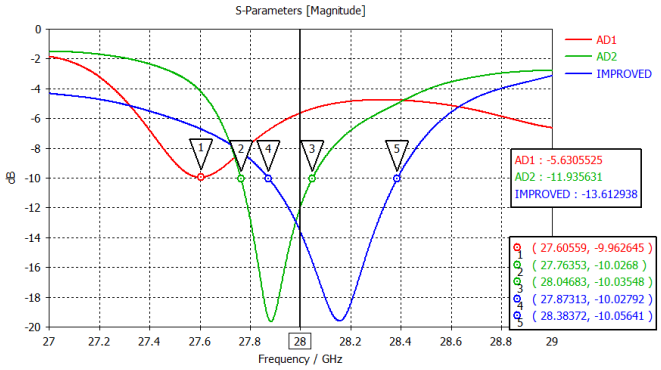

(b)

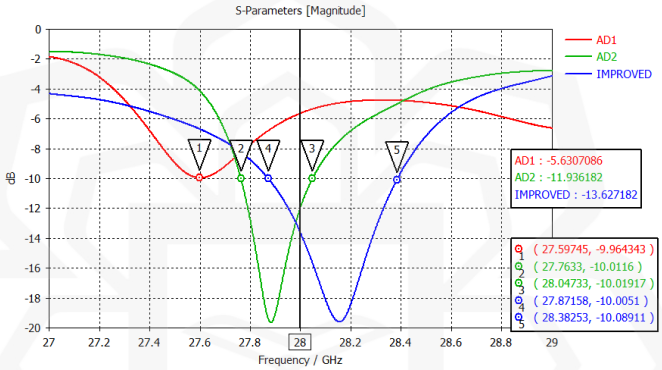

(c)

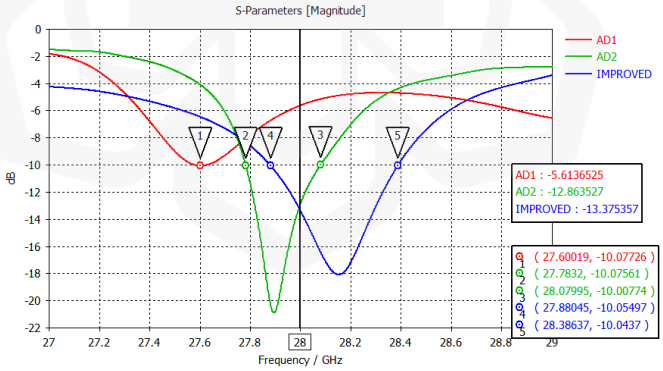

(d)

Figure 3.28 The Reflection Coefficient and Bandwidth of (a) (S_{11}) (b) (S_{22}) (c) (S_{33}) and (d) (S_{44}) of the Antenna Arrays

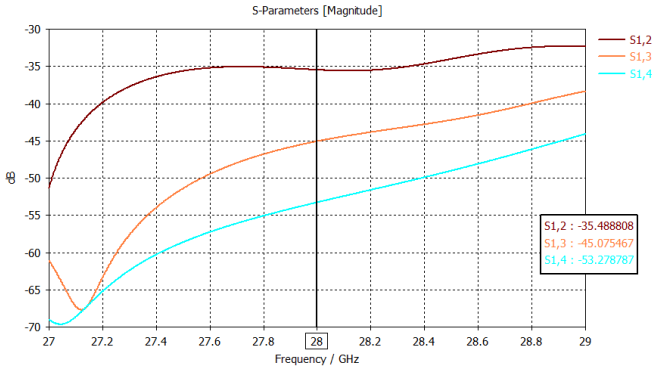

(a)

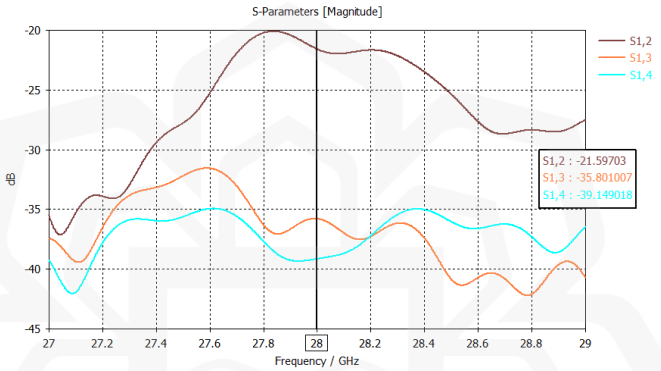

(b)

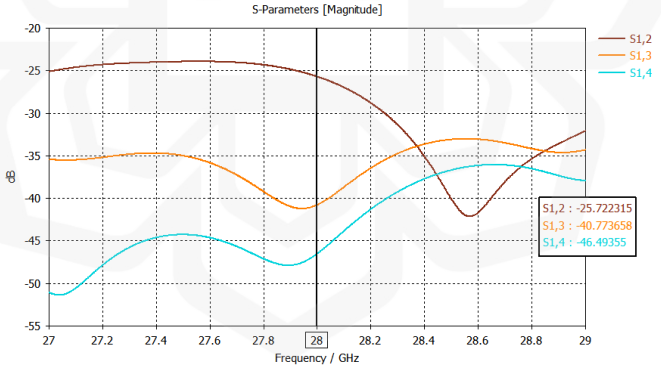

(c)

Figure 3.29 Mutual Coupling (S_{12}, S_{13}, S_{14}) of the (a) Antenna Array Design 1 (b) Design 2 and (c) Proposed Antenna Array

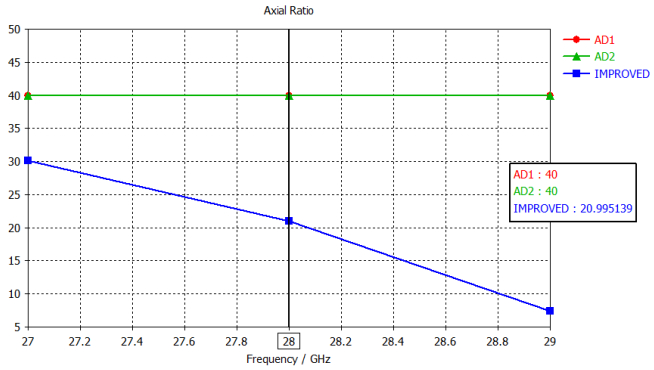

Figure 3.30 Axial Ratio of the Antenna Arrays

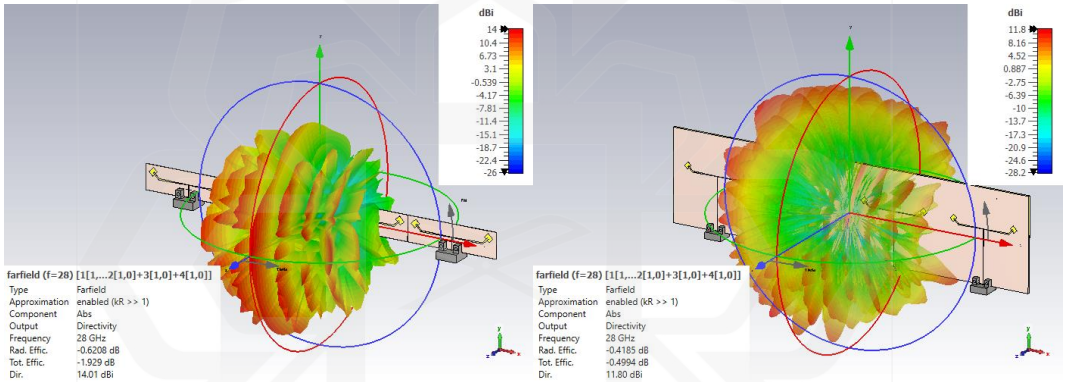

(a) (b)

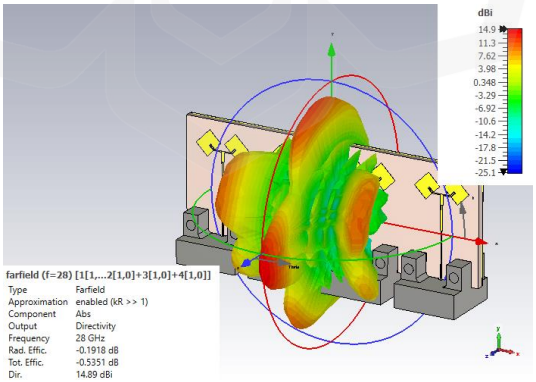

(c)

Figure 3.31 Directivity of the Antenna Array (a) Design 1 (b) Design 2 and (c) Proposed Antenna Array

From the antenna design 1 using substrate thickness of 0.254 mm, it shows that the antenna array exhibits a more directional main beam pattern than the other antennas. The antenna array's realized gain is much higher with a value of 12 dBi or 9.85 dB than the other antennas. The peak realized gain of co-polarization signals for both elevation and azimuth patterns is 12 dBi. Meanwhile, the peak realized gain of cross-polarization signals for elevation and azimuth patterns is -71.7 dBi and 9.39 dBi.

From the antenna design 2 using substrate thickness of 1.575 mm, it shows that the antenna array exhibits a more directional main beam pattern than the other antennas. The antenna array's realized gain is much higher with values of 8.5 dBi or 6.35 dB and 6.64 dBi or 4.49 dB, respectively. For the antenna array design 2, the peak realized gain of co-polarization signals for both elevation and azimuth patterns is 8.50 dBi and 6.64 dBi. Meanwhile, the peak realized gain of cross-polarization signals for elevation and azimuth patterns is -72.7 dBi and 5.37 dBi.

It is crucial to have a directive main beam pattern of co-polarization azimuth pattern as the phase distribution to the feeding ports would cause the main beam to be steered into a desired location (theta angle), and it could be observed from the azimuth plane. The amplitude of the all-source excitations is fixed to 1. Therefore, the modification of the T-power divider has been made to improve the directive main beam pattern. A reduction in the elements spacing would improve the directivity of the antenna array, hence improving its main beam pattern. The modified T-power divider is attached to each dual-polarised antenna element in a 1 x 4 linear array configuration. A proposed dual-polarised antenna array is then further designed and simulated to observe its performance particularly at the co-polarization azimuth pattern for beam-steering capability. For the proposed antenna array, the peak realized gain of co-polarization signals for both elevation and azimuth is 14.4 dBi and 13.1 dBi. Meanwhile, the peak realized gain of cross-polarization signals for elevation and azimuth is -54 dBi and 5.02 dBi.

The comparison of realized gain in co-polarization and cross-polarization in the elevation and azimuth patterns of the dual-polarised antenna array designs 1, 2, and a proposed antenna array is shown in Figure 3.32 (a) to Figure 3.32 (c). The polar pattern has been scaled to the same value. The realized gain of co-polarization in the elevation pattern

is much higher than that of cross-polarization. Meanwhile, the realized gain of co-polarization and cross-polarization in the azimuth pattern is at almost the same level. Based on the azimuth pattern (*xz*-plane), the orientations of the field components are parallel to the y and x axes if the radiating element is not slanted. When these two vectors are decomposed to ±45° orientations, the levels of co-polarization and cross-polarization are equal. This is also explained in the same situation for dual-polarised antenna designs 1 and 2 in the previous section (Lv et al., 2021).

The shape of the realized gain in the elevation pattern for all antenna arrays is not omni-directional. This is because the scale of the realized gain in all patterns has been standardized. All antenna array patterns show a fan-shaped beam pattern except for the realized gain of the elevation pattern of antenna array design 1 (Figure 3.32(a) (left)). The beam pattern that shows a unidirectional main beam is seen in the realized gain of co-polarization azimuth pattern of the proposed antenna array (Figure 3.32(c)(right)).

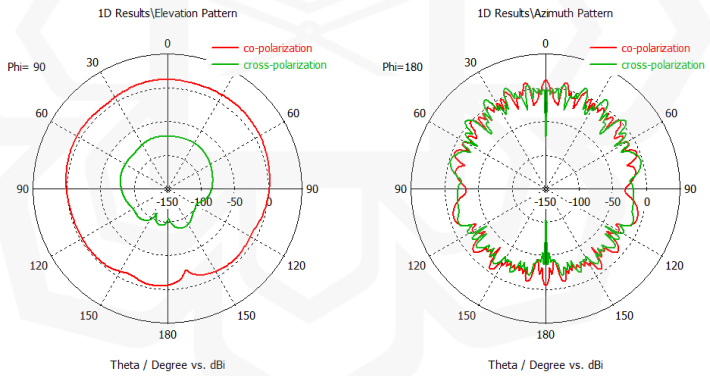

(a)

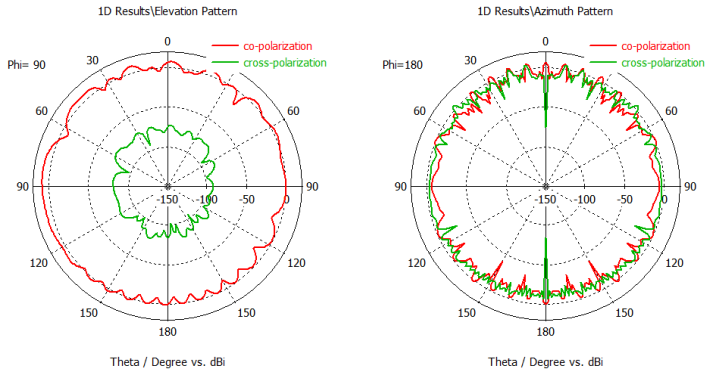

(b)

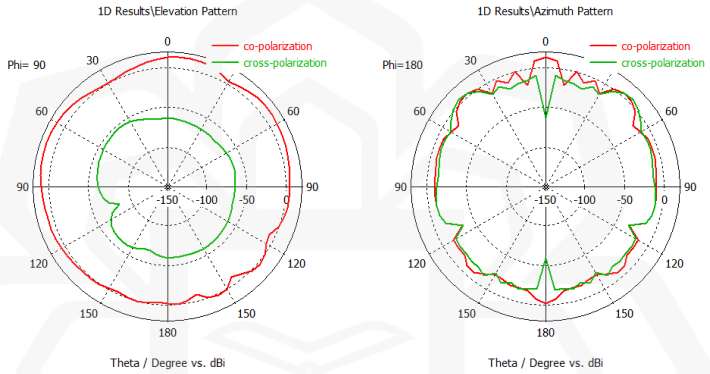

(c)

Figure 3.32 The Comparison of Realized Gain Co-Polarization and Cross-Polarization of Elevation (Left) and Azimuth (Right) Patterns of the Dual-Polarised Antenna Arrays (a) Design 1 (b) Design 2 and (c) the Proposed Antenna Array

Table 3.5, 3.6, and 3.7 show the summary of simulation results for all substrates. Table 3.5 presents a comparison of the simulated performance for three antenna types using a 0.254 mm substrate. All designs achieved acceptable impedance matching with S_{11} values below –10 dB, though the dual-polarised antenna exhibited a slightly narrower impedance bandwidth of 0.085 GHz compared to the single-polarised designs which around 0.47–0.48 GHz. In terms of axial ratio, all antennas showed values above 30, confirming strongly linear polarization, with the dual-polarised antenna achieving the highest axial ratio at 40.

Directivity was consistent across all types approximately at ~8 dBi, but the dual-polarised design offered the highest co-polarised realized gain in both elevation and azimuth planes around 5.91 dBi, alongside an exceptionally low elevation cross-polarization gain around –77.2 dBi, indicating excellent polarization purity. These results highlight the dual-polarised antenna's superior radiation characteristics despite its reduced bandwidth.

Table 3.5 The Simulation Results of Antennas (Substrate Thickness of 0.254 mm)

Microstrip Patch Antenna / **Outputs**	**Single +45° Patch Antenna**	**Single -45° Patch Antenna**	**±45° Dual-linearly Polarised Patch Antenna**
Reflection Coefficient (dB)	-12.00	-12.00	-10.00
Impedance Bandwidth (GHz)	0.47	0.47	0.08
Axial Ratio	31	39	40
Directivity (dBi)	7.99	8.04	7.96
Realized gain of co-polarization elevation (dBi)	4.94	4.98	5.91
Realized gain of co-polarization azimuth (dBi)	5.68	3.81	5.91

Realized gain of cross-polarization elevation (dBi)	2.07	1.90	-77.20
Realized gain of cross-polarization azimuth (dBi)	5.68	5.85	5.63

Table 3.6 presents the simulation results of antennas with a substrate thickness of 1.575 mm, showing that the proposed ±45° dual-linearly polarised patch antenna achieved the best performance in terms of reflection coefficient of –17.41 dB and co-polarised realized gain, with values reaching 7.98 dBi in elevation and 7.13 dBi in azimuth, significantly higher than the other antenna configurations. While the single +45° and –45° antennas showed good S_{11} values around –15.5 dB and moderate gains, the ±45° dual-polarised antenna suffered from a lower co-polarised gain at 2.84 dBi due to degraded coupling or mismatch effects. In terms of axial ratio, both dual-polarised antennas retained values near 40, indicating strong linear polarization, whereas the single –45° antenna showed a drop to 10.7. Cross-polarization performance was best in the proposed antenna, with elevation cross-polar gain at –54.10 dBi, further confirming its superior polarization purity. Overall, the proposed dual-polarised design demonstrated optimized performance by combining high gain, excellent impedance matching, and reduced unwanted polarization components.

Table 3.6 The Simulation Results of Antennas (Substrate Thickness of 1.575 mm)

Microstrip Patch Antenna / **Outputs**	**Single +45° Patch Antenna**	**Single -45° Patch Antenna**	**±45° Dual-linearly Polarised Patch Antenna**	**Proposed ±45° Dual-linearly Polarised Patch Antenna**
Reflection Coefficient (dB)	-15.60	-15.50	-15.50	-17.41
Impedance Bandwidth (GHz)	0.29	0.20	0.29	0.47
Axial Ratio	35.50	10.70	40.00	40.00
Directivity (dBi)	8.82	8.69	7.11	8.17
Realized gain of co-polarization elevation (dBi)	4.99	4.98	2.84	7.98
Realized gain of co-polarization azimuth (dBi)	2.98	3.81	2.84	7.13
Realized gain of cross-polarization elevation (dBi)	-0.12	1.12	-76.00	-54.10
Realized gain of cross-polarization azimuth (dBi)	-1.48	-0.35	3.96	-1.12

Table 3.7 presents a performance comparison among three dual-linearly polarised antenna arrays at 28 GHz using different substrate thicknesses and design modifications. The proposed antenna array, with 1.575 mm substrate and reduced element spacing, demonstrates the best overall performance, achieving the highest directivity of 14.89 dBi, realized co-polarised gain in both elevation, 14.4 dBi, and azimuth, 13.1 dBi, and the widest bandwidth of 0.463 GHz, outperforming the original arrays. While the array with 1.575 mm substrate shows excellent impedance matching with S_{11} is –17.47 dB, its gains are significantly lower, 8.50 dBi elevation, 6.64 dBi azimuth. The 0.254 mm array exhibits lower gain and narrow bandwidth of 0.124 GHz due to substrate limitations. The axial ratio of the proposed design is 21 and is lower than the others which is 40, suggesting a slight deviation from perfect linear polarization but still within acceptable range. Overall, the proposed antenna array offers a well-balanced trade-off between gain, bandwidth, and polarization, making it more suitable for high-performance 5G beam-steering applications.

Table 3.7 The Simulation Results of the Antenna Arrays at 28 GHz

Microstrip Patch Antenna / **Outputs**	**Dual-linearly Polarised Antenna Array (t=0.254 mm)**	**Dual-linearly Polarised Antenna Array (t=1.575 mm)**	**A Proposed Dual-linearly Polarised Antenna Array (t=1.575 mm)**
Reflection Coefficient (dB)	-10.00	-17.47	-12.00
Impedance Bandwidth (GHz)	0.12	0.32	0.46
Axial Ratio	40.00	40.00	21.00

Directivity (dBi)	14.01	10.77	14.89
Realized gain of co-polarization elevation (dBi)	12.10	8.50	14.40
Realized gain of co-polarization azimuth (dBi)	12.00	6.64	13.10
Realized gain of cross-polarization elevation (dBi)	-71.70	-72.70	-54.00
Realized gain of cross-polarization azimuth (dBi)	9.39	5.37	5.02

As mentioned before, the aim of this study is to steer the main beam into a desired location. Having a directional main beam pattern is important to observe the changes in steering the angle direction (azimuth angle) of the main beam. Angle direction indicates our desired location of targeting transmitted signals. In addition to that, the changes in beam-steering are influenced by the phase input signals and do not correlate to the amplitude. Therefore, the proposed antenna array shows a directional main beam pattern at the co-polarization azimuth pattern and it would be used for implementation of DNN algorithm for beam-steering capability in Chapter four. The simulation antenna performance plays a crucial role before progressing to the fabrication stage. Once satisfactory simulation outcomes are achieved, it is important to verify these simulation results through measurements. The process of measuring antennas and verification of DNN algorithm would be explained in Chapter five.

3.6 SUMMARY OF CHAPTER

Chapter 3 presents the detailed design and simulation of the proposed ±45° dual-linearly polarised antenna array intended for 28 GHz 5G beam-steering applications. The design begins with the development of single +45° and –45° slanted patch antennas, followed by the integration into a dual-polarised configuration using a T-power divider for signal distribution. Two substrate thicknesses (0.254 mm and 1.575 mm) are evaluated to examine their effects on key performance parameters such as reflection coefficient (S_{11}), bandwidth, gain, directivity, axial ratio, and polarization purity. The simulation results reveal that while both single-polarised antennas provide good impedance matching and linear polarization, the dual-polarised array with a thicker substrate achieves higher co-polarised gain and lower elevation cross-polarization. An improved version of the dual-polarised array is proposed by optimizing the substrate thickness and reducing element spacing, leading to significantly better performance in terms of gain (up to 14.4 dBi), bandwidth (0.463 GHz), and acceptable axial ratio (21). Overall, the chapter demonstrates that the proposed array design offers a balanced and high-performance solution for millimeter-wave 5G antenna systems, validating its suitability for integration with beam-steering techniques in next chapters.

CHAPTER FOUR

DEEP NEURAL NETWORK FOR BEAM-STEERING CAPABILITIES

4.1 INTRODUCTION

Deep learning combines feature collection and regression or classification with a larger number of neurons, simultaneously processes data through different layers, naturally extracts features, and assesses network hyperparameters, constructing a useful learning model from input data.

The pattern synthesis of the proposed DLPAA involves weight coefficients of the array to steer the main beam into a desired location, given the fixed amplitude of 1 and phase variation. These phase variations are indicators of the desired steered-beam location. Unlike the conventional methods of using mechanical parts to change the phase distribution of the antenna array, this study uses DNN model to act as the medium to obtain the predicted phase value for the proposed DLPAA. All the numerical computation and programming are carried out by MATLAB computing languages.

MATLAB serves as both a numerical computing environment and a programming language. It enables simple manipulation of matrices, plotting of functions and data, execution of algorithms, developing user interfaces, and connecting with programs in different languages. The MATLAB tools in the Neural Network Toolbox enable the designing, implementing, visualizing, and simulating of neural networks. It also offers extensive assistance for various established network paradigms, along with user-friendly graphical user interfaces (GUIs) for easy design and management of neural networks. The study utilizes MATLAB (R2024a) to create script files for building MLP and DNN models as well as functions for evaluating model performance by calculating error statistics like root-mean-square-error (RMSE) and loss.

In this study, the active element pattern (AEP) of the proposed DLPAA is presented to calculate the radiation pattern, also known as pattern synthesis, and to verify the predicted phase outputs from the DNN algorithm corresponding to the second objective of this study. The AEP is obtained by exciting a single element while the other elements are terminated with matched loads. The total far-field is given by the summation of AEP of all the port elements. The test datasets of initial phase value are obtained by placing the value obtained from Equation 4.4.

This chapter explains the DNN architecture, array pattern structure, data collection, data preprocessing, verification of AEP-based method, modeling network, training and validating network, testing network, DNN programming code, and summary. The aim of this chapter is to prove the ability of the DNN algorithm to steer the main beam into a desired location (degree), which is the second objective of this study. The verification of simulated DNN results is done by measured data in Chapter 5.

4.2 AEP-DNN DEVELOPMENT FLOWCHART

Figure 4.1 depicts the flowchart procedure for executing the DNN model. All details of each block in Figure 4.1 would be explained in each section. The development process begins by constructing the Deep Neural Network (DNN) architecture and selecting a suitable implementation framework. Following this, data relevant to the beam-steering application is collected and undergoes preprocessing, which includes normalization and formatting to ensure compatibility with the network input.

The network is then modelled and trained using the prepared dataset, with validation performed concurrently to monitor performance and minimize overfitting. After training, the proposed Active Element Pattern (AEP) approach is verified to assess its initial accuracy and reliability. If the verification fails to meet expected performance, the process is iterated with necessary adjustments. Upon successful verification, the trained model is

tested using unseen data to evaluate its generalization ability. The test results are analysed to determine whether the predicted output meets the targeted angular estimation criteria. If not, the training and modelling process is repeated. Finally, once the model achieves the desired accuracy, it is compared with conventional approaches such as the Full Wave Modelling (FWM) and Pattern Multiplication Method (PMM) to benchmark the performance of the proposed method.

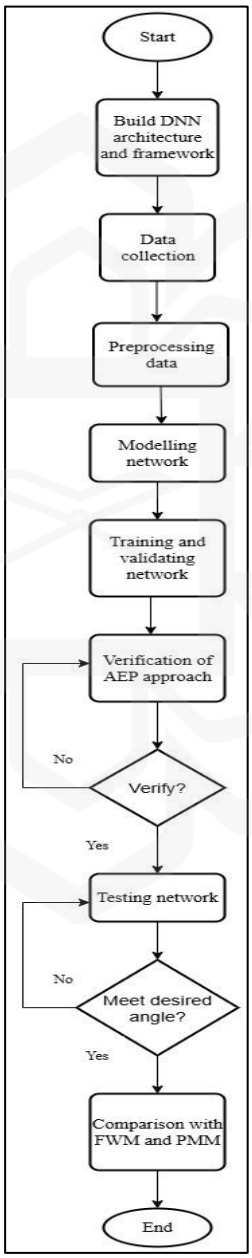

Figure 4.1 Flowchart of the DNN Model Development

4.3 DEEP NEURAL NETWORK FRAMEWORK

This section presents the framework of the proposed DNN used for predicting optimal phase excitations based on AEP data for beam-steering in a dual-linearly polarised antenna array. The DNN model was developed using MATLAB's Deep Learning Toolbox, and the architecture was carefully designed to balance model complexity, training efficiency, and prediction accuracy.

The deep neural network architecture has more than one hidden layer, referred to as Multilayer Perceptrons (MLPs). MLPs have been utilized in various applications and in this research. Different algorithms are employed to train the learning model; in this analysis, Adaptive Moment Estimation (ADAM) is utilized. ADAM is a newer, computationally efficient, and faster algorithm where learning rates are calculated for each parameter. This algorithm is especially beneficial for optimization problems with large datasets or a high number of parameters (Jais et al., 2019).

For the ADAM optimizer, the backpropagation learning algorithm is implemented. Backpropagation serves as a mechanism to distribute input signals, xi, to the neurons of the hidden layer without conducting any computations. Within each hidden layer neuron, j, input signals, xi are combined with their respective input connections, wji, and the outputs, yj are calculated based on the sum, as expressed by Montaser and Mahmoud (2021):

$$y_j = f\left(\sum w_{ji} x_i\right) \tag{4.1}$$

where *f(·)* could be a simple threshold function such as the linear activation function (*reluLayer*). The output from each layer of neurons is generated. Learning algorithms like ADAM are utilized to adjust the weights of MLP networks. The update in weights between neurons *i* and *j* is determined through the ADAM learning process. The weights are modified according to the formula presented in Equation 4.1. Figure 4.2 shows the architecture of the MLP DNN framework with six layers: an input layer, two hidden layers, two dropout layers, and an output layer.

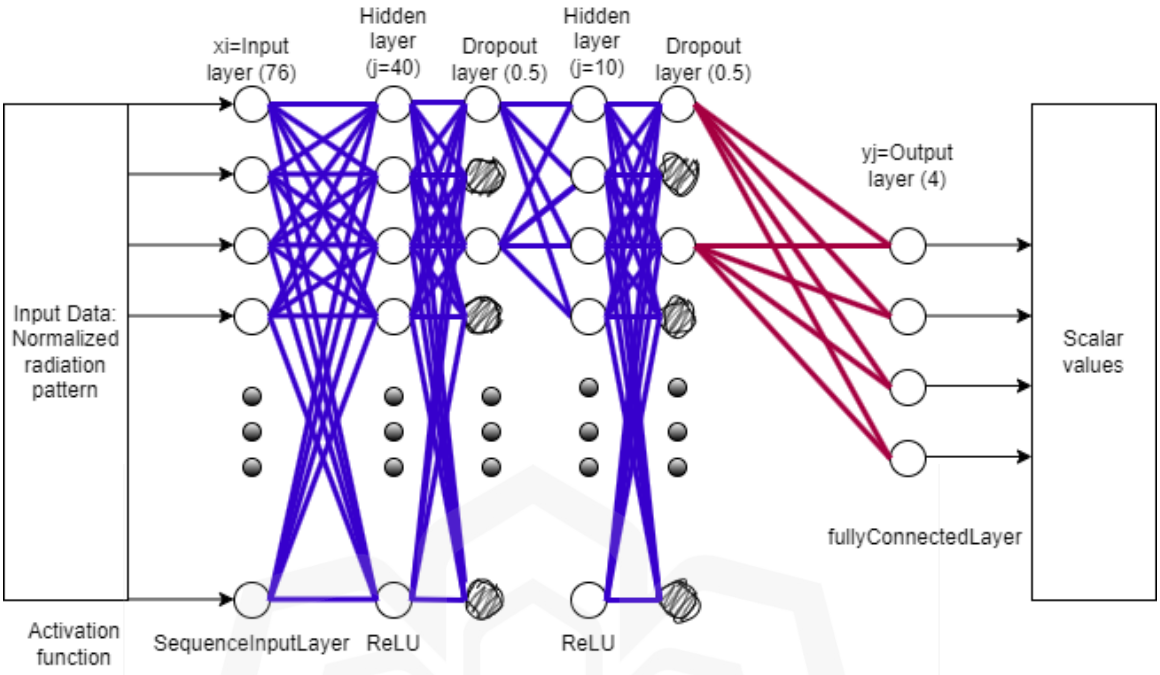

Figure 4.2 The Proposed 6-layer DNN Framework

Moreover, the DNN architecture comprises an input layer (*sequenceInputLayer*), where data-containing neurons are fed into the layer as depicted in Figure 4.2, with each neuron being independent. This architecture was selected after testing various configurations to balance model complexity with generalization performance. Too few layers resulted in underfitting, while additional layers increased training time without significant RMSE improvement. The hidden layers consist of *fullyConnectedLayer*, with *reluLayer* as the activation function, *dropoutLayer*, and a *fullyConnectedLayer* functioning as the output layer. The *sequenceInputLayer* handles sequence data input to the network. All input features were normalized between 0 and 1 using min-max scaling to improve convergence stability. The *fullyConnectedLayer* multiplies the input by a weight matrix and adds a bias vector. The *reluLayer* performs a threshold operation on the input, setting values less than zero to zero to avoid the vanishing gradient. The *dropoutLayer* is integrated to prevent overfitting. Each hidden layer comprises 40 and 10 neurons respectively. The last *fullyConnectedLayer* computes the mean-square error (MSE) or loss, as well as RMSE for regression tasks, and serves as interconnecting layers for feedforward MLP.

The feed-forward neural network used in the learning process is known as a Multilayer Perceptron (MLP) network, with each hidden node's function being supervised. The DNN model was evaluated using separate unseen test sets at angles of 5°, 10°, 15°, and 20° to assess generalization performance. Its performance was validated by comparing the synthesised patterns with full-wave CST simulation results and with ideal desired patterns. The DNN shows strong generalization capability even on unseen data, indicating its potential use in real-time phase control for practical 5G antenna systems. It is noted that this framework currently focuses on phase-only excitation and a fixed 1×4 linear array structure.

4.4 DATA COLLECTION

Figure 4.3 illustrates the simulated proposed DLPAA. The substrate material used is Rogers RT5880 with a relative permittivity of 2.2 and a thickness of 1.575 mm. The patch antennas had a length and width of 3.4 mm and 4.2 mm, respectively. The edge feeding method used is a transmission line model using an SMA connector of 50 Ω for each port. The operating frequency of the antenna is 28 GHz. The inter-element spacing was equal to 15.60 mm (2.159 λ).

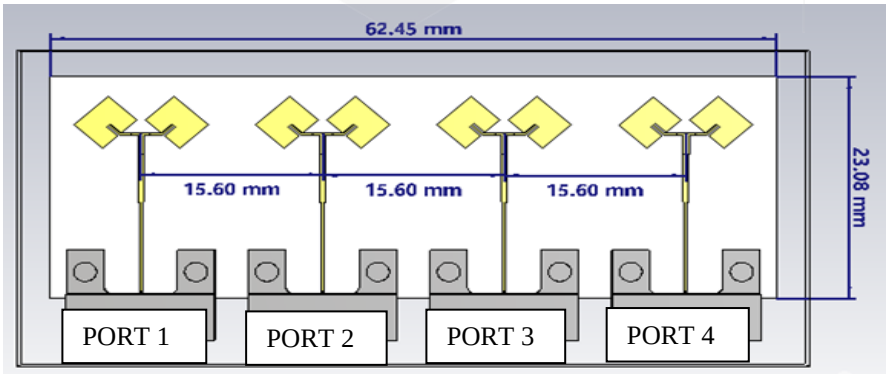

Figure 4.3 The Proposed 1 x 4 ±45° DLPAA

According to Pozar (1994), the array factor is the multiplication of the patterns of each individual element and the array, assuming point sources which represent the total radiation pattern. In this study, the radiation pattern includes mutual coupling. The amplitudes of the input signals of the antenna array are fixed at 1. For the scenario when coupling is present, the amplitude and phase of the signal are used to synthesise the array radiation pattern and are determined using the AEP-based method.

In order to optimize the weight coefficients of the proposed DLPAA using the DNN model, an AEP-based method is used to collect a large amount of data as the input variables to the algorithm. The AEP of the proposed DLPAA is an electric field value for each number of ports (E^n) as shown in Equation 4.2 and 4.3. In this study, the amplitude (I_n) is fixed to 1 and phases ($\emptyset_n$) are varied for each port (He & Wang, 2008):

$$E_{AEP} = \sum_{n=1}^{4} I_n E^n(\theta, \varphi) e^{jka_n cos(\emptyset_n) sin\theta} \quad (4.2)$$

$$a_n = \left(n - \frac{N+1}{2}\right) d, \qquad n = 1,2,3,4. \quad (4.3)$$

I_n is the complex value of feed current applied to the nth element; $E^n(\theta, \varphi)$ is the electric field value at each nth port within the theta, θ range -175° to 180° at cut angle phi, φ of 90°. k is the constant wavenumber, $k = 2\pi f\sqrt{DE}/c$, ($c = 3x10^8\ m/s$, $f = 28\ GHz$, dielectric constant, DE = 2.2); d is the inter-element spacing, $d = 15.60\ mm$ ($2.159\ \lambda$); $\emptyset$ is the phase; θ is the theta range -175° to 180° with a step size of 5°.

As the orientation of the proposed DLPAA for the execution of AEP value is in the y-direction linearly, therefore, AEP_n is obtained from the CST tool by selecting the absolute E-field (linear scale) at the cut angle phi = 90° and theta varied with 5°. Then, the American Standard Code for Information Interchange (ASCII) file in *'.txt'* format is exported at post-processing column for each selected port (port 1 till port 4). These ASCII files contain the real absolute numbers at each 5° theta intervals as shown in Figure 4.4. The extracted ASCII file for port is the absolute E-field at port 1 and it is named as AEP1. Similar steps for the

other extracted ASCII files for respective ports that indicate AEP2, AEP3, and AEP4. The total number of absolute E-field values at each port is 72 which indicates 72 theta angles ranging from -175° to 180°.

All extracted AEP values for each port are then imported to the Excel file named "AEP.xlsx". The Excel file is going to be used as input variables for MATLAB programming to execute the total radiation pattern using the formula shown in Equations 4.2 and 4.3. Appendix A shows the MATLAB code for the execution of training and validation data using Equations 4.2 and 4.3.

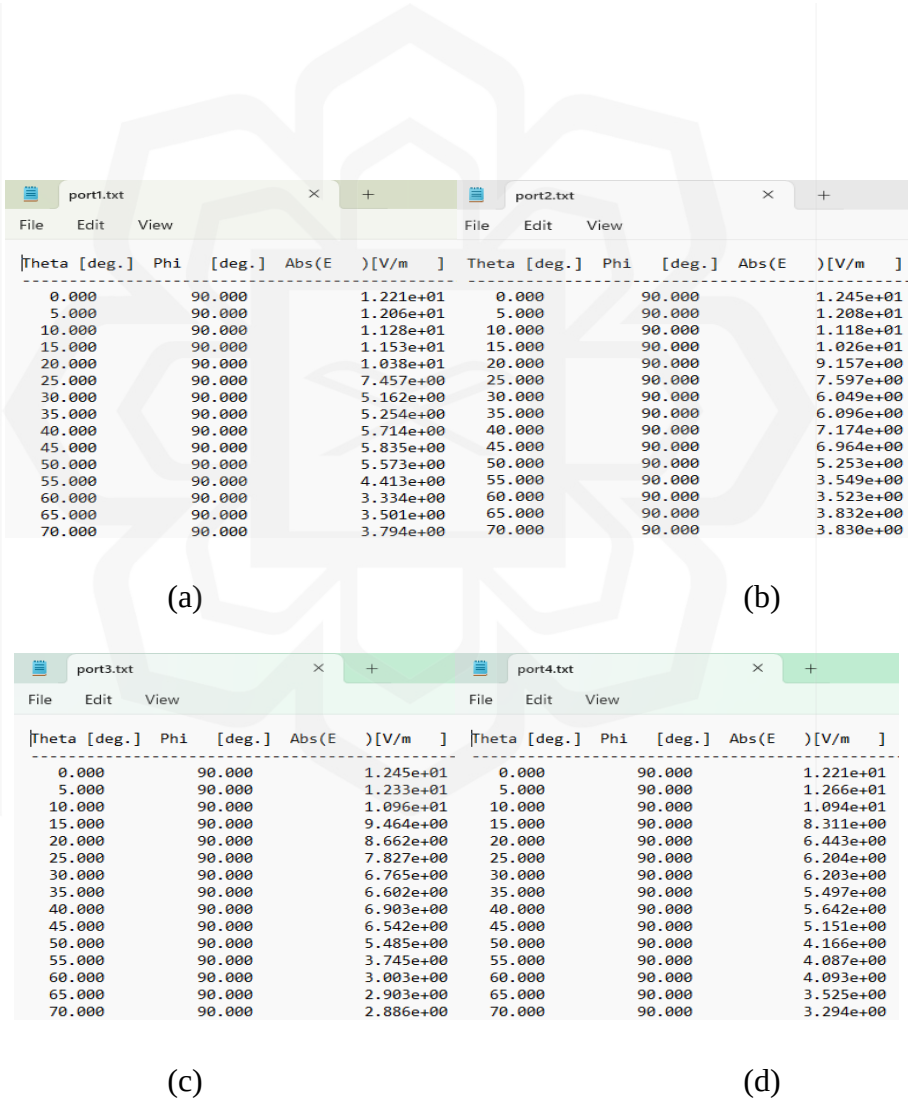

port1.txt

File Edit View

Theta [deg.]	Phi [deg.]	Abs(E)[V/m]
0.000	90.000	1.221e+01
5.000	90.000	1.206e+01
10.000	90.000	1.128e+01
15.000	90.000	1.153e+01
20.000	90.000	1.038e+01
25.000	90.000	7.457e+00
30.000	90.000	5.162e+00
35.000	90.000	5.254e+00
40.000	90.000	5.714e+00
45.000	90.000	5.835e+00
50.000	90.000	5.573e+00
55.000	90.000	4.413e+00
60.000	90.000	3.334e+00
65.000	90.000	3.501e+00
70.000	90.000	3.794e+00

(a)

port2.txt

File Edit View

Theta [deg.]	Phi [deg.]	Abs(E)[V/m]
0.000	90.000	1.245e+01
5.000	90.000	1.208e+01
10.000	90.000	1.118e+01
15.000	90.000	1.026e+01
20.000	90.000	9.157e+00
25.000	90.000	7.597e+00
30.000	90.000	6.049e+00
35.000	90.000	6.096e+00
40.000	90.000	7.174e+00
45.000	90.000	6.964e+00
50.000	90.000	5.253e+00
55.000	90.000	3.549e+00
60.000	90.000	3.523e+00
65.000	90.000	3.832e+00
70.000	90.000	3.830e+00

(b)

port3.txt

File Edit View

Theta [deg.]	Phi [deg.]	Abs(E)[V/m]
0.000	90.000	1.245e+01
5.000	90.000	1.233e+01
10.000	90.000	1.096e+01
15.000	90.000	9.464e+00
20.000	90.000	8.662e+00
25.000	90.000	7.827e+00
30.000	90.000	6.765e+00
35.000	90.000	6.602e+00
40.000	90.000	6.903e+00
45.000	90.000	6.542e+00
50.000	90.000	5.485e+00
55.000	90.000	3.745e+00
60.000	90.000	3.003e+00
65.000	90.000	2.903e+00
70.000	90.000	2.886e+00

(c)

port4.txt

File Edit View

Theta [deg.]	Phi [deg.]	Abs(E)[V/m]
0.000	90.000	1.221e+01
5.000	90.000	1.266e+01
10.000	90.000	1.094e+01
15.000	90.000	8.311e+00
20.000	90.000	6.443e+00
25.000	90.000	6.204e+00
30.000	90.000	6.203e+00
35.000	90.000	5.497e+00
40.000	90.000	5.642e+00
45.000	90.000	5.151e+00
50.000	90.000	4.166e+00
55.000	90.000	4.087e+00
60.000	90.000	4.093e+00
65.000	90.000	3.525e+00
70.000	90.000	3.294e+00

(d)

Figure 4.4 ASCII file for (a) AEP1 (b) AEP2 (c) AEP3 and (d) AEP4

To ensure the generalizability of machine learning algorithms, datasets should be divided into three segments: training set, validation set, and test set. The training set is used for model fitting, while the validation set evaluates the model's performance. The test set evaluates the model's generalization to unseen data and practical scenarios. This separation helps establish a reliable benchmark for the model's performance, preventing potential issues like overfitting. The training, validation, and test datasets should not overlap with each other, meaning they have separate datasets crucial for data reliability, accuracy, and unbiased results.

As previously mentioned, the amplitude of each port, I_n is fixed to 1 and the phases of each port, $\emptyset_n$ are varied. By increasing the phase input signals by 20°, the training data is executed. For the training data extraction, 19 cases are produced, resulting in a total of 1 x 19 x 19 x 19 = 6,859 radiation patterns. It is essential that the validation data and training data do not overlap in order to validate the network.

Data collection for the initial phase of validation begins at 10°, increased by 40°, and ends at 130°. With 4 cases produced, the total number of radiation patterns is 1 x 4 x 4 x 4 = 64. Tables 4.1 and 4.2 display the amplitude and phase input signals of the proposed DLPAA for each training and validation dataset. Port 4 is set at 0° as the reference port.

Table 4.1 The Amplitude (I_n) and Phase ($\emptyset_n$) Input Signals for the Training Dataset

Port	**Amplitude (I_n)**	**Phase ($\emptyset_n$)**	**Number of Cases**
1	1	0°,20°,40°,…,340°,360°	19
2	1	0°,20°,40°,…,340°,360°	19
3	1	0°,20°,40°,…,340°,360°	19
4	1	0°	1

Table 4.2 The Amplitude (I_n) and Phase ($\emptyset_n$) Input Signals for the Validation Dataset

Port	**Amplitude (I_n)**	**Phase ($\emptyset_n$)**	**Number of Cases**
1	1	10°,50°,90°,130°	4
2	1	10°,50°,90°,130°	4
3	1	10°,50°,90°,130°	4
4	1	0°	1

Based on Appendices A, C, and D, the data collection of the total radiation pattern is computed by summing the AEPs (from port 1 to port 4). The AEP values are extracted from CST Studio software at each port and inputted into MATLAB. The phase input signals are in radians. The amplitude and phase input signals are assigned to variable W. The phase variable assigned to variable W varies from 1 to 19 to indicate the phase input value in radians. The exponential function comprising real and imaginary numbers is utilized in this script.

For the test phase dataset, the amplitude (I_n) is set at 1 and the port's phase is determined by the phase shift difference between adjacent ports. The desired main beam direction, θ is set to 5°, 10°, 15°, and 20° and inputted into the Equation 4.4 to obtain the phase value, β. Each test dataset phase is fed into the DNN model separately. The input phases of the test data are in radians, as the computation of AEP is also in radians. Appendix C shows the MATLAB code for computing the phase shift difference as the initial input phases to the DNN model, β, (Alam et al., 2024):

$$\beta = kdcos(\theta) \tag{4.4}$$

β is the phase value in radian; k is 2 π/λ_g; d is 15.60; and θ is the desired angle (5°, 10°, 15°, and 20°).

4.5 PREPROCESSING DATA

Preprocessing is a critical step in preparing data for effective DNN training. It ensures that all input features are scaled consistently, which helps the network converge more efficiently and avoids dominance of certain features due to magnitude differences. In this work, the input data is derived from AEPs simulated in CST, and the target outputs are the excitation phase values for each of the four antenna elements. Figure 4.2 displays the architecture of the DNN framework which includes input and output of the DNN. The type of input and output is crucial as the learning algorithm depends on these. The extracted AEPs from CST are in units of 5° ranges from -175° to 180°. The collection of radiation pattern data by AEP computation consists of collected training and validation data, in complex integers value, serving as inputs to the DNN model. These inputs undergo preprocessing, converting them into a scalar value ranging from 0 to 1 with a total of 72 input data points as shown in Figure 4.2. The preprocessing is carried out by dividing the absolute value of collected training and validation data by its maximum value at each θ° interval (-175°:5°:180°) to normalize the input variables from 0 to 1, as shown in the MATLAB code in Appendix A. Equation 4.5 shows the formula used to calculate the normalized inputs which is referred to as preprocessing data.

Each input sample to the DNN consists of a 72-element normalized vector representing the AEP pattern across the theta range. The corresponding output is a 4-element vector containing the optimal phase excitations for the four antenna elements. These phase values are converted from degrees to radians and then scaled to a normalized range between 0 and 1 prior to training. After model inference, the outputs are denormalized and converted back to degrees for evaluation and beam synthesis.

$$Normalized\ inputs = abs\left(\frac{inputs\ value}{\max\left(inputs\ value\right)}\right) \tag{4.5}$$

4.5.1 Training and Validation Datasets

A total of 6859 training data and 64 validation datasets are computed. The amplitude and phase input signal values are assigned to the input variables for the AEP-DNN method computation inside MATLAB. The extracted patterns are two-dimensional, with values in units of 5°. The radiation pattern corresponds to the azimuth plane of the proposed DLPAA for observing its main beam-steering. Figure 4.5 shows a part of the training and validation datasets in Excel file format.

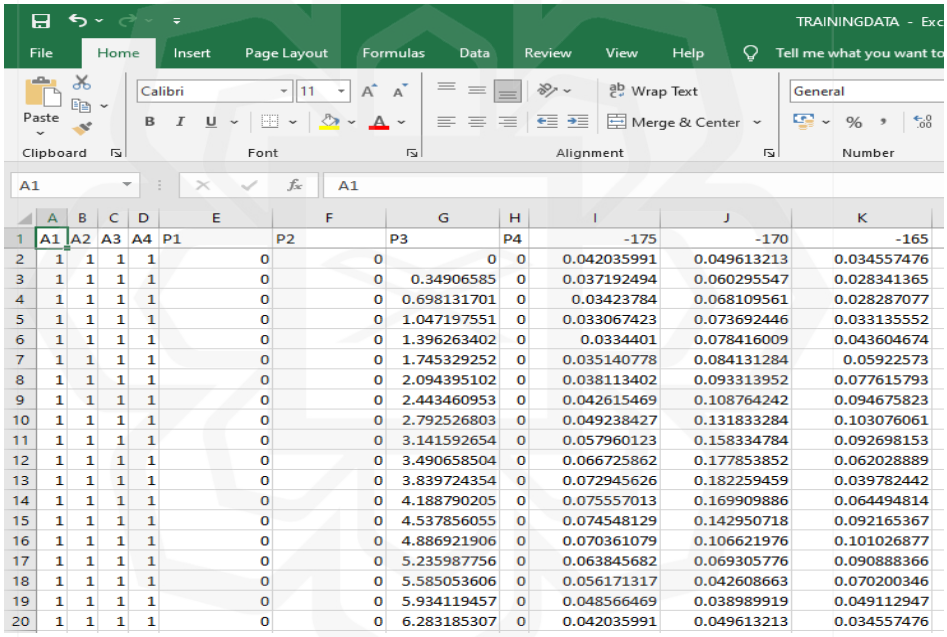

A1	A2	A3	A4	P1	P2	P3	P4	-175	-170	-165
1	1	1	1	0	0	0	0	0.042035991	0.049613213	0.034557476
1	1	1	1	0	0	0.34906585	0	0.037192494	0.060295547	0.028341365
1	1	1	1	0	0	0.698131701	0	0.03423784	0.068109561	0.028287077
1	1	1	1	0	0	1.047197551	0	0.033067423	0.073692446	0.033135552
1	1	1	1	0	0	1.396263402	0	0.0334401	0.078416009	0.043604674
1	1	1	1	0	0	1.745329252	0	0.035140778	0.084131284	0.05922573
1	1	1	1	0	0	2.094395102	0	0.038113402	0.093313952	0.077615793
1	1	1	1	0	0	2.443460953	0	0.042615469	0.108764242	0.094675823
1	1	1	1	0	0	2.792526803	0	0.049238427	0.131833284	0.103076061
1	1	1	1	0	0	3.141592654	0	0.057960123	0.158334784	0.092698153
1	1	1	1	0	0	3.490658504	0	0.066725862	0.177853852	0.062028889
1	1	1	1	0	0	3.839724354	0	0.072945626	0.182259459	0.039782442
1	1	1	1	0	0	4.188790205	0	0.075557013	0.169909886	0.064494814
1	1	1	1	0	0	4.537856055	0	0.074548129	0.142950718	0.092165367
1	1	1	1	0	0	4.886921906	0	0.070361079	0.106621976	0.101026877
1	1	1	1	0	0	5.235987756	0	0.063845682	0.069305776	0.090888366
1	1	1	1	0	0	5.585053606	0	0.056171317	0.042608663	0.070200346
1	1	1	1	0	0	5.934119457	0	0.048566469	0.038989919	0.049112947
1	1	1	1	0	0	6.283185307	0	0.042035991	0.049613213	0.034557476

(a)

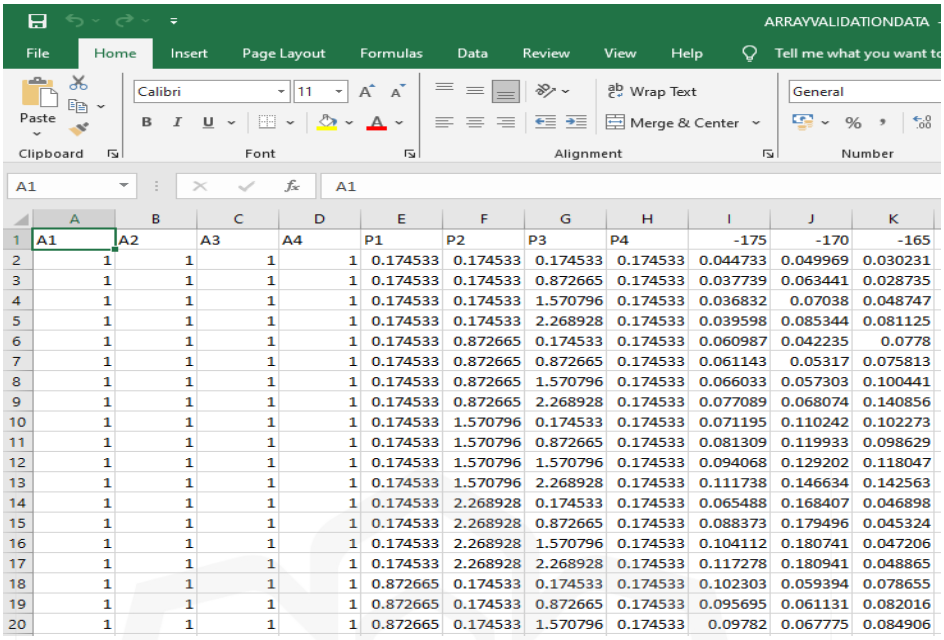

ARRAYVALIDATIONDATA

File Home Insert Page Layout Formulas Data Review View Help Tell me what you want to

Paste Clipboard Calibri 11 Font Wrap Text Merge & Center Alignment General Number

A1

	A	B	C	D	E	F	G	H	I	J	K
1	A1	A2	A3	A4	P1	P2	P3	P4	-175	-170	-165
2	1	1	1	1	0.174533	0.174533	0.174533	0.174533	0.044733	0.049969	0.030231
3	1	1	1	1	0.174533	0.174533	0.872665	0.174533	0.037739	0.063441	0.028735
4	1	1	1	1	0.174533	0.174533	1.570796	0.174533	0.036832	0.07038	0.048747
5	1	1	1	1	0.174533	0.174533	2.268928	0.174533	0.039598	0.085344	0.081125
6	1	1	1	1	0.174533	0.872665	0.174533	0.174533	0.060987	0.042235	0.0778
7	1	1	1	1	0.174533	0.872665	0.872665	0.174533	0.061143	0.05317	0.075813
8	1	1	1	1	0.174533	0.872665	1.570796	0.174533	0.066033	0.057303	0.100441
9	1	1	1	1	0.174533	0.872665	2.268928	0.174533	0.077089	0.068074	0.140856
10	1	1	1	1	0.174533	1.570796	0.174533	0.174533	0.071195	0.110242	0.102273
11	1	1	1	1	0.174533	1.570796	0.872665	0.174533	0.081309	0.119933	0.098629
12	1	1	1	1	0.174533	1.570796	1.570796	0.174533	0.094068	0.129202	0.118047
13	1	1	1	1	0.174533	1.570796	2.268928	0.174533	0.111738	0.146634	0.142563
14	1	1	1	1	0.174533	2.268928	0.174533	0.174533	0.065488	0.168407	0.046898
15	1	1	1	1	0.174533	2.268928	0.872665	0.174533	0.088373	0.179496	0.045324
16	1	1	1	1	0.174533	2.268928	1.570796	0.174533	0.104112	0.180741	0.047206
17	1	1	1	1	0.174533	2.268928	2.268928	0.174533	0.117278	0.180941	0.048865
18	1	1	1	1	0.872665	0.174533	0.174533	0.174533	0.102303	0.059394	0.078655
19	1	1	1	1	0.872665	0.174533	0.872665	0.174533	0.095695	0.061131	0.082016
20	1	1	1	1	0.872665	0.174533	1.570796	0.174533	0.09782	0.067775	0.084906

(b)

Figure 4.5 (a) Training and (b) Validation Datasets

4.6 MODELLING NETWORK

The DNN framework consists of 6 layers. The input, hidden, and output layers are "*sequenceInputLayer*", "*ReLU*", and "*fullyConnectedLayer*". The "*dropoutLayer(0.5)*" is also used to avoid overfitting learning data with 0.5 set by default. Each layer employs a dense layer that connects input and output neurons completely. The number of neurons in each hidden layer is 40 and 10 as shown in Figure 4.2. The modelling network code is shown in Appendix D inside the "*layers*" column.

4.7 TRAINING, VALIDATING AND TESTING NETWORK

The model training phase uses 6859 input to optimize network weights, while the validation phase evaluates the generalization of the model on 64 unseen combinations. The final testing phase evaluates DNN performance on beam directions (5°, 10°, 15°, 20°), which were not part of the training or validation datasets. During the training process, the weights are adjusted to make the predicted DNN pattern close to the desired pattern of the network. In this study, 6859 radiation pattern data of the proposed DLPAA are used for training. ADAM Optimizer is used as one of the training options during the training network.

InitialLearnRate is the initial learning rate used for training, specified as a positive scalar. If the learning rate is too low, then training takes a long time. If the learning rate is too high, then training could reach a suboptimal result. For many datasets, it is advisable to use a much lower initial learning rate to achieve its optimum accuracy, which in this study is 0.001. *LearnRateSchedule* is set to 'none', where the learning rate remains constant throughout training. *GradientThreshold* is set to '1'; if the gradient exceeds this value, it is clipped as specified by the *GradientThresholdOption*. *GradientDecayFactor* is set to '0.9', which is the decay rate of the gradient moving average for the ADAM solver, specified as a nonnegative scalar less than 1. *SquaredGradientDecayFactor* is 0.99, which is the decay rate of the squared gradient moving average for the ADAM solver, also specified as a nonnegative scalar less than 1. All these hyperparameters are set to the default value.

L2Regularization is the factor for L2 regularizer (weight decay), specified as a nonnegative scalar to reduce overfitting, which is 0.0000001. The number of epochs is set to 2500 for training 2500 times. The number of training epochs is varied based on convergence trends for each steering angle to ensure optimal performance while avoiding overfitting. The batch size is set to 50. The *maxEpochs* is the maximum number of epochs (full passes of the data) used for training, specified as a positive integer. The *MiniBatchSize* is the size of the mini-batch used for each training iteration, specified as a positive integer. A mini-batch is a subset of the training set used to evaluate the gradient of the loss function and update the weights. If the mini-batch size does not evenly divide the number of training

samples, then the software discards the training data that does not fit into the final complete mini-batch of each epoch. If the mini-batch size is smaller than the number of training samples, then the software does not discard any data. All these hyperparameters are tuned to obtain the best training and validation RMSE and loss performance.

Meanwhile, the option for data shuffling under *Shuffle* is set to 'never'. For the *Verbose*, it is set to 'true', meaning the flag to display training progress information in the command window, specified as 1 (true) or 0 (false). The content of the verbose output depends on the function that is used for training. The *Metrics* function is 'RMSE', which is the root mean squared error that estimates the standard deviation of the error distribution. The *Plots* are set to 'training-progress' to display during the neural network training. The '*minibatchpredict*' function is used to predict numeric responses of sequences using the trained ADAM Network. ADAM is an optimization algorithm that could be used instead of the classical stochastic gradient descent procedure to update network weights iteratively based on training data. Table 4.3 shows the number of epochs for each desired steering angle. The hyperparameter tuning is necessary to obtain the desired steering angle of the main beam. Tuning the hyperparameter of number of epochs does not affect the accuracy of the RMSE and loss performance.

Table 4.3 Number of Epochs

Desired Steering Angles (°)	**Number of Epochs**
5	2000
10	2000
15	2500
20	2500

This iterative process employs the backpropagation method. For each iteration, the weights are modified (Montaser & Mahmoud, 2021). Figure 4.6 shows the RMSE performance of this AEP-DNN network. One of the key benefits of neural networks is their capacity for generalization, which enables them to categorize data even if a trained network has never encountered data belonging to the same class as the learning data.

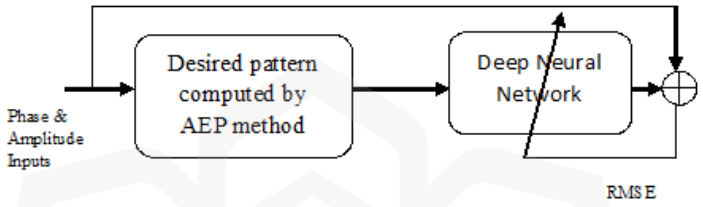

Figure 4.6 The RMSE Procedure

To observe the steering angle of the main beam at a desired angle, a testing network is required. The initial phases and desired pattern are inputted into DNN. The prediction from the training network would execute the predicted phases, and the AEP method computes the desired pattern. The predicted phases are also inputted into the CST to obtain the CST pattern. These three radiation patterns are compared and presented. The selected desired main beam angles to be investigated in this study are 5°, 10°, 15°, and 20°.

To evaluate the performance of the developed DNN model quantitatively, and verify whether there is any underlying trend in the performance of DNN models, the training and validation loss were conducted. For the regression network output, the loss is the half-mean-squared-error. The half mean squared error operation computes the half mean squared error loss between network pattern predictions and desired pattern for regression tasks as shown in Equation 4.6. RMSE is used to evaluate prediction accuracy, with lower RMSE indicating better alignment between the predicted and desired phase values. The loss or MSE is calculated using the following formula, and RMSE is the square root of the MSE as shown in Equation 4.7 (Montaser & Mahmoud, 2021):

$$MSE = \frac{1}{2N}\sum_{i=1}^{M}(X_i - T_i)^2 \quad (4.6)$$

$$RMSE = \sqrt{MSE} \quad (4.7)$$

where X_i is the network pattern predictions, T_i is the desired pattern, M is the total number of predicted phases in X which is 4 (across all observations), and N is the total number of theta angles in X which is 72. The predicted DNN phases output is expressed as a scalar value. Outputs 1 till 4 are the predicted DNN phases respectively.

The desired main beam angle is inserted into Equation 4.4, and the phase value in radians is obtained. These phase values and the total radiation pattern are inputted into the MATLAB computation of the DNN algorithm to predict the DNN phase values to steer the main beam pattern to the desired angle. The desired pattern is determined by setting the main lobe at the desired angle to 1, indicating the normalized pattern at its maximum, with a beamwidth of 10° and the sidelobe level at -5 dB. The best sidelobe level should be lower than -10 dB. However, the DNN learning algorithm is precisely dependent on the given input data. If the sidelobe level is set to approximately lower than 0.1, it would be an unrealistic value for such a high frequency antenna, specifically at millimeter-wave frequency. In order to avoid the possibility of inaccuracy in the learning algorithm, which is fully dependent on the given training and validation data, the sidelobe level is set to the average value of the sidelobe levels in both the training and validation data. Please keep in mind that the aim of this study is to observe the ability of a dual-polarised antenna at 28 GHz to steer the main beam to a desired angle using the AEP-DNN algorithm, not to lower the sidelobe level.

4.8 VERIFICATION OF AEP METHOD USING PMM AND CST

It is crucial to verify the reliability of the AEP method by the Pattern Multiplication Method (PMM) using MATLAB and a full-wave model using CST. Therefore, some sample datasets are chosen. The amplitude (I_n) is fixed at 1. The selected phases datasets are shown in Table 4.4.

Table 4.4 The PMM, AEP, and CST Phases of Verification Sample Dataset

Datasets	**Phases**
1	0° 0° 0° 0°
2	10° 50° 90° 10°
3	25° 35° 45° 55°

For the above data, the radiation pattern of these selected sets was obtained by the AEP method through computation with MATLAB, as explained in Section 4.4 earlier. The same amplitude and phase values are used to obtain the radiation pattern by CST Simulation tool. These values are set in the *'post-processing'* tab, where the amplitude and phase value for each port are inputted, and the tool would automatically simulate the proposed DLPAA to the desired pattern. The acquired radiation pattern is then displayed, and the scale is set to *'Abs E-field'* of *'linear scaling'* at a cut angle of 90° (azimuth). The pattern is then extracted by exporting it to an ASCII file. Now, the acquired radiation pattern file by CST is imported into Excel for further verification, as shown in Figure 4.7. It is important to verify the AEP method with a full-wave modeling tool (CST) to ensure its accuracy.

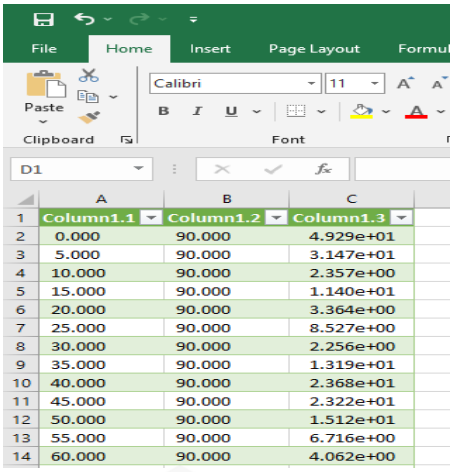

	A	B	C
1	Column1.1	Column1.2	Column1.3
2	0.000	90.000	4.929e+01
3	5.000	90.000	3.147e+01
4	10.000	90.000	2.357e+00
5	15.000	90.000	1.140e+01
6	20.000	90.000	3.364e+00
7	25.000	90.000	8.527e+00
8	30.000	90.000	2.256e+00
9	35.000	90.000	1.319e+01
10	40.000	90.000	2.368e+01
11	45.000	90.000	2.322e+01
12	50.000	90.000	1.512e+01
13	55.000	90.000	6.716e+00
14	60.000	90.000	4.062e+00

Figure 4.7 The CST Pattern Data

The same amplitude and phase values are used to obtain the radiation pattern using MATLAB by PMM, computing the array factor of each input phase as shown in Table 4.8 and multiplying them with the single element pattern (SEP) as shown in Equation 4.8. The computation of the array factor using MATLAB is shown in Appendix B.

$$PMM\ pattern\ data = SEP(AF) \tag{4.8}$$

AF is the array factor obtained from MATLAB. SEP is the single element pattern obtained from the proposed ±45° dual-polarised antenna. The accuracy of the AEP-DNN method is achieved by using realistic antenna behavior through the AEP, which includes the effects of mutual coupling between elements. These AEP values are taken from CST simulations and used in the training data to represent how each antenna port actually performs. A total of 6859 training datasets were created with fixed amplitude and varying phase values, allowing the deep neural network to learn how different input phases affect the beam pattern. The model's accuracy was measured using RMSE and loss values, where the RMSE was around 1.5 for training and 1.3 for validation, and the validation loss was between 1.7 and 1.9.

Figure 4.8 shows the PMM, AEP, and CST patterns for each phase dataset. The sidelobe levels of the AEP pattern are much lower than those of the PMM and CST patterns. It shows that the peak gain and radiation pattern shape between PMM, AEP, and CST are well agreed to each other. Therefore, this AEP method is successfully verified and further implemented into DNN algorithm in the next section.

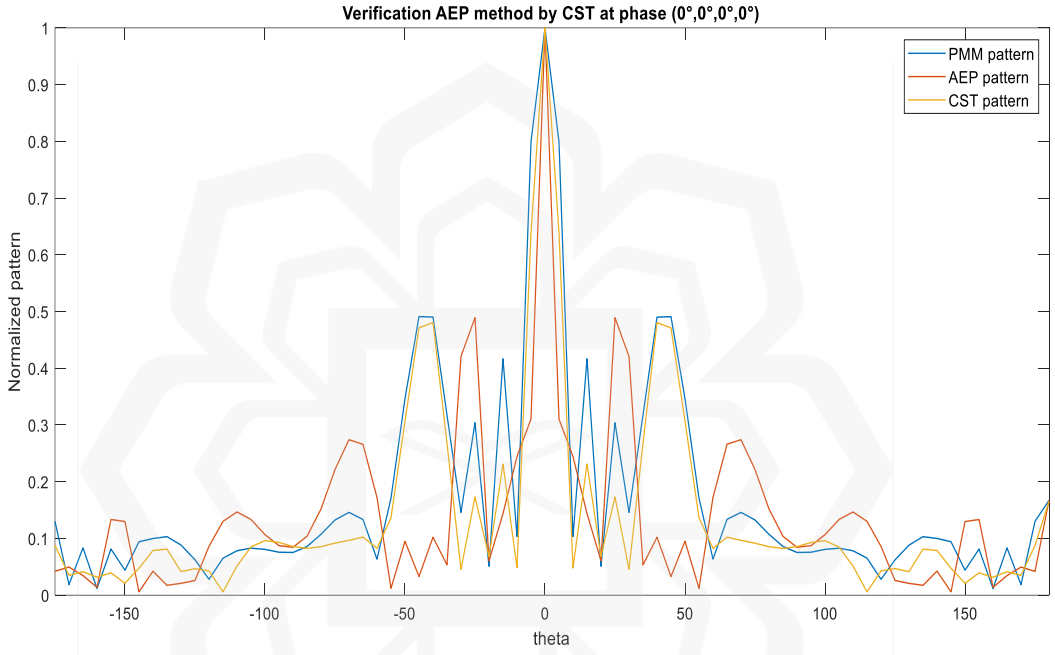

(a)

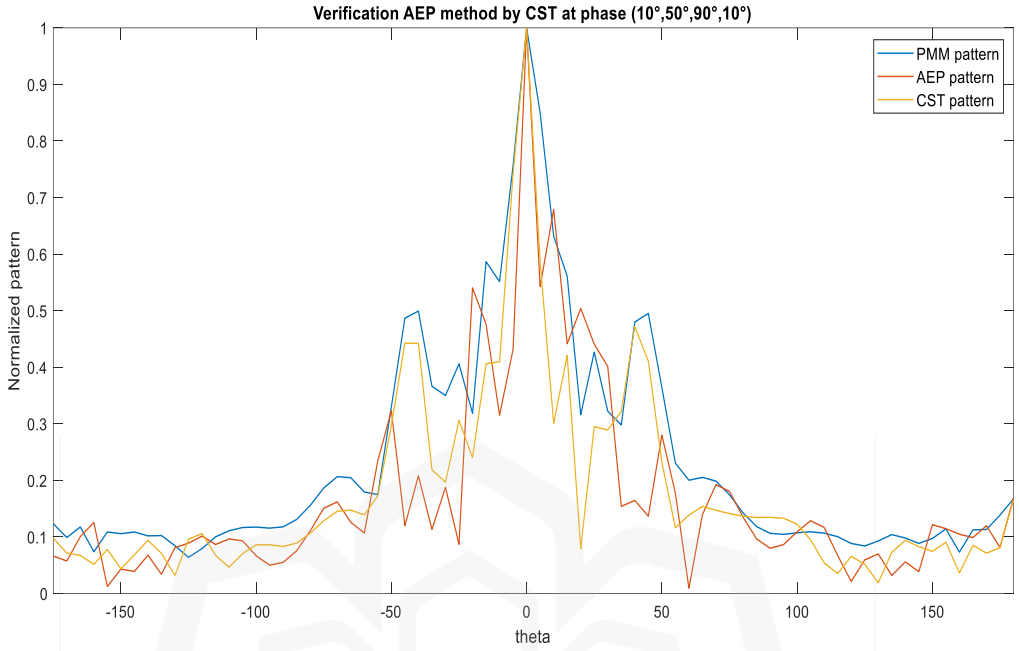

(b)

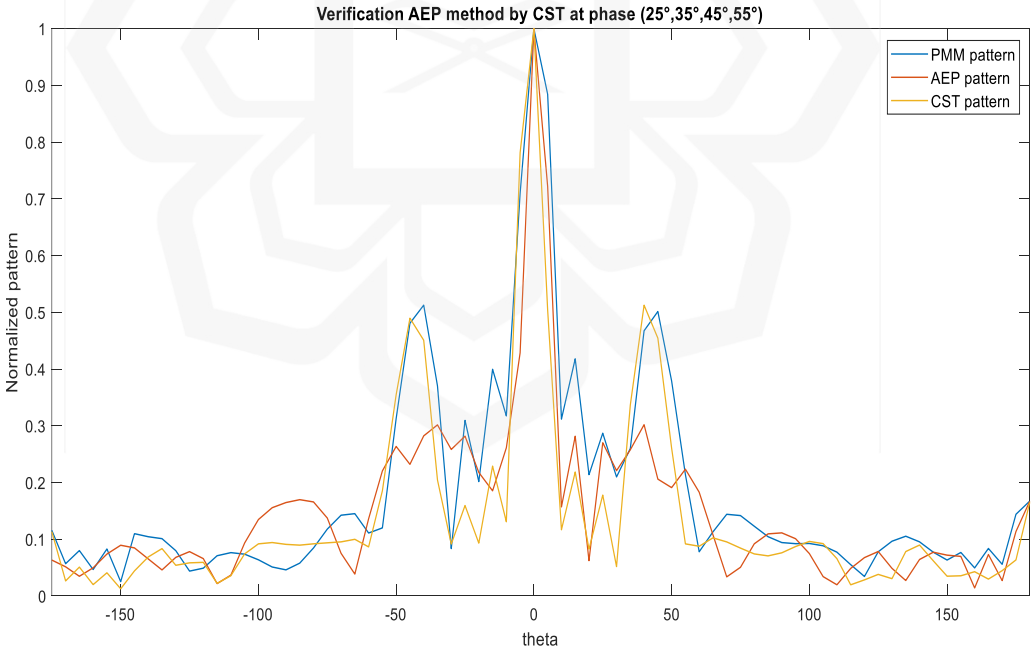

(c)

Figure 4.8 Verification of AEP Method with PMM and CST at (a) phase 0° 0° 0° 0°, (b) Phase 10° 50° 90° 10°, and (c) phase 25° 35° 45° 55°

4.9 AEP-DNN RESULTS

For estimating initial phase datasets by Equation 4.4, the datasets are shown in Table 4.5. The predicted phases obtained after DNN learning at each desired main beam angle are also shown in the table. Figure 4.9 shows the desired pattern, predicted AEP-DNN pattern, PMM pattern, and CST pattern in normalized form. The maximum at 1 indicates the main beam location. The AEP-DNN pattern data is obtained by inserting the predicted phases into the AEP computation in MATLAB as shown in Appendix A. Full-wave modelling method could simulate complex structures with high accuracy but longer time. However, the AEP-DNN method could simulate within shorter time with the same accuracy compared to the full-wave model. The AEP-DNN, PMM, and CST patterns are computed using predicted phase DNN outputs as their input phases while the input phases for the desired pattern are the initial phase inputs as shown in Table 4.5.

Table 4.5 Initial Phases and Predicted Phases of the DNN Model

Desired Main Beam Direction (°)		**5**	**10**	**15**	**20**
Initial Phase inputs (°)	port 1	54	45	30	10
	port 2	0	0	0	0
	port 3	54	45	30	10
	port 4	0	0	0	0

Predicted phase DNN outputs (°)	port 1	218	234	232	274
	port 2	247	43	322	160
	port 3	218	222	77	152
	port 4	17	-20	5	2

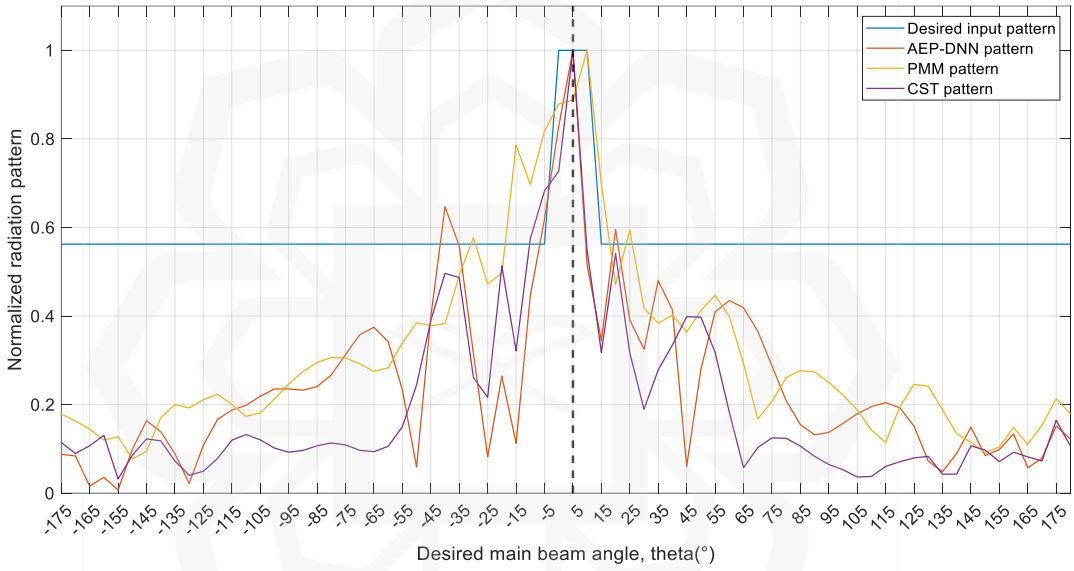

(a)

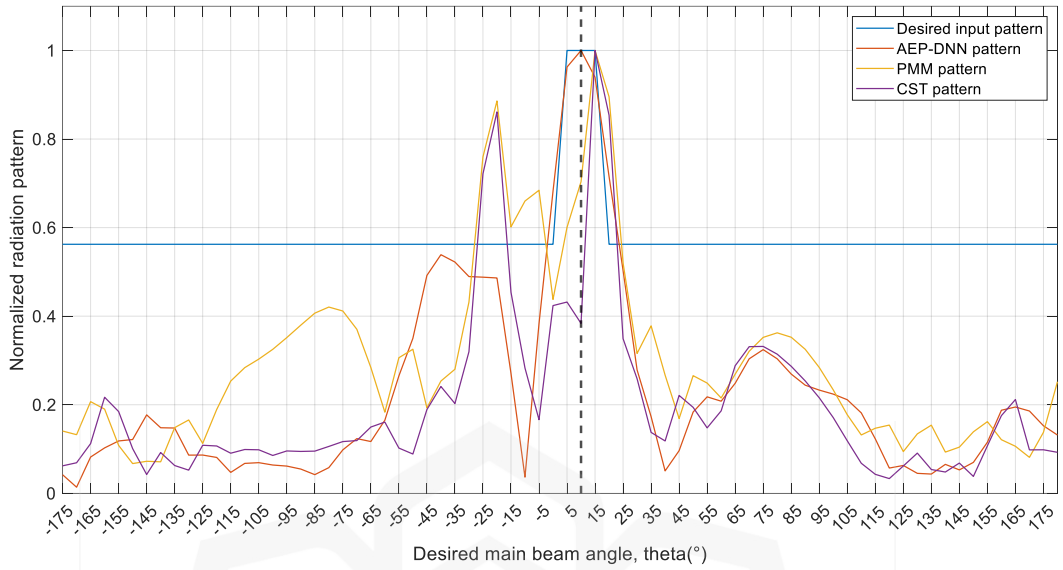
Desired input pattern
AEP-DNN pattern
PMM pattern
CST pattern
Normalized radiation pattern
Desired main beam angle, theta(°)

(b)

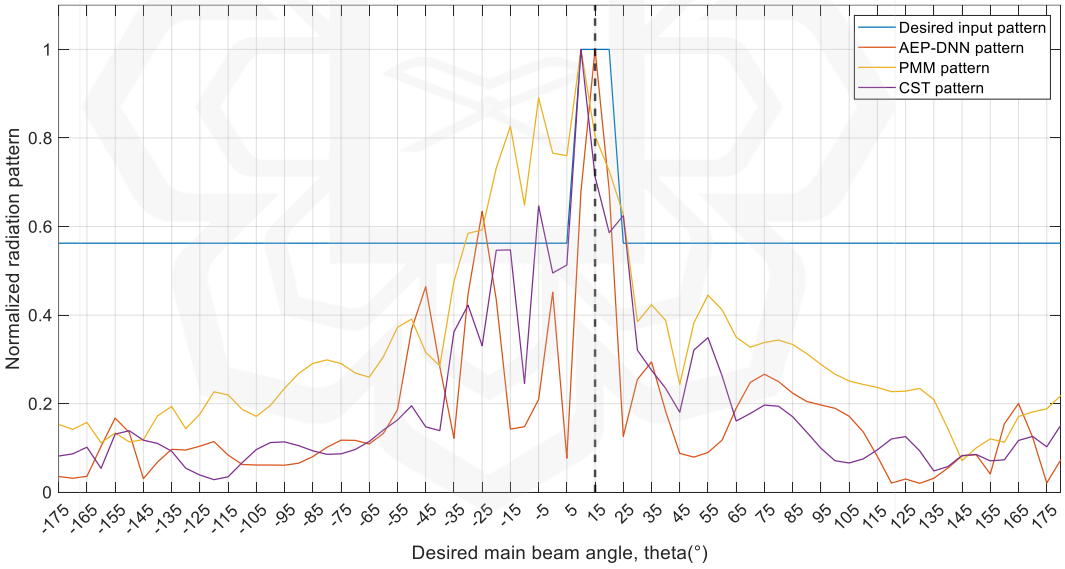
Desired input pattern
AEP-DNN pattern
PMM pattern
CST pattern
Normalized radiation pattern
Desired main beam angle, theta(°)

(c)

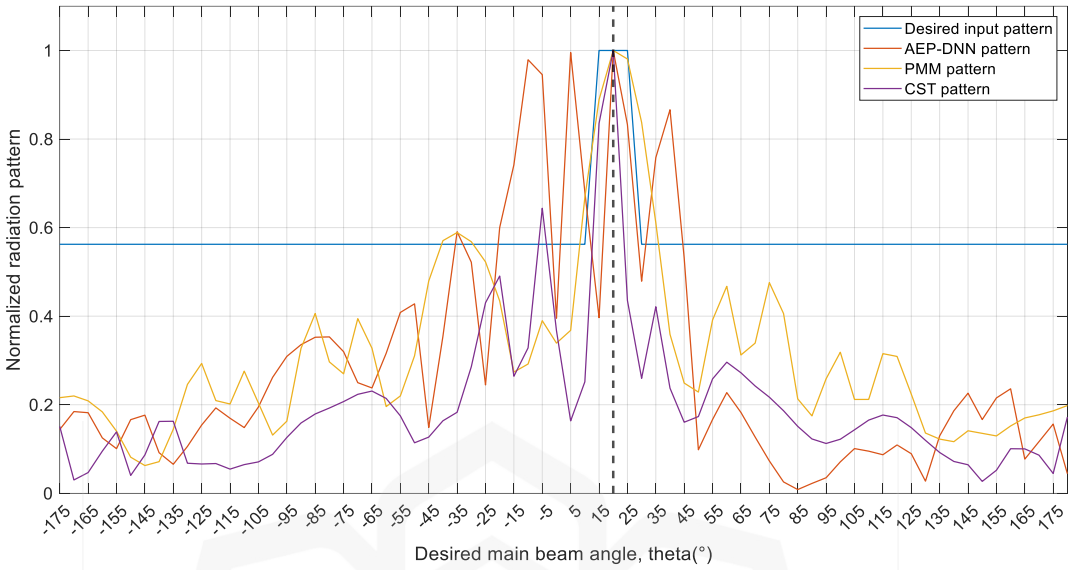

(d)

Figure 4.9 The Desired, AEP-DNN, PMM, and CST Patterns at the Desired Main Beam Angle of (a) 5° (b) 10° (c) 15° and (d) 20°

Based on Figure 4.9, it shows that the main beam of predicted AEP-DNN, PMM, and CST patterns are matched and fall within the main beam of the desired pattern. The beamwidth of the desired pattern is set to 10° as the beamwidth of the main beam shown in Figure 3.34 (c). The simulated the co-polarised azimuth pattern of proposed DLPAA is 10°. The sidelobe level is set to -5 dB since the simulated sidelobe level of proposed DLPAA is on average at this level. Figure 4.10 shows the training and validation RMSE and loss performance.

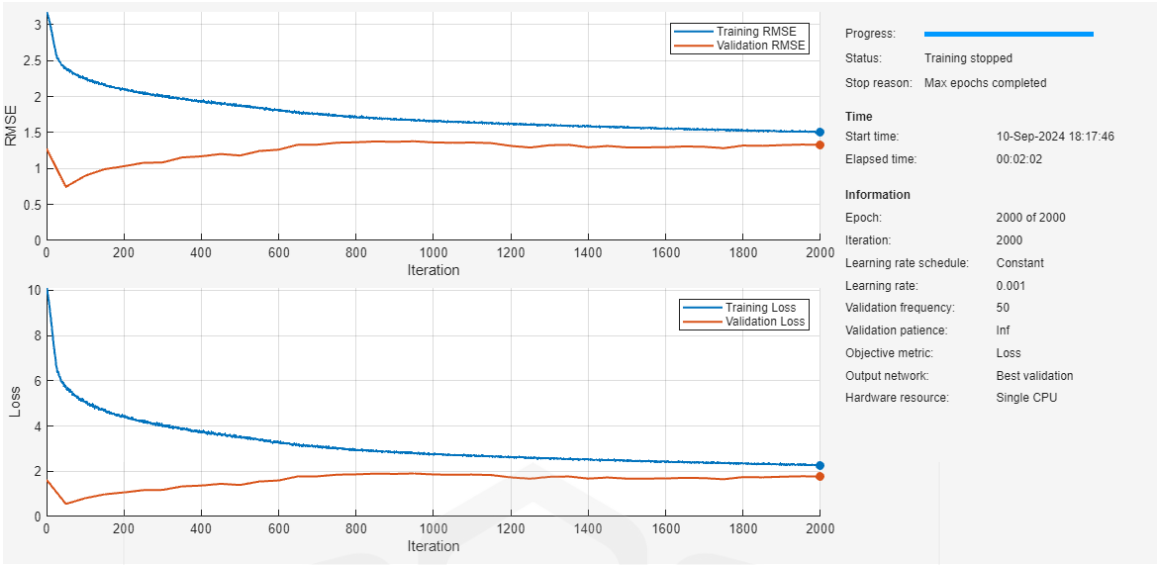
Training RMSE
Validation RMSE
RMSE
Iteration
Training Loss
Validation Loss
Loss
Iteration
Progress:
Status: Training stopped
Stop reason: Max epochs completed
Time
Start time: 10-Sep-2024 18:17:46
Elapsed time: 00:02:02
Information
Epoch: 2000 of 2000
Iteration: 2000
Learning rate schedule: Constant
Learning rate: 0.001
Validation frequency: 50
Validation patience: Inf
Objective metric: Loss
Output network: Best validation
Hardware resource: Single CPU

(a)

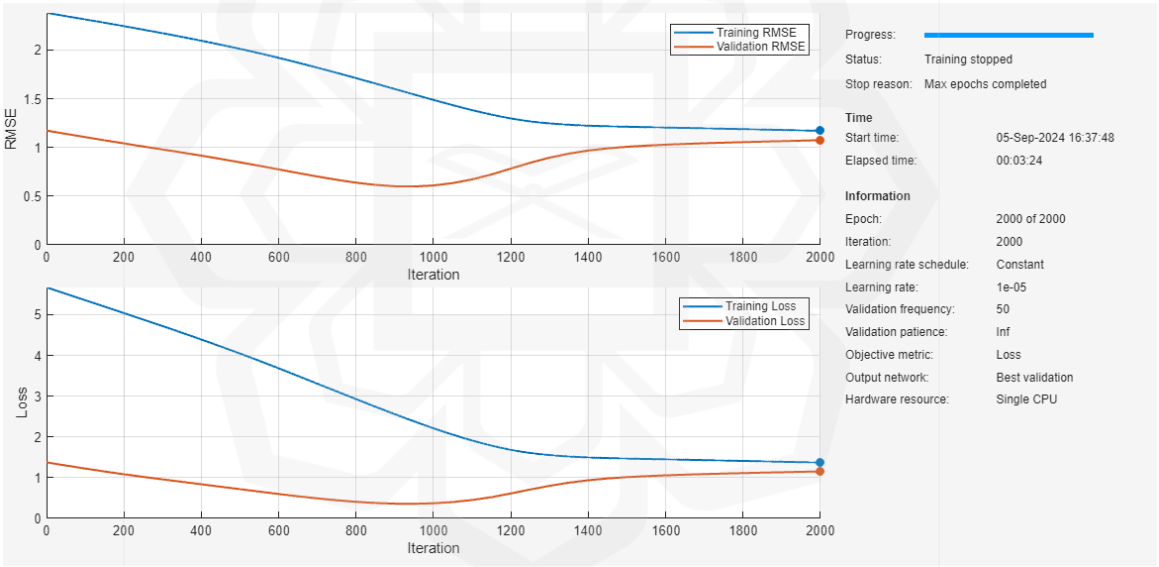
Training RMSE
Validation RMSE
RMSE
Iteration
Training Loss
Validation Loss
Loss
Iteration
Progress:
Status: Training stopped
Stop reason: Max epochs completed
Time
Start time: 05-Sep-2024 16:37:48
Elapsed time: 00:03:24
Information
Epoch: 2000 of 2000
Iteration: 2000
Learning rate schedule: Constant
Learning rate: 1e-05
Validation frequency: 50
Validation patience: Inf
Objective metric: Loss
Output network: Best validation
Hardware resource: Single CPU

(b)

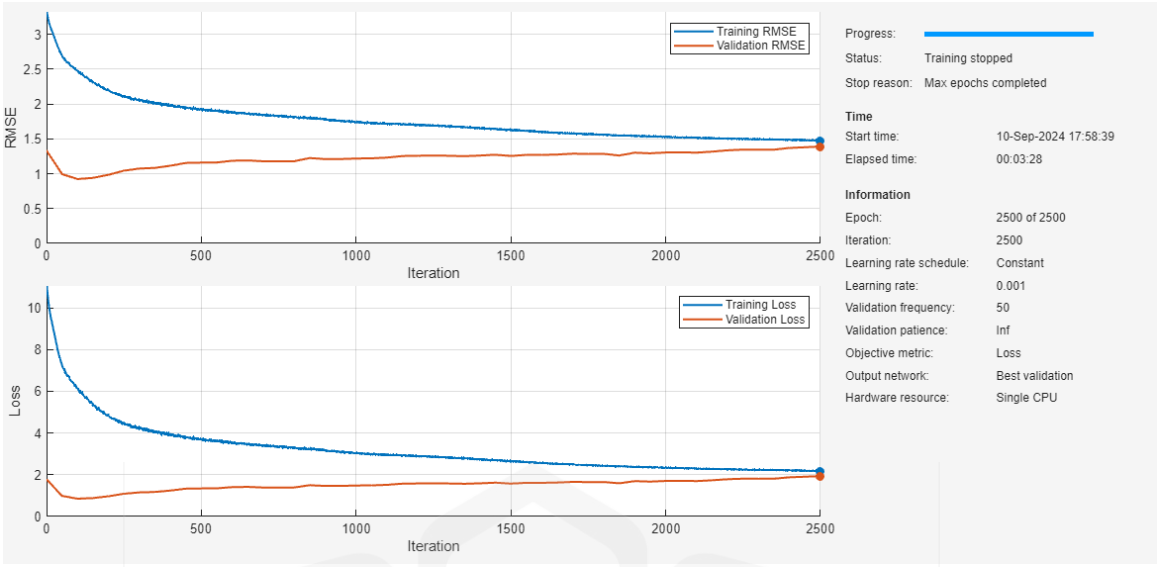

(c)

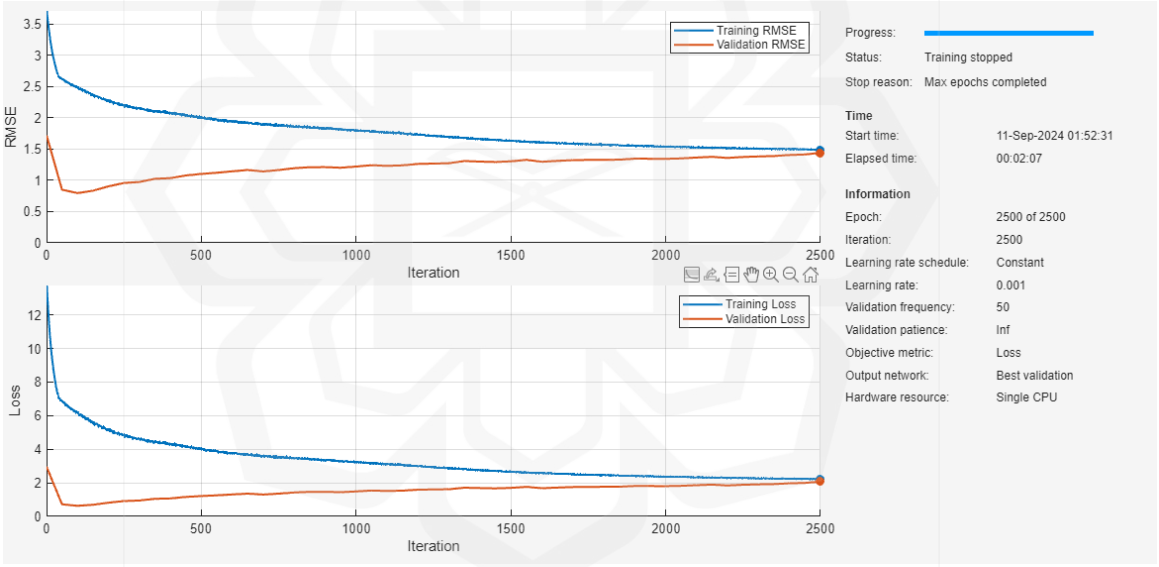

(d)

Figure 4.10 The Training and Validation RMSE and Loss at the Desired Steering Angle of (a) 5° (b) 10° (c) 15° and (d) 20°

Table 4.6 presents the minimum RMSE and loss values obtained during training and validation for each beam steering angle using the AEP-DNN method. The values demonstrate successful convergence and acceptable accuracy. RMSE is a measure used to confirm the dependability of a model examining differences between predicted and observed values. In this study, RMSE is difference between predicted and initial phases. It quantifies how closely the model's predictions align with the actual values in magnitude. Small RMSE values indicate precise predictions and a good fit for the data. Training loss assesses the performance of a machine learning model on training data. It is computed during training and used to adjust the model's parameters using methods like gradient descent to reduce loss. Validation loss evaluates the model's performance on a different dataset, the validation set, to assess generalization to unseen data and identify overfitting. When validation loss exceeds training loss, it indicates overfitting during testing network stage. The closer the minimum RMSE and loss values are to '0', the better for the convergence rate of both training and validation performances. However, RMSE values ranged from 1.3 to 1.5 is acceptable because the AEP-DNN pattern met desired main beam at 5°, 10°, 15°, and 20°.

The training loss performance of the AEP-DNN model, as shown in Table 4.6, demonstrates consistent and stable convergence across all steering angles. The loss values remain within a narrow range of 2.07 to 2.33, indicating that the network effectively minimized the error during training without significant discrepancies. This stable performance suggests that the model successfully captured the underlying relationship between the desired main beam's angle direction and the resulting predicted phases. Furthermore, the minimal difference between training and validation loss values indicates balanced learning and limited overfitting. However, the slightly higher training loss values also suggest potential for further optimization through fine-tuning of hyperparameters or network architecture to improve learning efficiency and accuracy. Additionally, the reported processing times, ranging from approximately 2 to 3.5 minutes, reflect the computational efficiency of the AEP-DNN model.

As shown in Table 4.6, the training and validation times for 10° and 15° beam steering angles are longer compared to 5° and 20°. This is because the beam patterns at 10°

and 15° are more complex and harder for the neural network to learn. At these mid-range angles, the phase values needed for each antenna element are less distinct and more sensitive to small changes, so the model takes longer to adjust and learn the correct pattern. Also, the sidelobes at these angles might vary more, making it harder for the network to achieve accurate results quickly. On the other hand, at 5° and 20°, the phase patterns are either close to uniform (near 0°) or more clearly defined (near the array's edge), so the network could learn them faster and with fewer corrections. This explains why training for 10° and 15° takes more time than for the other angles.

Table 4.6 The Minimum Value of Training and Validation RMSE and Loss

Graphs / **Desired Angle (°)**	**Processing Time (mins: secs)**	**RMSE**		**Loss**	
		Training	**Validation**	**Training**	**Validation**
5	02:02	1.50	1.33	2.26	1.77
10	03:24	1.52	1.37	2.33	1.90
15	03:28	1.47	1.39	2.17	1.93
20	02:07	1.48	1.44	2.21	2.07

4.10 COMPARISON WITH PREVIOUS WORKS

Based on the investigation of pattern synthesis using DNN, a research work conducted by Kim and Choi (2020) carried out pattern synthesis of a 1 x 4 patch antenna array at 2.4 GHz using FR4 substrate with a dielectric constant of 4.3 and a thickness of 1 mm as shown in Figure 4.11. The DNN framework comprises 5 layers, and their DNN algorithm is verified by HFSS. The authors optimized both amplitude and phase to achieve the desired main beam angle. The predicted DNN main beam pattern of 114°, falls within the desired range of 100°-140°.

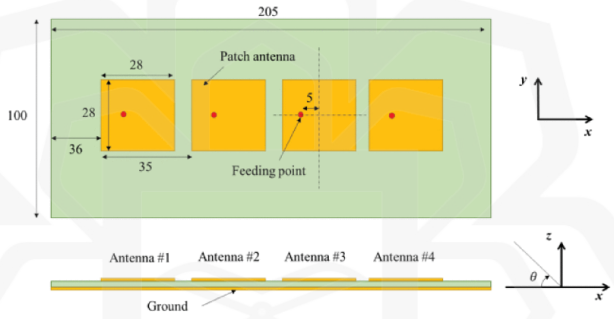

Figure 4.11 Array Antenna Structure Used for Radiation Pattern Simulations (Kim & Choi, 2020)

Additionally, a previous work conducted by Montaser and Mahmoud (2021) also carried out pattern synthesis for a dual-band circularly polarised bone-shaped patch antenna at 28 GHz and 38 GHz, consisting of 16 elements as shown in Figure 4.12. The DNN framework also includes 5 layers. The authors optimized phases to obtain the desired main beam angle and the DNN verification was performed by CST. In this work, the authors used the modified gravitational search algorithm and particle swarm optimization (MGSA-PSO) algorithm to obtain initial input phases for the DNN algorithm. The desired main beam directions investigated in this work are 40°, 142°, 205°, and 320°.

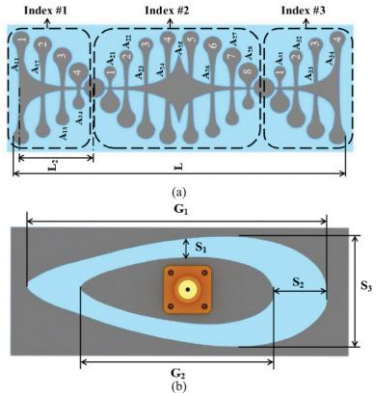

Figure 4.12 Proposed Antenna Structure (a) Top View, and (b) Back View (Montaser & Mahmoud, 2021)

Research conducted by Alam et al. (2024) investigated pattern synthesis on a 1 x 4 rectangular patch antenna array at 10 GHz through phase shift optimization as shown in Figure 4.13. The DNN framework consists of 10 layers.

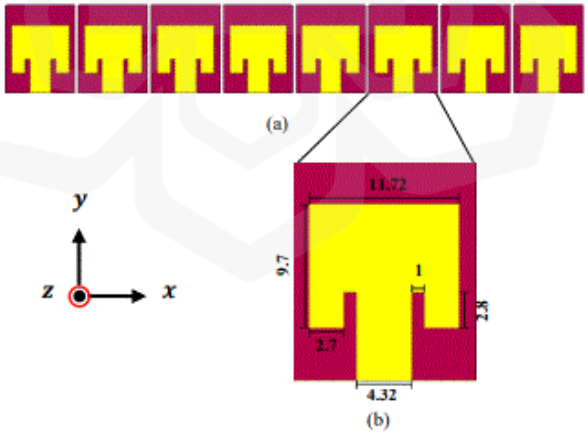

Figure 4.13 (a) AESA Antennas in CST Full-Wave Simulator, and (b) Enlarged View of Individual Antenna Elements (Alam et al., 2024)

(Kim & Choi, 2020) introduce a DNN that maps radiation patterns of a 4×1 millimeter-wave patch array to amplitude and phase excitations, using 6859 full-pattern samples to capture element coupling and achieve high-fidelity synthesis. (Montaser & Mahmoud, 2021) adopt a hybrid PSO-MGSA-enhanced DNN trained on 150 bone-shaped patch antenna geometries, validated via physical prototypes at 28 and 38 GHz, achieving side-lobe levels below –30 dB. (Alam et al., 2024) propose a novel dataset reduction approach by exploiting phase-shift redundancy in an 8-element AESA array, enabling scalable beam pattern synthesis with minimal data and fast training. Compared to these, this AEP-DNN method uniquely combines AEP, simpler architecture, and accurate beam prediction which balancing antenna design structure and computational efficiency to support advanced 5G millimeter-wave beamforming.

4.11 SUMMARY OF CHAPTER

This chapter summarizes the array pattern synthesis by using the AEP-DNN algorithm to prove the beam-steering capability of the main beam pattern of the proposed DLPAA at 28 GHz. The pattern synthesis for the proposed DLPAA has been successfully steered using the AEP-DNN method to the desired patterns of 5°, 10°, 15°, and 20°. The RMSE and loss values at the steering angles of 5°, 10°, 15°, and 20° are below than 2.3. The main beam pattern synthesis of AEP-DNN has been verified with the pattern multiplication method (PMM) and full-wave model (CST) and the results show good agreement with each other.

CHAPTER FIVE

FABRICATION AND VALIDATION

5.1 INTRODUCTION

The satisfactory simulation results from Chapter 3 need to be verified by undergoing antenna measurements. In this chapter, it discusses the fabricated antennas, the experimental setup for reflection coefficient and radiation pattern measurements, the comparison of measured results to simulated results, and a summary. The aim of this chapter is to verify the simulated results (Chapter 3) and DNN algorithm for the beam-steering capability (Chapter 4) of antennas. This aim corresponds to the third objective of this study. The measurement is carried out for antenna design 2 (substrate thickness 1.575 mm) and also for the ±45° proposed dual-polarised antenna array.

Since our fabricated antenna focuses on dual polarization slanting at ±45°, our measured antenna performance is compared with previous research that also used slanted ±45° dual-polarised antennas. Based on research work (Xia et al., 2022), the paper introduces a millimeter-wave end-fire phase antenna array designed for 5G mobile communications. The antenna achieves ±45° linear polarizations using a modified substrate integrated waveguide (SIW) slot polariser. However, the antenna has complexity in fabricating the antenna arrays for practical mobile terminal integration.

Additionally, the research work in (Zhu & Deng, 2022) also uses SIW of double layer stacked and a stepped slot to enable dual linear polarization. A resonated metallic loop and bilateral connecting lines are integrated in front of the antenna aperture. Another complex antenna structure investigated by (Jiang et al., 2023), where ±45° dual-polarised dipole element antenna forms a wideband phased antenna array. They use two orthogonal coupling feeding baluns over a dual-polarised dipole to excite the dipole's two pairs of orthogonal arms and employ four parasitic patches to realize ±45° dual-polarised antenna array. However, the other works involve a complicated antenna structure to operate at high

frequency, and this study manages to achieve a high gain antenna by using only a single layer antenna. Furthermore, the aim of this study is to achieve a directive main beam pattern of the antenna array for the implementation of beam-steering capability. The proposed antenna array has proven that the directive main beam pattern is obtained.

5.2 MEASUREMENT FLOWCHART

Figure 5.1 depicts the flowchart procedure for carrying out measurement process in order to verify the simulation results from the Chapters 3 and 4. All details of each block in Figure 5.1 would be explained in each section. The experimental validation process begins with the fabrication of the antenna based on the proposed design. Upon completion, the reflection coefficient (S_{11}) is measured using a vector network analyzer to ensure proper impedance matching and confirm that the antenna operates within the desired frequency band.

Subsequently, the radiation pattern is measured to evaluate the antenna's beam direction, gain, and side lobe characteristics. These measured results are then used to verify the accuracy of the proposed Active Element Pattern (AEP) approach by comparing the actual beam direction with the predicted values. If the measured performance does not meet the expected criteria, adjustments are made and the verification process is repeated. Once the predicted and measured results are in agreement, the experimental validation is considered complete.

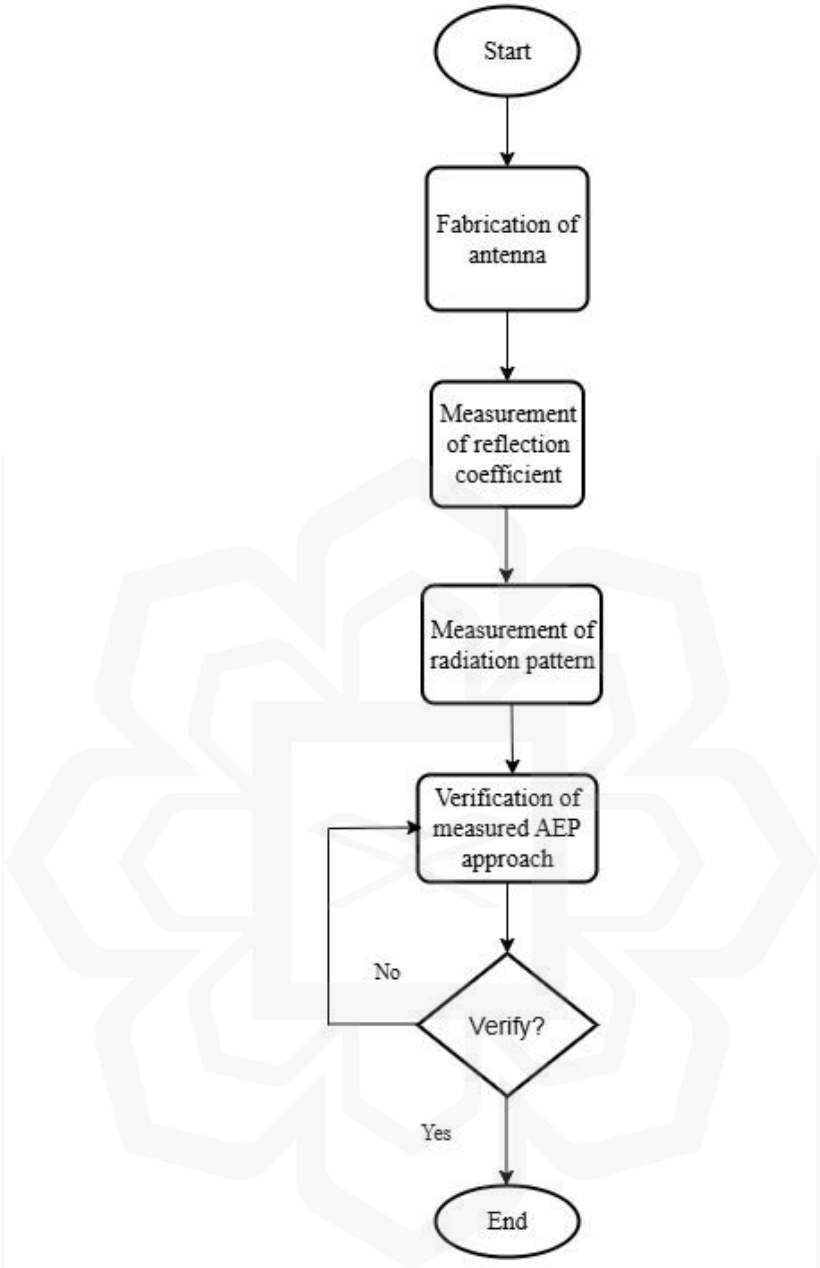

Figure 5.1 Flowchart of Measurement

5.3 FABRICATION AND MEASUREMENT

The antennas are fabricated to measure and verify their simulation performance. The antenna is fabricated by an industry company as the etching process for the antenna at high frequency is challenging. This is due to the small size of the transmission feedline, where even the smallest mistake could cause a short-circuited antenna. Initially, the first step of manual fabrication process, which is PCB cutting process is carried out using an automatic program machine and *IsoCam* software. However, the feeding line's dimensions are so small that high cutting accuracy is required. The drilling process has been repeated several times because the feeding line's dimensions are inaccurate after cutting. Therefore, the researcher decided to send the antenna design to an industrial company with high accuracy machine for antenna etching. Once the antennas are fabricated, they are further investigated by measuring the S-parameters, and radiation pattern. The drilling process for the SMA connector is done at the Antenna Lab, Kulliyyah of Engineering, IIUM.

A drilling machine is necessary for placing connectors on the input ports of the antenna as shown in Figure 5.2. A 2 mm drill diameter is used because the screw connector diameter is also 2 mm. After completing the drilling operation, the SMA connectors are placed on the fabricated antennas.

Figure 5.2 The Drilling Machine

Figures 5.3 and 5.4 show the fabricated antennas at substrate thicknesses of 0.254 mm (antenna design 1) and 1.575 mm (antenna design 2), respectively. Figure 5.5 shows the fabricated proposed ±45° dual-polarised antenna array using the modified T-power divider (substrate thickness 1.575 mm).

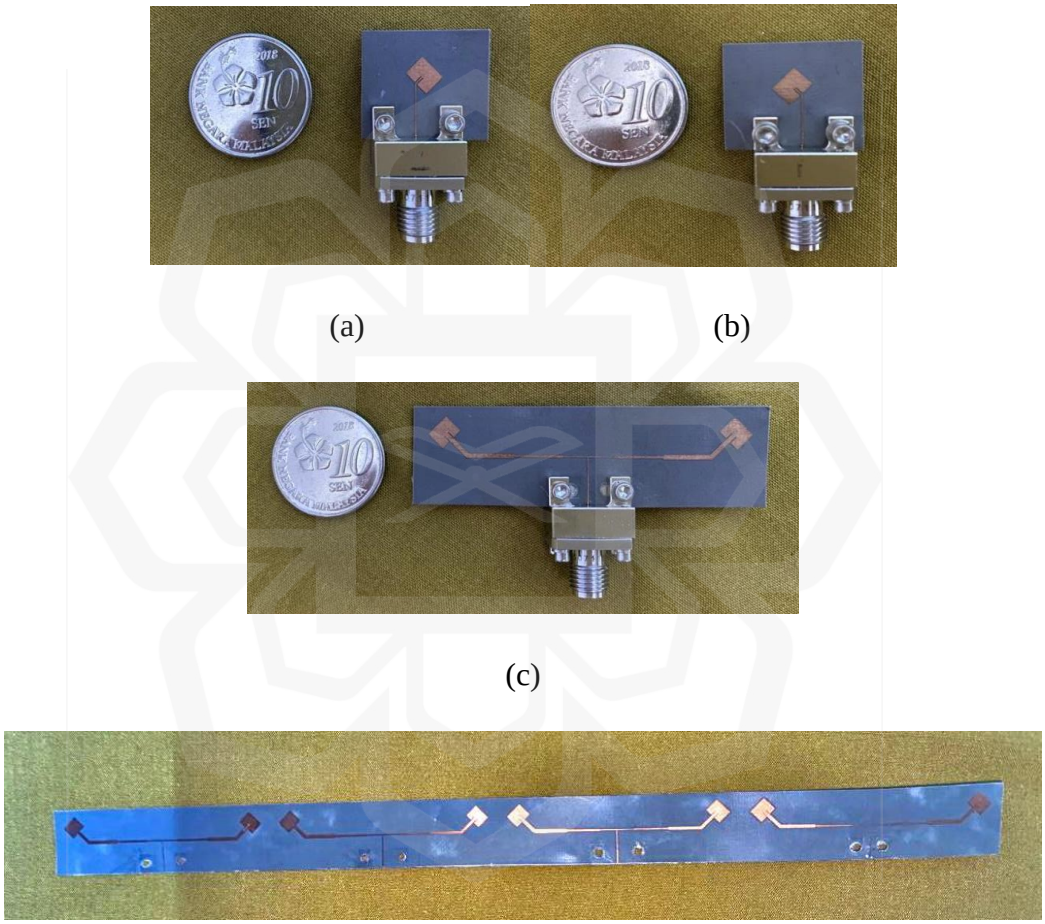

(a) (b)

(c)

(d)

Figure 5.3 The Fabricated Slanted (a) +45° (b) -45° Single Antennas (c) ±45° Dual-Polarised Antenna and (d) 1 x 4 ±45° Dual-Polarised Antenna Array (Antenna Design 1)

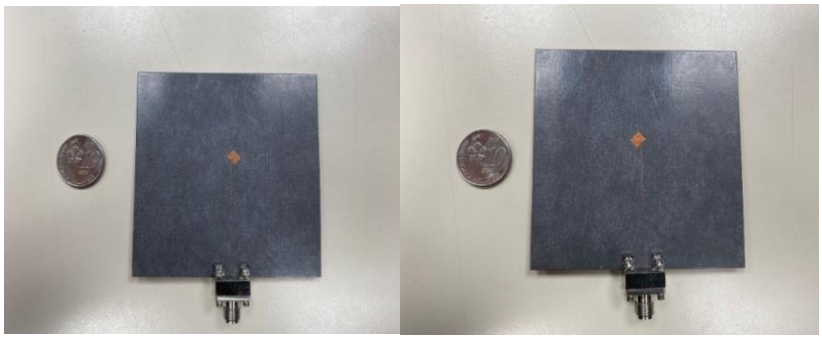

(a) (b)

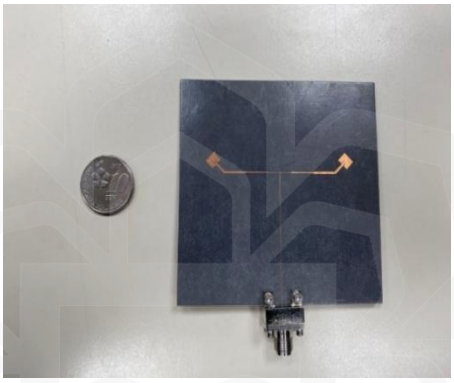

(c)

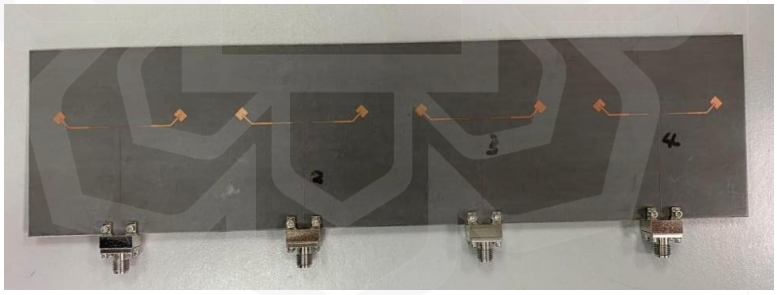

(d)

Figure 5.4 The Fabricated Slanted (a) +45° (b) -45° Single Antennas (c) ±45° Dual-Polarised Antenna and (d) 1 x 4 ±45° Dual-Polarised Antenna Array (Antenna Design 2)

Figure 5.5 The Fabricated Proposed 1 x 4 ±45° Dual-Polarised Antenna Array (Substrate Thickness of 1.575 mm)

The inter-element spacing was equal to 15.60 mm (2.159 λ). In this study, controlling sidelobe levels of dual-polarised antennas at millimeter-wave frequencies is a challenging task. Therefore, the average sidelobe level of the proposed antenna array would be around -5 dB. The ideal value of inter-element spacing should be approximately 0.5 λ to 0.7 λ to avoid high sidelobe levels and mutual coupling. It is the smallest distance that could be applied to the antenna as the dimension of the SMA connector limits the spacing between ports. Despite this, the main beam pattern remains unaffected, and the aim of this study is to steer the main beam to a desired location, not to reduce sidelobe levels.

All antennas are measured except for the antennas at substrate thickness 0.254 mm. It is because the fabricated antenna at 0.254 mm is extremely thin which could easily cause the antenna to bend. The effect on antenna bending is that it could change the ability to radiate at the desired frequency and the signal would be worse. Therefore, only the fabricated antenna design 2 and the proposed antenna array (substrate thickness 1.575 mm) are measured. Prior to measuring the radiation pattern of the antenna, the researcher needs to measure the reflection coefficient (S_{11}) of the antenna to indicate that the amount of reflected received power is less than -10 dB to ensure that the received power is effectively delivered to the antenna for transmitting signals. The mutual coupling of the antenna arrays is also measured. Therefore, the vector network analyzer (VNA) at the Antenna Laboratory, Chang Gung University is used to measure the S_{11} performance for single ±45°, and a dual-polarised antenna. The S_{11} of 1 x 4 antenna array and the proposed 1 x 4 antenna array is

measured at the Antenna Lab of MJIIT UTM KL. The radiation pattern of the single antennas and the dual-polarised antenna is measured at the Antenna Laboratory, Chang Gung University, by using the over-the-air (OTA) measurement chamber. Meanwhile, the radiation pattern of antenna arrays is measured at the RF Station in Petaling Jaya, by using the compact-antenna-test-range (CATR) measurement. The obtained measured S_{11} is compared to the simulated S_{11}.

5.4 EXPERIMENTAL SETUP FOR S-PARAMETER MEASUREMENT

5.4.1 Calibration Procedures

Measurement of S_{11} and mutual coupling is carried out using VNA, and the calibration of VNA is done using a common approach called SOL (Short, Open, and Load). The calibration kit is provided by the facility. VNA calibration aims to remove systematic errors from the instrument hardware and consider the presence of any factors that might have been added to enable specific measurements at the required frequencies. SOL involves 3 loads placed at the end of the VNA's port cables. The Open and Short loads result in total reflection with 180° phase differences. The 50 Ω load provides a no-reflection situation. The data at each frequency point is processed through a simple algorithm to calibrate the measured data with the antenna under test (AUT).

5.4.2 Measurement Setup

The actual antenna measurement is installed in the system after the calibration setup is completed. The measurement setup is similar to the calibration setup excepts for:

1. The female adapter is interconnected to the port cable 1 and to the port of the antenna.
2. S_{11} measurement requires one connected cable port and mutual coupling measurement requires two connected cable ports.
3. The range of frequencies 27 GHz – 29 GHz is selected.
4. Measurements of S_{11} and mutual coupling of the antenna are carried out.

5.4.3 Measurement Results

In order to verify the simulation results, the measured S-parameters, bandwidth and radiation pattern are obtained. The S-parameter includes the reflection coefficient (S_{11}) and mutual coupling.

5.4.3.1 Reflection Coefficient and Bandwidth

The measured and simulated S_{11} for each antenna are shown in Figures 5.6, 5.7, 5.8 and 5.9. For the single antennas, the dual-polarised antenna, and the dual-polarised antenna array, the raw measured data S_{11} is given in complex numbers format. Hence, it is necessary to find its magnitude in decibels (dB) by using the formula in Equations 5.1 and 5.2. For the proposed antenna array, the raw measured data S_{11} is given in magnitude format in dB, therefore, it would not require any conversion. The measured data S_{11} is in the range of 27 GHz to 29 GHz with an interval of 0.01 GHz, thus, the simulated data S_{11} should have the same data intervals as the measured ones for comparative analysis. The simulated data S_{11} is averaged at each 0.01 GHz interval from their original value. The total number of measured and simulated data S_{11} is 200 from 27 GHz to 29 GHz with an interval of 0.01 GHz.

$$k = \sqrt{Re^2 + Im^2} \tag{5.1}$$

$$magnitude\ (dB) = 20 * log(k) \tag{5.2}$$

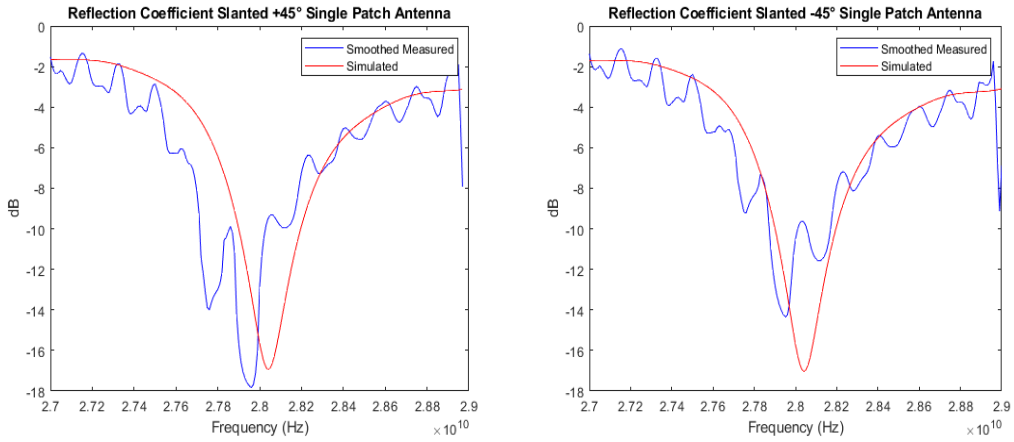

Figure 5.6 The Simulated and Measured S_{11} of Single Antennas

Based on Figure 5.6, the measured S_{11} shows ripple signals. This might be possibly due to measurement errors caused by equipment such as a coaxial connector. Therefore, the measured data undergo a smoothing process, which is a signal processing technique typically used to remove noise from signals using the *OriginLab* tool. The simulated S_{11} at 28 GHz for both single antennas are similar to each other, approximately -15.60 dB and -15.50 dB, while the measured S_{11} at 28 GHz for both single antennas are -12.85 dB and -10.50 dB, respectively. The minimum simulated S_{11} for both single antennas are -16.94 dB and -17.04 dB at 28.04 GHz. The minimum measured S_{11} for both single antennas are -17.82 dB at 27.96 GHz and -14.34 dB at 27.95 GHz. The difference between simulated S_{11} and measured S_{11} is acceptable due to the ripple errors. The minimum point of measured S_{11} is shifted downwards from the resonant frequency with a difference of 0.04 and 0.05 GHz, which is relatively low and these are an acceptable measurement results performance and quite agree with simulated ones. The small discrepancies between the simulated and measured ones might be possibly caused by several factors such as measurement and fabrication errors. The bandwidth of simulated data for both single antennas is 0.29 GHz and 0.20 GHz. The bandwidth of measured data for both single antennas is 0.30 GHz and 0.29 GHz, respectively.

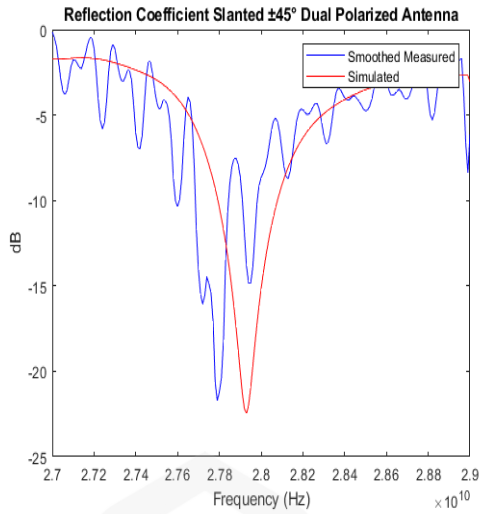

Figure 5.7 The Simulated and Measured S_{11} of ±45° Dual-Polarised Antenna

As shown in Figure 5.7, the measured S_{11} is also has ripple signals. It might possibly be due to measurement errors caused by equipment such as a coaxial connector. Therefore, the measured data also undergo a smoothing process using the *OriginLab* tool. The simulated and measured S_{11} at 28 GHz are -15.50 dB and -8.65 dB, respectively. The minimum simulated and measured S_{11} are -22.50 dB at 27.93 GHz and -21.72 dB at 27.79 GHz. The difference between simulated S_{11} and measured S_{11} is acceptable due to the ripple errors. The minimum point of the measured S_{11} is shifted downwards from the resonant frequency with a difference of 0.21 GHz. These measurement results are in agreement with the simulated ones, and the small discrepancies between the simulated and measured ones might also possibly be caused by several factors such as measurement and fabrication errors. The bandwidth of the simulated and measured data is 0.29 GHz and 0.15 GHz respectively.

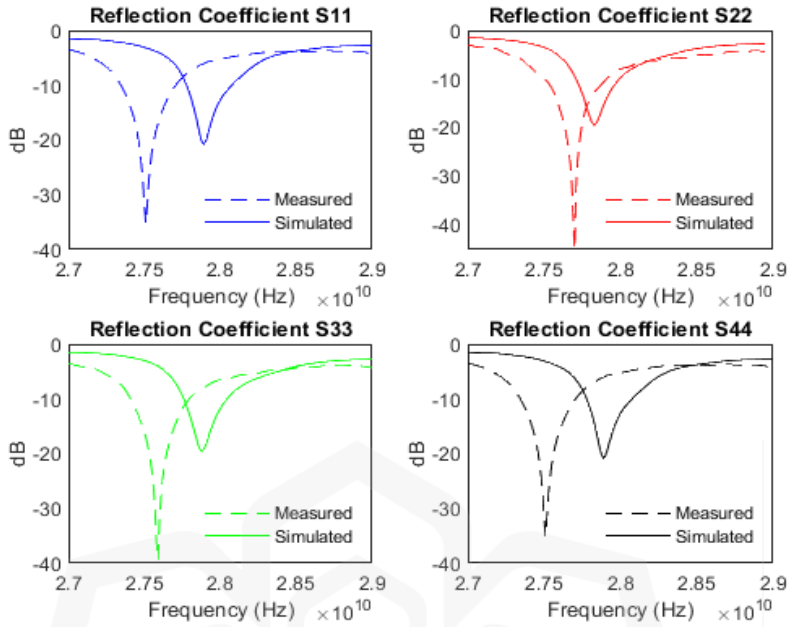

Figure 5.8 The Simulated and Measured S_{11} of ±45° Dual-Polarised Antenna Array

As shown in Figure 5.8, the simulated S_{11} at 28 GHz for port 1, port 2, port 3, and port 4 are -12.85 dB, -11.94 dB, -11.90 dB, and -12.87 dB. The measured S_{11} at 28 GHz for port 1, port 2, port 3, and port 4 are -5.27 dB, -7.96 dB, -6.54 dB, and -5.25 dB. The minimum simulated S_{11} at port 1, port 2, port 3, and port 4 are -20.77 dB (27.89 GHz), -19.55 dB (27.83 GHz), -19.55 dB (27.88 GHz), and -20.77 dB (27.89 GHz). The simulated S_{11} at port 1 and 5 are similar to each other, as are those at port 2 and 3. The minimum measured S_{11} at port 1, port 2, port 3, and port 4 are -35.28 dB (27.51 GHz), -45.26 dB (27.70 GHz), -39.50 dB (27.59 GHz), and -35.06 dB (27.51 GHz). The measured S_{11} shows good performance, however, the frequency is shifted downwards ranging between 27.51 GHz to 27.70 GHz. A slight difference between the shifted frequencies and 28 GHz might possibly be due to fabrication errors. In addition, as the resonance frequency is at millimeter-waves (28 GHz), any small shift or fabrication tolerance might lead to large errors.

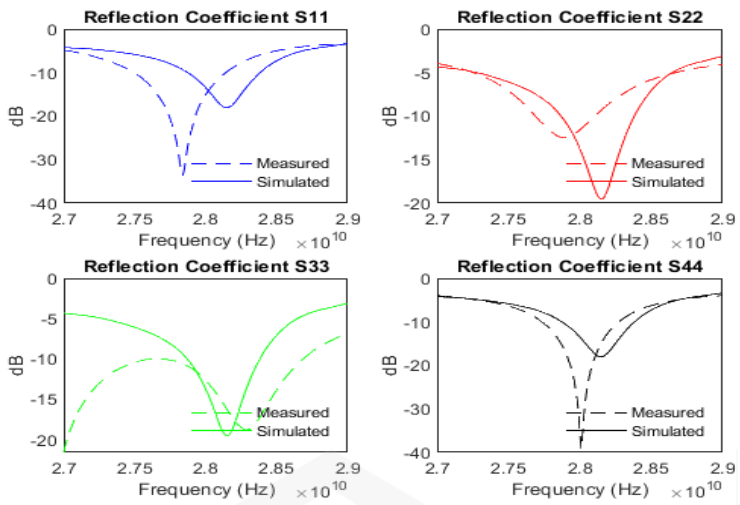

Figure 5.9 The Simulated and Measured S_{11} of ±45° Dual-Polarised Proposed Antenna Array

As shown in Figure 5.9, the simulated S_{11} at 28 GHz for port 1, port 2, port 3, and port 4 is -13.44 dB, -13.66 dB, -13.67 dB, and -13.43 dB. The measured S_{11} at 28 GHz for port 1, port 2, port 3, and port 4 is -15.05 dB, -11.57 dB, -12.69 dB, and -35.23 dB. The minimum simulated S_{11} at port 1, port 2, port 3, and port 4 is -18.05 dB (28.15 GHz), -19.56 (28.15 GHz), -19.54 dB (28.15 GHz), and -18.05 dB (28.15 GHz). The simulated S_{11} at port 1 and 4 are similar to each other, as are port 2 and 3. The minimum measured S_{11} at port 1, port 2, port 3, and port 4 are -33.53 dB (27.84 GHz), -12.50 dB (27.89 GHz), -21.60 dB (27.00 GHz), and -39.11 dB (28.01 GHz). Both the simulated and the measured S_{11} show good performance, however, the frequency is shifted upwards at 28.15 GHz for the simulated S_{11} and shifted downwards and upwards within the range 27.00 GHz to 28.01 GHz for the measured S_{11}. A slight difference between the shifted frequencies and the desired resonant frequency of 28 GHz might possibly be due to fabrication errors. At high frequencies like 28 GHz, even slight misalignment of the connector, minor differences in patch or substrate size, or uneven soldering could affect the antenna's performance. These small changes could shift the resonant frequency or create unwanted signal reflections, leading to higher return loss. As an example, at port 2, such issues might have disrupted the feed connection, resulting in poorer matching compared to the other ports.

5.4.3.2 Mutual Coupling

The measured and simulated mutual coupling for the antenna array and the proposed antenna array are shown in Figure 5.10 and 5.11. As mentioned before in Chapter 3, the inter-element spacing of both antennas are 70 mm (9.69 λ), and 15.60 mm (2.159 λ). The raw measured data for the dual-polarised antenna array is given in complex number format, hence, it is necessary to find its magnitude in decibels (dB) by using the formula in Equations 5.1 and 5.2. The raw measured data for the proposed dual-polarised antenna array is given in magnitude format in dB, hence it would not require any conversion. The measured data is in the range of 27 GHz to 29 GHz with an interval of 0.01 GHz, therefore, the simulated data should have the same data intervals as measured ones for comparative analysis. The simulated data is averaged at each 0.01 GHz interval from their original value. The total number of measured and simulated data S_{11} is 200 from 27 GHz to 29 GHz with an interval of 0.01 GHz.

Due to the uniform inter-element spacings, the mutual coupling between two adjacent ports is approximately the same. The mutual coupling between the two adjacent ports of the proposed antenna array could not be measured because the size of the two coaxial connectors of VNA are larger than the distance between two ports of antenna array. Based on Figures 5.10 and 5.11, the simulated and measured mutual coupling of the antenna arrays show good performance with less than -20 dB. Also, the mutual coupling between adjacent port elements has much higher mutual coupling value compared to non-adjacent port elements. It shows that the nearer port elements would cause higher electromagnetic signal's interaction between them that fluctuates the mutual coupling value.

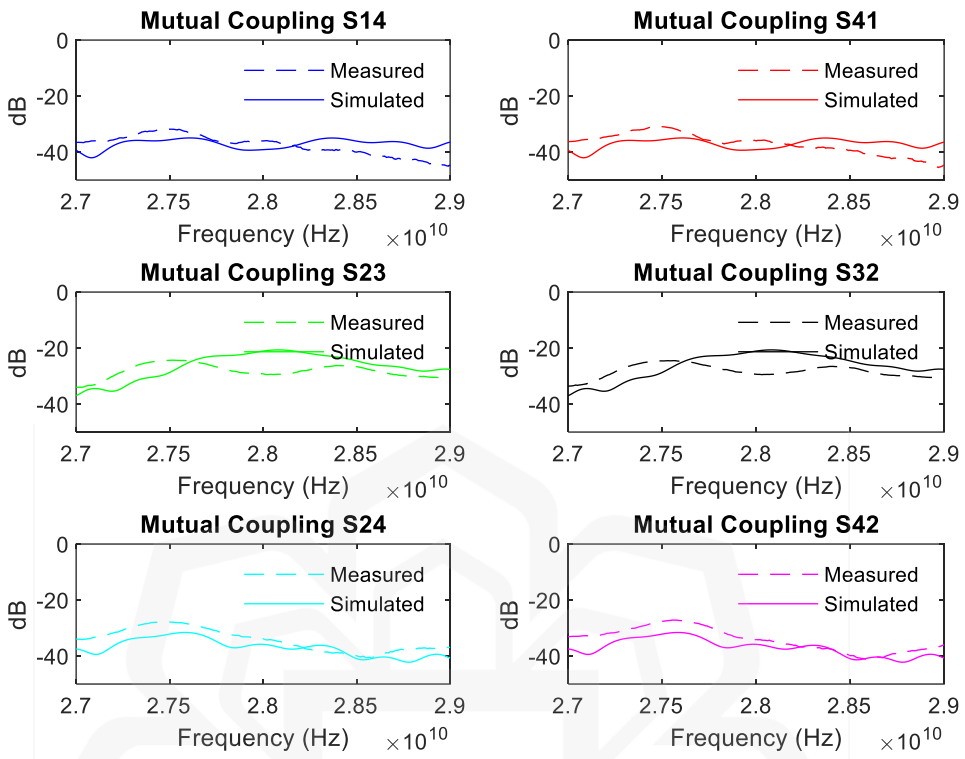

Figure 5.10 The Mutual Coupling of the ±45° Dual-Polarised Antenna Array

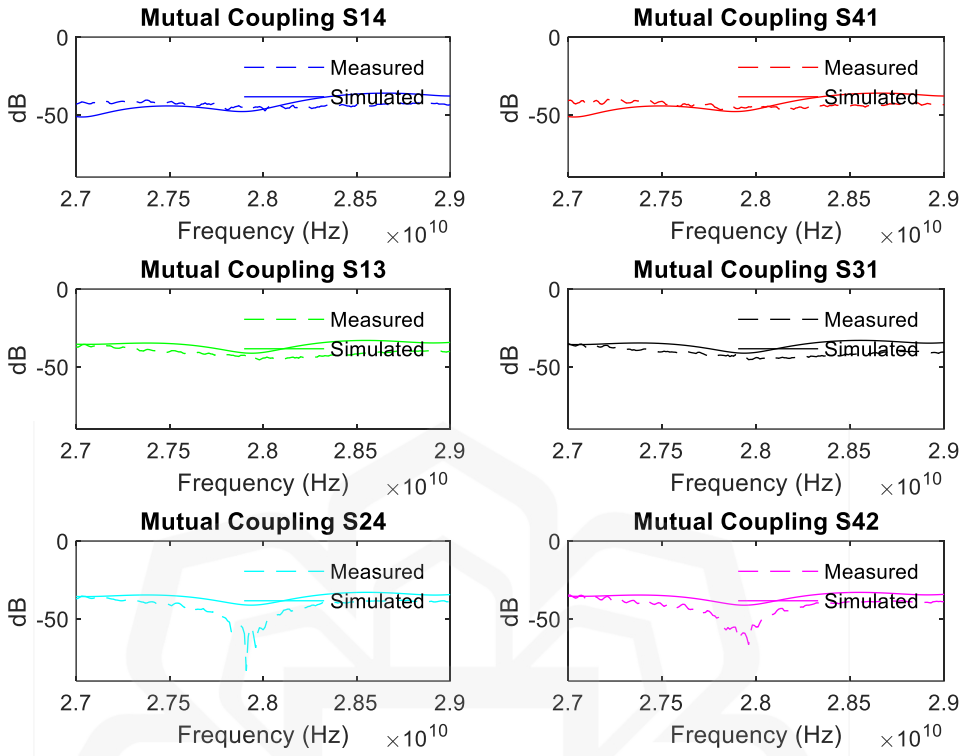

Figure 5.11 The Mutual Coupling of the Proposed ±45° Dual-Polarised Antenna Array

5.5 EXPERIMENTAL SETUP FOR RADIATION PATTERN MEASUREMENT

The radiation pattern is a graphical representation of the field magnitude at a fixed distance from the antenna as a function of direction (angle). In this study, realized gain is used as the indicator of how much the antenna concentrates its energy in one direction. Realized gain is usually lower than gain due to taking into account impedance mismatch.

5.5.1 Radiation Pattern of Single Antennas and Dual-polarised Antenna Measurement

Before proceeding to the antenna pattern measurement, the researcher needs to identify the polarization of the antenna from the CST simulation tool for comparative analysis. The radiating patch elements are slanted at ±45°, the polarization setting is set to be "linear" as the radiating signals propagate in a linear direction at an angle of 45° to the normal plane. The 'vertical' realized gain indicates the co-polarization signals and the 'horizontal' realized gain indicates the cross-polarization signals.

During radiation pattern measurement setup for the single antennas and the dual-polarised antenna, the antenna under test (AUT) is placed on top of the antenna holder parallel to 0°. Therefore, to attain both co- and cross-polarization of electric and magnetic fields, *E*- and *H*-plane, respectively, the antenna settings ought to be checked properly. Therefore, a complete radiation pattern measurement should include the polarization properties, which are often accomplished by making pattern cuts in the co-polarised and cross-polarised *E*- and *H*-planes of the AUT. An example of antenna measurement setup for each *E*- and *H*-planes of both co-polarised and cross-polarised of +45° single antenna is shown in Appendix E. Similar measurement setup is also applied to the -45° single antenna and the dual-polarised antenna (combination +45° and -45° single elements). The *E*-plane is measured when the AUT input port is placed parallel to the holder cable meanwhile, the *H*-plane AUT input port is placed perpendicular to the holder cable. The co- and cross-polarization signals are determined by placing the horn antenna (the transmitter) in the same or different polarization to the AUT. The transmitter horn antenna would only rotate 180° to measure the front antenna pattern.

5.5.1.1 Hardware Components

Figure 5.12 shows an illustration of hardware components installed for the measurement setup of single +45°, single -45°, and the ±45° dual-polarised antenna. The horn antenna is used as the standard transmitter antenna shown in Appendix E and the AUT is used as the transmitting antenna in the setup. The AUT is placed on top of the antenna holder as shown in Appendix E. The radio frequency (RF) signal generators (E8257DSG) as shown in Appendix E are used for generating the signals and feeding the signal of the desired frequency and power to the transmitter. The AUT is rotated in azimuth and elevation cut plane and is received by the receiver.

The entire antenna setup is placed in a location where walls are covered with absorbing material, an RF microwave absorber pyramidal foam cones or high-performance polypropylene hybrid material as shown in Appendix E. This would allow AUT testing free from any building structure and would have testing as if the antenna is placed in an unbounded free space medium.

The mixer (11970A) as shown in Appendix E is used as it is a critical component in the instrumentation of antenna measurements, especially for high frequencies. It converts RF power signal at one frequency into another frequency to down-convert the signal into lower frequencies (28 GHz) from the original setup frequency (~60 GHz), and it is also used to make signal processing easier and less expensive.

E5071C Network Analyzer is used to perform the calibration measurements as shown in Appendix E. To ensure that all the connected devices in the setup are appropriately synchronized, the reference output of 10 MHz is set. The computer is connected to the devices for the data to be the transferred to and collected as shown in Appendix E. The collected data of pattern measurement is in normalized form. The single antennas and dual-polarised antenna measurement setup comprise the main hardware components as shown in Appendix E.

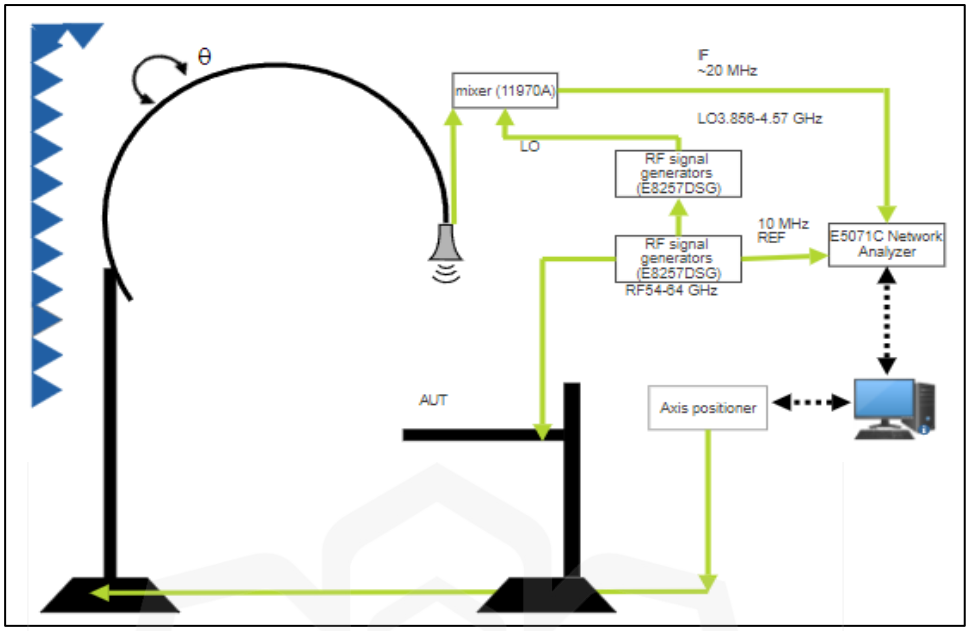

Figure 5.12 The Measurement Setup Diagram

5.5.1.2 Calibration Procedures

Prior to antenna pattern measurement, calibrating the measurement setup is necessary to ensure that the other factors that might affect the measurement are minimized, as examples, factors such as range-length loss, reference antenna gain, cable losses, and others. The calibration is done using a reference antenna, in this study, a standard gain horn antenna (for 28 GHz operating frequency). The reference horn antenna is placed at the center of the antenna holder as the AUT and adjusted to be at bore-sight level with the receive antenna. The objective of the calibration is to ensure that a single input signal delivered to the system arrives with equal magnitude and phase at each antenna port.

If the antenna and source cable are ideally matched, all power provided to the antenna would radiate, according to the Friis transmission equation formula. However, the most typical scenario is that source and antenna impedance mismatch results in a portion of the energy being reflected back to the source, meaning that the net power transmitted is

the difference between the applied forward incident power and the power reflected to the source.

Furthermore, since measuring the system's absolute gain is not necessary, only the equalization of the relative discrepancies between transmitter and receiver ought to be accomplished, and calibration could be carried out using a regular VNA S-parameter without the addition of a vector mixer.

The calibration measurement setup should be carried out with all wires connected, and the calibration and antenna pattern measurements should both be performed using the same configuration. The total measurement uncertainty would grow if independent calibrations are performed on each component of the system. When possible, it is best to calibrate the system as a whole. Additionally, if any component is altered or destroyed, the calibration process ought to be restarted. This happened during the second trial of antenna measurement where the VNA did not detect any gain value and the graph was merely flat. We had detected a broken wire that connected to the signal generator hence, the new cable was replaced, and the entire system was recalibrated prior to the actual measurement.

5.5.1.3 Measurement Setup

The actual antenna measurement is installed in the system after the calibration setup is completed. The measurement setup is similar to the calibration setup except for:

1. The AUT is placed on top of the antenna holder and the transmit power is connected to the antenna.
2. Port 2 of the VNA is connected to the measurement antenna of the setup.
3. The down-mixer is placed on top of the transmitter horn antenna to lower the frequency range.
4. Measurement signals are transmitted between the transmitter and receiver antenna.

The obtained measurement results would be compared to the simulation results for verification purposes. If the simulation and measurement results match, the proposed dual linearly polarised antenna array would be further investigated for the beam-steering capabilities.

5.5.2 Radiation Pattern of Dual-polarised Antenna Arrays Measurement

The antenna array pattern measurement is carried out using the built-in CATR system. Due to the multiple number of input ports for these antenna arrays, the system tools that could measure the radiation pattern of multiple input ports (antenna array) are available only at a few locations, with one of them being at the RF Station company located in Petaling Jaya as shown in Appendix E. The CATR system has a compact range reflector which enables the system to measure up to 110 GHz with an excellent quiet zone at nearer far-field distance. It is most suitable for 5G measurements, especially in millimeter-wave (24 GHz up to 110 GHz) where the path loss is too high for standard far-field measurement.

The calibration setup is already set up by the company. The antenna array with 4 input ports is connected to the beamformer through external connectors at each port. The connected antenna array is then placed parallel to the normal plane on top of a sturdy polystyrene stand holder, facing the parabolic antenna as shown in Appendix E. Once the antenna setting is done correctly, the pattern measurement is ready to be carried out. The antenna holder would rotate 360° horizontally to obtain the radiation pattern of the antenna. However, this measurement system is limited to the azimuth pattern measurement only. Figure 5.13 displays the CATR R2 system architecture.

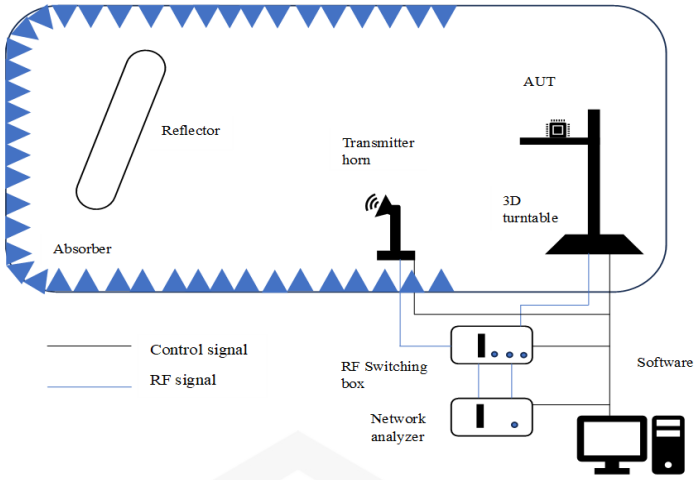

Figure 5.13 The CATR Architecture System

5.5.3 Measurement Results

The measurement of far-field radiation patterns of the fabricated antennas was performed in the OTA and CATR measurement setup. The measured pattern data of the single antennas and the dual-polarised antenna are measured in the angular range of 0° to 180° instead of 360° as it is due to the limitation of the CATR. The horn antenna stand rotates only 180°, measuring the radiation pattern of the front antenna. Therefore, the measured and simulated data for the single antennas and the dual-polarised antenna are compared in terms of their front lobe of radiation pattern only.

The single antennas and the dual-polarised antenna pattern are measured at both co-polarization and cross-polarization signals of elevation (*E*-plane) and azimuth (*H*-plane). In the simulation, the *E*-plane cut is at the cut angle phi 90° (*xz*-plane) and the *H*-plane cut is at the cut angle 180° (*yz*-plane). The antenna gain's performance relies heavily on the co-polarised signal as it is the desired polarization and maximizes signal strength while

minimizing interference. The cross-polarised signal, on the other hand, plays a different role.

During the antenna pattern measurement of the single antennas and dual-polarised antenna, a mixer is used to convert the operating frequency to the desired frequency. Thus, the received power, P_r of AUT is displayed on the computer at the angle, θ =0°. The measured absolute realized gain in decibels is calculated using the Friis transmission formula shown in the Equation 5.3 (Stutzman & Thiele, 2012) and (Hogg, 1993):

$$G_r = P_r - P_t - G_t \tag{5.3}$$

The received gain, G_r (dBi) is obtained by subtracting the transmitted power, P_t, and the transmitter gain, G_t from the received power, P_r. P_r and G_r are the power and gain of the receiver antenna (AUT). P_t and G_t are the power and gain of the transmitter horn, which are 14 dB and -24.1 dB. The first measured data (θ = 180°) acquired at the computer is the P_r at the default setting of low frequency (0.15 GHz), and that is the reason why those values needed to be converted into values at 28 GHz by scaling it to the obtained P_r (θ=0°). Next, the measured pattern data is calculated by inserting these new values (P_r) at 28 GHz into Equation 5.3 and subtracting the transmitted power and gain of the horn antenna. Table 5.1 shows the received power, P_r (θ=0°) at 28 GHz for each antenna at respective co-polarised and cross-polarised of elevation and azimuth pattern, simultaneously. Table 5.2 shows the absolute realized gain value at each antenna.

Table 5.1 The Received Power, *Pr* (θ=0°) of the Antenna at 28 GHz

Radiation Pattern / Antenna	**Co-pol Elevation (dBm)**	**Cross-pol Elevation (dBm)**	**Co-pol Azimuth (dBm)**	**Cross-pol Azimuth (dBm)**
+45° single	-16.00	-13.40	-18.70	-15.20
-45° single	-15.80	-16.40	-10.80	-15.40
Dual-polarised	-2.20	-17.50	-13.30	-2.80

Table 5.2 The Absolute Peak Realized Gain

Radiation Pattern / Antenna	**Co-pol Elevation (dB)**	**Cross-pol Elevation (dB)**	**Co-pol Azimuth (dB)**	**Cross-pol Azimuth (dB)**
+45° single	6.82	3.65	4.96	8.42
-45° single	4.37	7.84	3.83	4.26
Dual-polarised	8.78	12.25	11.16	13.84

Based on Table 5.2, for +45° single antenna, the peak realized gain of co-polarization in the *E*-plane is 6.82 dBi higher than the cross-polarised gain. However, the peak realized gain of co-polarization in the *H*-plane is 4.96 dBi. Meanwhile, for -45° single antenna, both peak realized gain of co-polarization in the *E*-plane and *H*-plane are 4.37 dBi and 3.83 dBi lower than the cross-polarised gain. The single antennas pattern performance as shown in Figures 5.14 and 5.15, indicates that the sidelobe levels for both elevation and

azimuth patterns are of interest compared to the main lobes. The single antennas exhibit a fan-shaped beam pattern. Despite this, the peak realized gain at co-polarization signals pattern is quite high.

For the ±45° dual-polarised antenna, the peak realized gain of co-polarization in the *E*-plane and *H*-plane is 8.78 dBi and 11.16 dBi lower than the cross-polarised gain. The dual-polarised antenna pattern's performance as shown in Figure 5.16, reveals that the sidelobe levels for both elevation and azimuth patterns are of interest compared to the main lobes. The cross-polarised patterns also surpass the co-polarised patterns due to the symmetric property of the slanted ±45° patch elements antenna (Lv et al., 2021) and (Zeng et al., 2015). The antenna displays a fan-shaped beam pattern, and the peak realized gain at co-polarization signals pattern is considered significant. Human errors during antenna pattern measurement setup could influence the shape of the antenna pattern. Even a slight tilt in the angle of AUT position on top of the antenna's holder would impact the antenna pattern and its peak gain. The best achieved peak gain of the dual-polarised antenna at co-polarization signals is much higher than those of single antennas. The dual-polarised antenna is further investigated by configuring it into an array with a linear arrangement of 1 x 4 (four source ports).

Contrary to the antenna arrays, the measured pattern data covers an angular range of 0° to 360° horizontally at phi=0°. Therefore, the measured and simulated data for the antenna arrays are compared in terms of the full lobe of the radiation pattern, which includes front, and back patterns. The array pattern is measured by exciting sources at each port simultaneously with default settings of amplitude 1 and phase 0 using a beamformer. Additionally, the antenna arrays pattern could only be measured in absolute pattern, which combines co-polarization and cross-polarization signals of the azimuth pattern (*H*-plane).

It is necessary to have normalized simulated pattern data for the comparative analysis. The original simulated pattern data is extracted in realized gain value of angular range 360° with intervals of 1° in Excel format. The data is normalized by using Equation 5.4. A normalized pattern is useful when the sidelobe levels and the depth of the nulls are of interest since it is easier to read their respective levels. However, normalization would not change the behavior or shape of that field pattern. These patterns are expressed in dB

with scalar value of 1 corresponding to the peak gain. The simulated pattern data for the antenna arrays are extracted by setting the amplitude to 1 and phase to 0°. The simultaneously ports source excitation is chosen. The simulated and measured pattern data are then compared to each other at desired operating frequency 28 GHz as shown in Figure 5.14 to 5.18. Since the raw data has both positive and negative values, the data is normalized by using Equation 5.4. A is the normalized value and x is the raw data.

$$A = \frac{x + \min(x)}{\max(x + \min(x))} \tag{5.4}$$

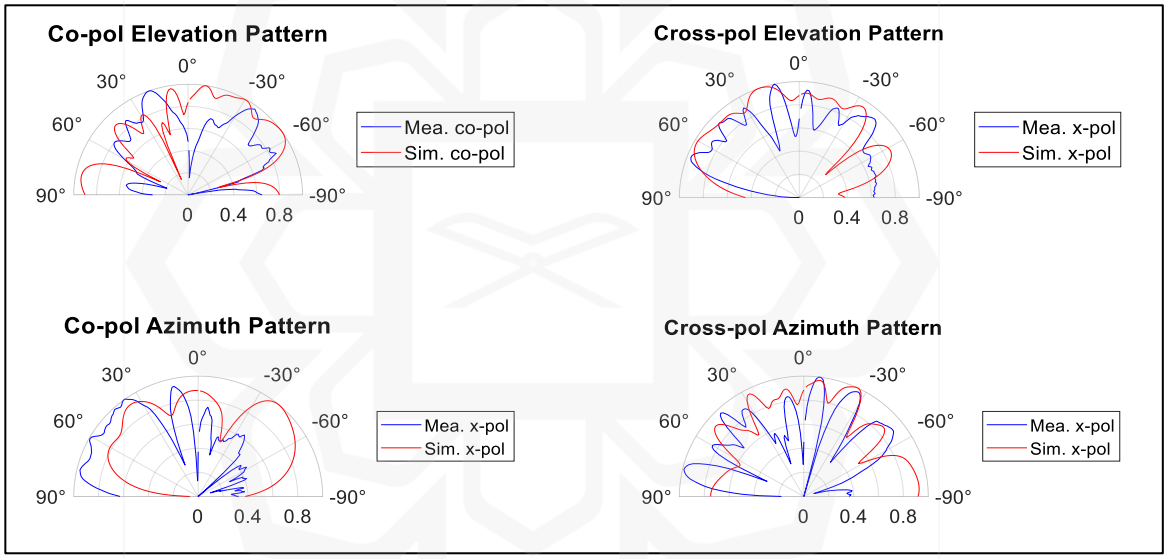

Figure 5.14 Normalized Realized Gain Pattern of the +45° Single Antenna

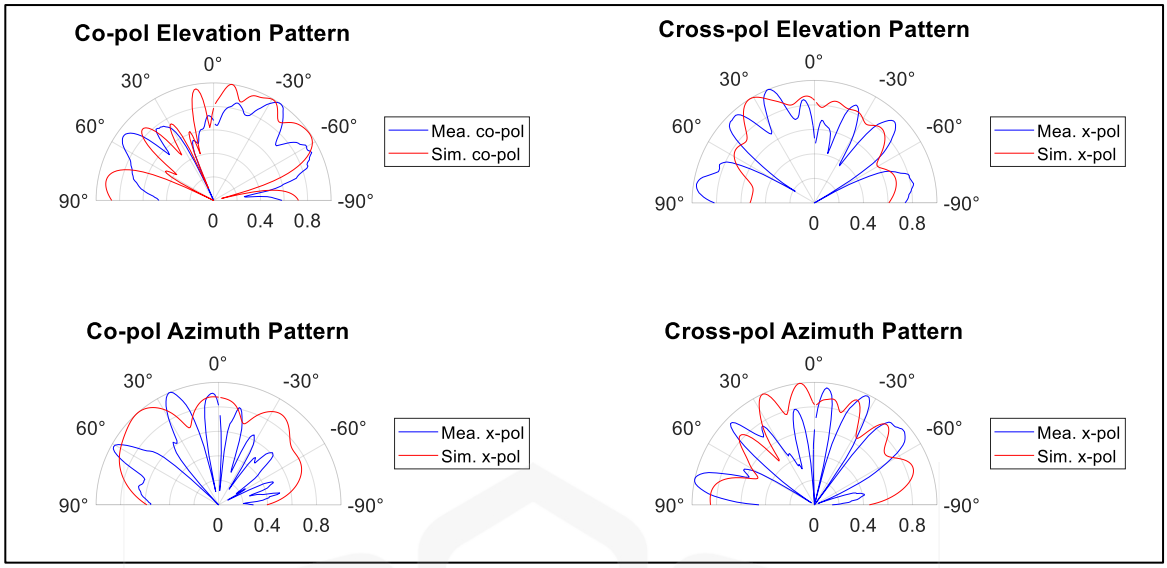

Figure 5.15 Normalized Realized Gain Pattern of the -45° Single Antenna

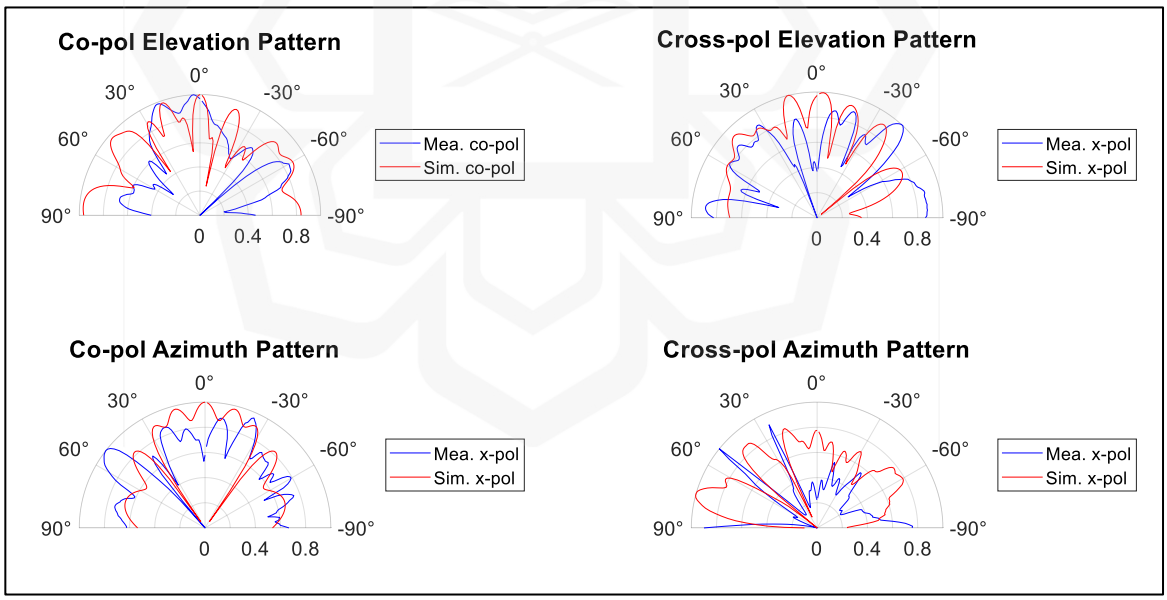

Figure 5.16 Normalized Realized Gain Pattern of the ±45° Dual-Polarised Antenna

As shown in Figure 5.17, the dual-polarised antenna array is measured in the normalized *H*-plane pattern. The beamformer that used to measure the pattern could only measure at the cut angle of phi, ϕ = 0° (θ = 0° to 360°). The peak realized gain at the *H*-plane is 6.45 dBi. The sidelobe levels at the antenna array are quite high, similar to the main lobe's level. It is to determine the exact main lobe. Besides, the best achieved peak gain is slightly lower than that of the dual-polarised antenna. Therefore, the antenna array has been improved in terms of its inter-element spacing by reducing 70.00 mm to 15.60 mm (9.69 λ to 2.159 λ). The entire antenna dimension of the proposed antenna array has been reduced. Reducing the inter-element spacing is necessary as to improve the main lobe pattern as well as the peak gain.

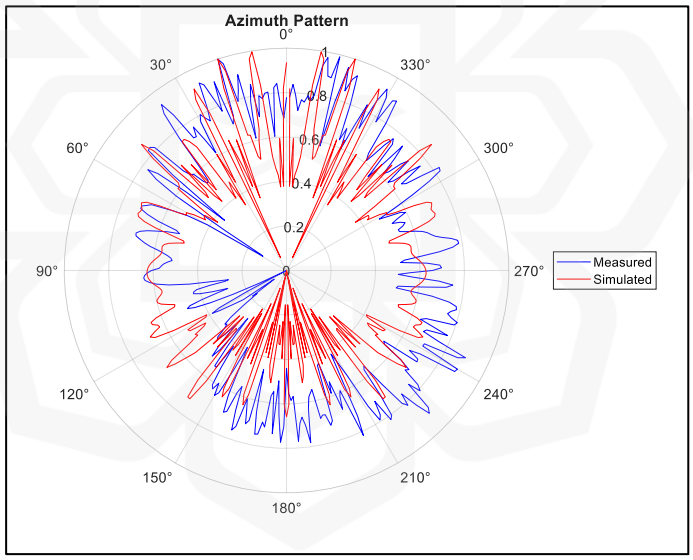

Figure 5.17 Normalized Realized Gain Pattern of the ±45° Dual-Polarised Antenna Array

As shown in Figure 5.18, the proposed antenna array is measured in the normalized *H*-plane pattern. The peak realized gain at *H*-plane is 6.72 dBi. The main lobe pattern is improved and the sidelobe levels are reduced by an average of 0.2 to 0.3 dBi. However, the measured peak gain of the proposed antenna array is nearly the same as the +45° single antenna. However, the main beam shows a directive pattern. The measured pattern of all antennas is then further analysed by doing a comparison to the simulated pattern.

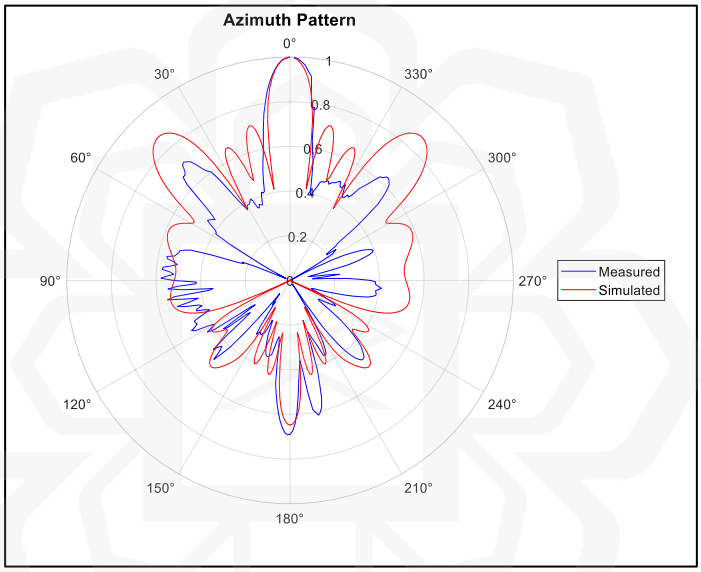

Figure 5.18 Normalized Realized Gain Pattern of the Proposed ±45° Dual-Polarised Antenna Array

The single antennas have an irregular-shaped pattern, while the dual-polarised antenna has a fan-shaped pattern. The antenna array's pattern has improved from an irregular shape to a pencil-beam shape. The main lobe pattern has also seen improvement. Generally, a good agreement is obtained between the simulated and measured results. Similarly, Table 5.3 shows the absolute peak realized gain of each simulated and measured pattern for all antennas.

Table 5.3 Simulated and Measured Absolute Peak Realized Gain (Proposed Antenna)

	Co-pol *E*-plane		**Cross-pol *E*-plane**		**Co-pol *H*-plane**		**Cross-pol *H*-plane**	
	Simulated (dBi)	Measured (dBi)	Simulated (dBi)	Measured (dBi)	Simulated (dBi)	Measured (dBi)	Simulated (dBi)	Measured (dBi)
+45°	4.94	6.82	2.07	3.65	5.68	4.96	5.68	8.42
-45°	4.98	4.37	1.90	7.84	3.81	3.83	5.85	4.26
Dual-Polarised	5.91	8.78	-77.20	12.25	5.91	11.16	5.63	13.84

Even though the best achieved peak realized gain is at the ±45° dual-polarised antenna, the main beam pattern is not clearly seen as a directive pattern. The directive main beam pattern is clearly seen at the proposed antenna array. The comparison between the measured and simulated pattern peak realized gain for all antennas is in suboptimal performance, however, the shape of the radiation pattern is well agreed with each other. The minor difference between them might be caused by the fabrication tolerance and measurement error. The peak realized gain for all antennas is not much affected despite of these differences.

Table 5.3 presents the simulated and measured radiation characteristics of various dual-linearly polarised antenna configurations. Among them, the proposed DLPAA design demonstrates superior performance across the several parameters. Although other designs such as the ±45° dual-polarised antenna show high peak gain, their radiation patterns do not exhibit clearly directive main beams, which is critical for accurate beam steering. In contrast, the proposed DLPAA offers a well-formed directional main beam, particularly in the co-polarised azimuth pattern, which is essential for effective pattern synthesis and phase prediction control. The axial ratio of the proposed design remains within an acceptable range, confirming linear polarization. Furthermore, the realized gain values for the co-polarised elevation and azimuth patterns are consistent and quite good, making this design

well-suited for 5G millimeter-wave applications. Based on these results, the proposed DLPAA is the most appropriate choice for implementation in beam-steering systems using AEP-DNN due to its balanced performance in gain, polarization purity, and pattern directivity.

The sidelobe levels shown in Figures 5.14 to 5.18 help us understand how well the antenna focuses its signal in the desired direction while reducing unwanted radiation in other directions. In Figures 5.14 and 5.15, which show the +45° and –45° single antennas, the sidelobes are quite noticeable, especially in the elevation view. This is expected because these are single-element antennas, so the beam is wider and there is less control over the radiation pattern. In Figure 5.16, which shows the ±45° dual-polarised antenna, the sidelobes are slightly lower because the antenna uses two polarizations and has better impedance matching. However, since it is still a single antenna, the improvement is limited. Figures 5.17 and 5.18 show the results for the antenna arrays. In these, especially in Figure 5.18, the sidelobes are much lower and the main beam is more focused. Still, some sidelobes remain, which could be caused by small errors in manufacturing, or mutual coupling between antenna elements. Overall, as the antenna design moves from a single element to the proposed array, the sidelobe levels clearly reduce and main beam's pattern improved.

The simulated radiation patterns shown in Figures 5.14 to 5.18 appear smooth and well-defined because they are generated in a full-wave environment using CST software, free from real-world disturbances such as fabrication errors, mechanical tolerances, and measurement limitations. In contrast, the measured patterns show inconsistent patterns due to several contributing factors during experimental setup. First, fabrication errors, such as slight misalignment of SMA connectors, substrate bending, or uneven soldering, could cause distortions in the radiation behavior. Second, measurement setup issues, including imperfect antenna placement on the holder, reflection from nearby objects, or environmental noise within the compact antenna test range (CATR), could interfere with accurate radiation pattern capture. Despite these discrepancies, the main lobe direction and general beam shape still show good agreement with simulations, confirming the validity of the antenna's performance.

The drop in measured gain could also be explained by similar small physical errors during fabrication and assembly, which are especially important at high frequencies like 28 GHz. Slight changes in the patch size, substrate thickness, or ground plane, such as uneven etching or bending which could affect how the antenna radiates and reduce its efficiency. If the coaxial connector or probe is not perfectly aligned, it could cause extra signal loss or interfere with the signal flow. Also, poor soldering or small gaps between layers could lead to energy loss. These small imperfections, although minor, could add up and reduce the amount of power the antenna could radiate, which results in a lower measured gain compared to the ideal gain seen in simulation. Therefore, the gain drop is due to small but important fabrication and alignment issues.

The reason the cross-polarised patterns appear stronger than the co-polarised patterns is due to the symmetric design of the slanted ±45° patch antenna elements. Normally, we expect co-polarization (the intended signal direction) to be stronger, but in this case, the antenna radiates quite high in both directions. Previous studies by (Lv et al., 2021; Vallozzi, 2016) and (Zeng et al., 2015) explain that antennas with slanted ±45° patches naturally create balanced electric fields, which means they could send signals in both polarizations. This makes the cross-polarised radiation stronger than usual. In other words, the geometry of the patch and its slanted orientation make it easier for energy to radiate in both co- and cross-polarised directions. When both ports are excited in a dual-polarised antenna, the interaction between the two polarization paths could cause some power leakage or mixing, which increases the cross-polarised radiation. While the symmetry helps achieve good isolation and polarization diversity, it also makes perfect polarization purity more difficult to maintain. Therefore, the slightly higher cross-polar levels observed in the radiation patterns are a trade-off due to the slanted structure's inherent symmetry.

The proposed DLPAA is evaluated for its axial ratio, realized gain, and main beam's pattern, demonstrating superior performance in polarization purity and directional gain at 28 GHz. The antenna maintains a good axial ratio of 40 and achieves a simulated gain of 14.40 dBi in elevation and 13.10 dBi in azimuth. This performance supports precise beam-steering when integrated with the AEP-DNN method. In comparison, the ±45° dual-

polarised array presented by (Lv et al., 2021) operates at 30 GHz using a single-layer series-fed structure and achieves approximately 10.8 dBi realized gain. While their design emphasizes simplicity and effective polarization rotation through ±45° feeding, it lacks beam-steering capability and does not offer the same level of control over the radiation pattern. Therefore, the proposed DLPAA provides a more flexible and high-performance solution for 5G millimeter-wave applications, where beam directivity and adaptive control are critical.

5.6 VERIFICATION OF AEP-BASED METHOD

In order to verify the proposed AEP-based method, the beamformer is used to excite and tune the input phases of the proposed DLPAA. *TMYTEK 5G FR2* beamformer with 1 x 4 RF ports is used for the antenna array verification. Four independent RF channels synthesise beams by adjusting the phase and amplitude of each channel. The intuitive *GUI TMXLAB Kit* (*TLK software*) connects the beamformer via the local area network (LAN) port to control the phase and amplitude of each RF port to form the beams. The top view of the built-in beamformer and the connection of the proposed DLPAA with the built-in beamformer is shown in Appendix E.

5.6.1 Verification Results

The beamformer's input phases are tuned to steer the main beam to a desired location. Table 5.4 shows the list of input phases at each desired steering angle in degrees. The measured pattern after tuning the phases is compared to the CST and AEP patterns as shown in Figure 5.19.

Table 5.4 The Input Phases of the Beamformer

Desired Steering Angles (°) / **Port of Input Phases (°)**	**0**	**11**	**25**
Port 1	0	130	250
Port 2	0	85	170
Port 3	0	45	85
Port 4	0	0	0

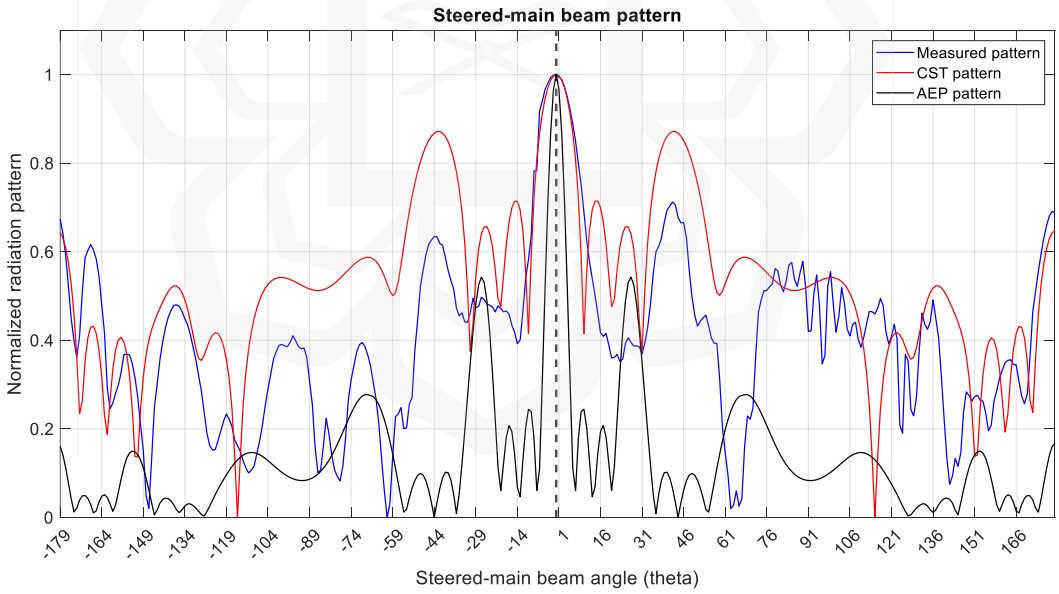

(a)

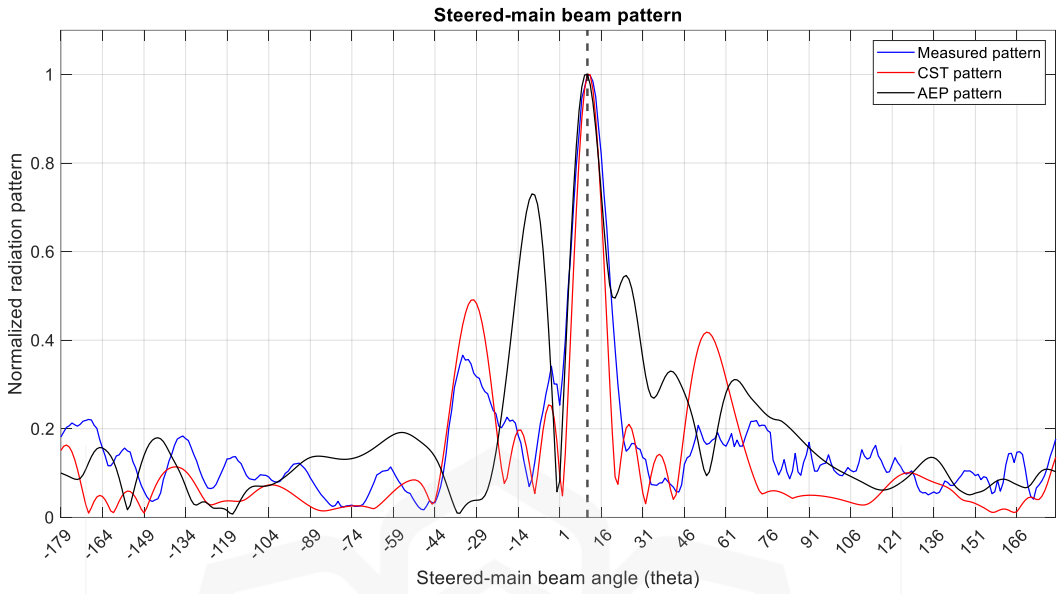

(b)

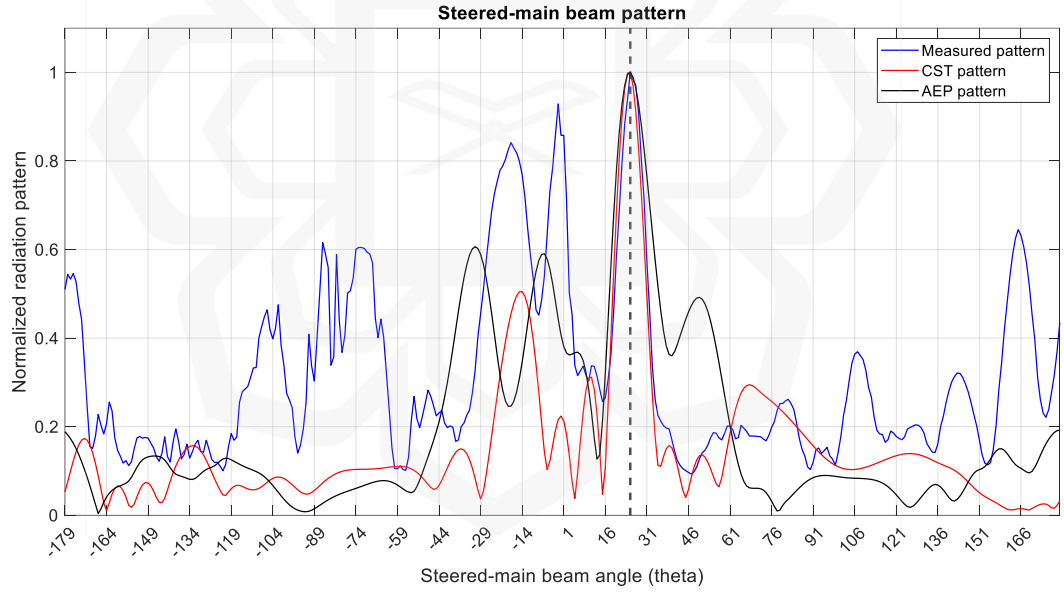

(c)

Figure 5.19 The Measured, PMM, and CST Patterns at Each Steered-Main Beam Angle of (a) 0° (b) 11° and (c) 25°

Based on Figure 5.19, the vertical ‘dot’ line indicates the steered-main beam angle of direction. The antenna array has been successfully steered to the desired main beam angle using the input phases with the beamformer. The measured radiation pattern of the desired angle is similar to the CST and AEP patterns, despite at different levels of gain except at the main beam. This could be caused by the placement of the antenna array on the antenna holder, interference losses, and the experimental surroundings of the half-foam provided during the measurement.

The performance of the proposed AEP-DNN method is evaluated using a dataset generated from full AEP of a 1×4 dual-linearly polarised antenna array at 28 GHz. This approach captures realistic electromagnetic behavior, including mutual coupling effects, and achieves low RMSE values ranging from 1.3 to 1.5 and validation loss values between 1.7 and 1.9, confirming its accuracy for beam pattern prediction. In contrast, (Alam et al., 2024) propose a deep learning approach for AESA antennas that significantly reduces dataset size by exploiting the phase-shift symmetry in uniform arrays. Their method eliminates the need for extensive training data as the excitation patterns could be generalized, resulting in faster training and improved scalability for larger arrays. However, this simplification might limit the accuracy of the model in representing real-world coupling effects and element-specific variations, especially at millimeter-wave frequencies where such factors are critical. Therefore, while (Alam et al., 2024) is advantageous in terms of computational efficiency and scalability, this AEP-DNN method approach offers superior antenna structure’s reliability and pattern accuracy, making it more suitable for high-precision applications such as beam-steering in 5G millimeter-wave systems.

Table 5.5 shows the comparison summary of the measured output antenna performance of this study and the other previous works. This study shows good performance mainly in terms of its mutual coupling. Even though the realized gain is not the best compared to the other works, the best achieved peak realized gain is quite significant for an antenna operating at the high frequency of 28 GHz. The measured S_{11} for all antennas shows good performance, as it successfully performed less than -10 dB. The mutual coupling performance of the antenna array shows satisfactory results as they obtained less than -20 dB (Saeidi-Manesh et al., 2020). This chapter is focused on the

verification of simulation results of the antennas, AEP-based method and full-wave modelling (CST) for the radiation pattern computation. Table 5.6 shows the comparison summary of the beam pattern synthesis of this study and the other previous works.

Table 5.5 Comparison between the Proposed Fabricated Proposed ±45° Dual Linearly Polarised Antenna Array and Previous Works

Parameters / **Studies**	**Frequencies (GHz)**	**Methods of Dual Polarization**	**Reflection Coefficient (at 28 GHz) (dB)**	**Mutual Coupling (dB)**	**Realized Gain (dBi)**
(Xia et al., 2022)	23.40-30.00 (n257 or n258)	SIW	<-15.00	<-15.60	8.90
(Zhu & Deng, 2021)	26.00-30.00 (n257 and n261)	Double layer stacked up SIW	-20.00 to -40.00	<-15.00	9.38 and 9.51
(Jiang et al., 2023)	24.00-33.00	Integrated dipole with parasitic patches	<-15.00	<-14.00	14.00
This work	28.00	Single layer	<-11.57	<-20.00	6.72

Table 5.6 Comparison between the Proposed AEP-DNN method and Previous Works

Parameters / **Studies**	**Aim**	**Method**	**Type of polarization and number of elements**	**Computational time (minutes)**	**Training/ Validation RMSE or loss**
(Montaser & Mahmoud, 2021)	Pattern synthesis (phase)	Simulations using CST for DNN database and linked to MGSA-PSO algorithm, MATLAB coded for initial phases to feed DNN model	Circular	Not reported	Not reported
(Cui et al., 2021)	Synthesizing beampatterns in linear antenna arrays including on non-	Encoder-decoder	Linear 149 (ideal array) 32 (microstrip array) 50 (dipole array)	24.60 (ideal array) 27.00 (microstrip array) 16.20 (dipole array)	Training loss: 0.0003 (ideal array) 0.0008 (microstrip array)

	ideal array conditions				0.0002 (dipole array)
(Iye et al., 2022)	Pattern synthesis using one measurement of the radiation pattern	Inputs the measured radiation power pattern of the antenna array into a neural network to estimate phase errors	Linear 8	210.00	Training and validation RMSE: 0.000176, 0.00801
(Liang et al., 2023)	Pattern synthesis using AF and AEP	CST for input phases	Linear 12	18.05	Not reported
This work	Pattern synthesis (phase) using AEP-DNN	Simulations using AEP for DNN database	Linear 8	2-3	1.3-2.3

5.7 SUMMARY OF CHAPTER

Chapter 5 explains and analyzes the performance of the proposed dual-linearly polarised antenna array (DLPAA) and the AEP-DNN method for beam steering. This chapter has successfully validated the proposed dual-polarised antenna array design and its associated AEP-DNN beamforming algorithm through fabrication and measurement at 28 GHz. The fabricated antennas, comprising single slanted ±45°patches, a dual-polarised element, and the proposed 1×4 DLPAA were measured using standard VNA and chamber facilities. The proposed DLPAA shows better results than the previous ±45° design, with lower reflection (S_{11}), more directive main beam's pattern, and stable axial ratio using VNAs and anechoic chambers. The measured results match the simulations quite well, although some small differences are seen due to fabrication and measurement issues. Mutual coupling between ports is kept below –20 dB, showing good isolation. The AEP-DNN model, trained using realistic AEP data, successfully steers the main beam to 0°, 5°, 10°, 15°, and 20°, with low RMSE and loss values. These results are verified using both CST simulations and the pattern multiplication method. The figures and tables show that the antenna gain is stable and the beam direction is accurate. Although the measured patterns are slightly misaligned compared to the smooth simulated ones which is mainly due to alignment or testing limitations, and the overall performance proves that the proposed antenna and DNN method work well for 5G millimeter-wave beam-steering applications.

CHAPTER SIX

CONCLUSION AND FUTURE RECOMMENDATIONS

6.1 CONCLUSION

In conclusion, the emerging demand for high-speed networks has led many researchers to focus on enhancing 5G wireless communication performance. Antenna pattern optimization methods for beam-steering capability improvement are widely researched. Among the optimization methods, deep neural networks (DNN) are considered one of the best methods for 5G networks. In this study, the proposed Active Element Pattern (AEP) integrated with DNN's multi-layer perceptron network has successfully produced an enhanced AEP-DNN algorithm. The research demonstrates that the method predicts input phases to steer the main beam pattern to a desired location, enhancing the beam-steering capability for the dual-polarised antenna for wider scanning angles. The Computer Simulation Technology (CST) and MATLAB were used for simulation, AEP-DNN implementation, and measurement of proposed Dual Linearly Polarised Antenna Array (DLPAA) to investigate antenna performance. The proposed AEP-DNN method offers faster deep learning processing times than the full-wave model of CST and pattern multiplication method. The AEP-DNN is an approximation tool for the pattern synthesis yet it considers the mutual coupling effect.

The study's first objective explores dual-polarised antenna arrays at millimeter-wave frequencies and suggests a proposed ±45° DLPAA operating at 28 GHz. The antenna's simple and compact configuration, with a single feeding port exciting dual polarization simultaneously, sets it apart from previous designs. The design utilizes slanted radiating patch antennas for dual polarization and is less complex, focusing on mobile applications. The design is necessary to introduce new methods for the DNN database for radiation pattern synthesis. The proposed DLPAA is a 1 x 4 linear array with dimensions of 62.45 x 23.08 x 1.575 mm^3, and the inter-element spacing is 15.60 mm. The proposed DLPAA simulation is conducted using the CST Simulation tool. The simulated reflection

coefficient (S_{11}), bandwidth, directivity, and realized gain of co-polarization elevation and azimuth are -12 dB, 0.46 GHz, 14.89 dBi, 14.4 dBi, and 13.1 dBi.

In the second objective, developing an algorithm using the AEP-DNN method for pattern synthesis and validate it using the conventional method (pattern multiplication method) and full-wave modelling (CST tool). The AEP is obtained from the proposed DLPAA through MATLAB computation. The AEP-DNN method is introduced for efficient performance with reduced DNN layers. The AEP method is utilized for training and validation, and the AEP-DNN method is compared to pattern multiplication method and full-wave modelling, aiming to simplify the neural network structure, reduce complexity and time consumption. The performance of the AEP-DNN method is executed using MATLAB software, and the desired steering angles have successfully been steered to the theta value of 5°, 10°, 15°, and 20°. It has been demonstrated that the desired main lobe location is successfully matched with the AEP and CST patterns. The training and validation of RMSE and loss have successfully converged to its minimum, between 1.33 to 2.33. The processing time for deep learning process to get to the possible low convergence rate is only 2 to 3 minutes. It could be concluded that the investigation on the AEP-DNN method has been successfully implemented for pattern synthesis of the proposed DLPAA.

The final objective involves measuring the fabricated antennas to validate the simulation results and establish the effectiveness of pattern synthesis using the AEP approach. The algorithm has been tested using a full-wave method (CST) and measurement procedures in an anechoic chamber. The measurement is carried out by using the vector network analyzer (VNA) and anechoic chamber to obtain important parameters: reflection coefficient (S_{11}), radiation pattern, and peak realized gain. The measured S_{11} of the proposed DLPAA for port 1, port 2, port 3, and port 4 are -15.05 dB, -11.57 dB, -12.69 dB, and -35.23 dB. The simulated co-polarised gains are improved from 12.10 dBi to 14.40 dBi (elevation) and 12.00 dBi to 13.10 dBi (azimuth). The proposed DLPAA has also been measured to test the antenna's capability to steer the main beam into a desired angle direction. The test samples of measured desired steering angle are 0°, 11°, and 25°. The desired radiation pattern obtained from the measurement is compared to the AEP and CST patterns for verification purposes. It shows that the desired radiation pattern is well agreed

with the AEP and CST patterns. There are few discrepancies between them, possibly due to the approximation of AEP itself, which is only accurate for large arrays. Besides, the AEP pattern does not account for the ground edge effect. The CST pattern is accurate but very time-consuming, and requiring larger memory usage. Another factor is that the experimental setup for the antenna measurement is the half-foam provided. The foam does not fully cover the surrounding of the antenna during measurement. The metal objects existing in the surrounding during the measurement might influence the radiation pattern of the antenna.

The proposed DLPAA achieves directional gain at 28 GHz, with simulated gains of 14.40 dBi (elevation) and 13.10 dBi (azimuth) which supporting accurate beam-steering with the AEP-DNN method at 5°, 10°, 15°, and 20°. In contrast, (Lv et al., 2021)'s ±45° dual-polarised array at 30 GHz offers simpler structure and 10.8 dBi gain but lacks beam-steering and pattern control. Thus, the proposed DLPAA is more suitable for advanced 5G millimeter-wave applications requiring flexible and accurate main beam's prediction control.

The AEP-DNN method, trained using full AEP data from a 1×4 dual-polarised array at 28 GHz, captures realistic coupling effects and achieves low RMSE (1.3–1.5) and validation loss (1.7–1.9), ensuring accurate beam prediction. In comparison, (Alam et al., 2024) reduce dataset size using phase-shift symmetry for faster training and better scalability but might compromise accuracy in modeling real-world effects. Thus, while (Alam et al., 2024) is efficient, AEP-DNN method provides greater prediction's accuracy for 5G millimeter-wave beam-steering.

6.2 CHALLENGES

Research challenges are difficulties or complications that researchers might face during the study. Recognizing these obstacles could help finding another approach and offer a specific

direction for overcoming limitations. Below are a few examples of obstacles encountered in the research of this study:

1. Time constraints: The Rogers RT5880 substrate material is purchased from a foreign country, resulting in a lengthy delivery time for the item. Besides, making the antenna design sample and sending it to an industrial company for fabrication is a time-consuming process.

2. Instrumentation issues: The radiation pattern measurement at Chang Gung University, Taiwan is carried out with a self-built chamber as there is no available horn antenna (transmitter) specifically for the 28 GHz. A mixer was used to down-convert the frequency to 28 GHz. Furthermore, the SMA coaxial connectors broke multiple times due to the very sensitive tiny size of the pin inside the connector, requiring us to reorder them from abroad.

3. Technical limitations: Limited resources are available for utilizing a beamformer to measure radiation patterns by employing multiple ports to excite the source of the antenna array. Additionally, there are only a few vector network analysers for measuring the reflection coefficient at high frequency bands.

4. Project timeline: The experiment has been delayed beyond the initial expectations due to Covid-19 restrictions in place from 2020-2021, limiting movement across states, institutions, labs, and requiring adherence to specific rules and regulations.

A new approach was identified to ensure the project stayed on schedule despite unexpected challenges. These situations contributed to the development of patience, resilience, and a more solution-focused mindset. Time management skills were also enhanced through improved organization, task prioritization, and appropriate delegation. These challenges provided valuable learning opportunities, supporting growth in both research skills and attitude. The experience also demonstrated the importance of self-awareness and adaptability, qualities essential in academic and professional environments.

6.3 CONTRIBUTIONS

The contributions of this thesis are:

1. Designing an antenna that operates effectively at 28 GHz (a key frequency for 5G applications) is challenging due to issues like path loss and interference. The paper addresses design considerations specific to high-frequency bands, optimizing for aspects such as gain, bandwidth, and efficiency.

2. By using dual polarization, the antenna could transmit and receive signals in two orthogonal polarizations, enhancing data rates and enabling more robust communication. Dual polarization could also improve signal quality in environments with multipath interference, which is critical for applications like 5G and beyond.

3. Beam-steering is essential for focusing signal energy towards specific users or devices, which is especially useful in millimeter-wave communication (28 GHz). The design explores how the antenna array could direct beams dynamically, enhancing both the range and the quality of the communication link.

4. Designing an array with beam-steering capabilities at 28 GHz requires specific attention to array configuration, element spacing, and phase shifting. The research addresses the configuration needed for optimal beam-steering with minimal sidelobe levels and maximized main lobe's gain.

5. The AEP-DNN algorithm is presented that could synthesise the radiation pattern for proposed DLPAA with reduced DNN layers yet given an efficient performance.

6. The training and validation datasets with smaller dimensions making them feasible for proposed DLPAA that are obtained by the AEP method.

7. Validation of the proposed AEP-DNN method is carried out by comparing with the pattern multiplication method and full-wave modelling (CST). The radiation patterns synthesised using DNN followed the desired patterns of the steered-main beam pattern.

8. The study includes benchmarks comparing the performance of the AEP-DNN-enhanced beam-steering with traditional methods (like conventional beam-steering techniques).

9. By demonstrating a practical beam-steering antenna system at 28 GHz, this research contributes to millimeter-wave technology adoption in 5G. The dual-polarised, AI-optimized beam-steering antenna could be particularly relevant for mobile applications needing high-bandwidth, directional communication.

6.4 IMPLICATIONS

This study has shown that the AEP-DNN method, providing a wider scanning angle and less time in predicting the steering of the main beam pattern into a desired location, has greater performance than previous works. The outcomes of the proposed method supported the idea that beam-steering capability in a 5G wireless communication could be reliable. In this light, radiating beam scanning angle could be improved by the dual-polarization feature and optimizing the phase coefficients of the proposed DLPAA. In this regard, this study has demonstrated that the research objectives outlined in Chapter 1 of this thesis have been met. Additionally, it could be possible to pursue digital beam-steering analysis incorporating a more extensive implementation using AEP-DNN in the very near future. Extended designs like MIMO antenna arrays might be used. The experimental results would be based on the parameters suggested in this thesis, which are compatible with the laboratories and other constraints. The results could be tested in a real environment, including indoor and outdoor environments.

6.5 RECOMMENDATION AND FUTURE WORKS

The forthcoming 5G technology is undergoing intensive research. The goal of this study is to address the dual-polarised feature in antenna design that could support millimeter-wave frequency at 28 GHz in order to overcome the high path loss, and to implement the AEP-DNN method in performing the main beam-steering capability to offer a wider scanning angle and lesser time of phase coefficients prediction process. The study makes the following recommendations for directions in future research:

1. Consider the alternative configuration of radiating antenna elements for arrays to decrease inter-element spacing and mutual coupling. Optimizing the geometry might further enhance array efficiency.

2. Scalability to planar arrays configuration. Expanding to 2D or planar arrays allows for beam-steering in both azimuth and elevation, which is crucial for massive MIMO and advanced 5G systems.

3. Consider alternative substrate materials and thicknesses. Changing the substrate material or thickness could help reduce losses, improve bandwidth, and potentially improve fabrication feasibility at millimeter-wave frequencies.

4. Explore increasing the number of radiating elements in the antenna array and integrating reconfigurable hardware like phase shifters. Adding more elements improves gain and beam directivity, while reconfigurable hardware like phase shifters supports option on real-time adaptive beam-steering.

5. Testing under multipath environments or non-line-of-sight conditions. Real environments often have reflections and obstacles. Testing in these settings helps validate the robustness of the AEP-DNN method.

6. Explore larger datasets provided for the AEP-DNN method to investigate its optimal results. More data improves the training quality and helps the DNN model generalize better, especially for more complex or varied scenarios.

7. Implement the AEP-DNN method on other types of antennas. Demonstrates the flexibility and applicability of the method beyond the current patch array.
8. Improvise the AEP-DNN method to account for ground edge effects which are more accurate for small sizes of arrays. These effects become important in small or compact arrays, and including them could improve the accuracy of the synthesised beam patterns.

REFERENCES

Alam, Z., Masood, A. R., Abdullah, M. A., Khattak, S., Saleem, A. B., & Ullah, I. (2024). AESA Antennas using Machine Learning with Reduced Dataset. *Radio engineering*, *33*(3), 397.

Ali, W. A., & Hassan, A. H. (2014). A hybrid least mean square/sample matrix inversion algorithm using microstrip antenna array. 2014 Science and Information Conference.

Arora, R., Basu, A., Mianjy, P., & Mukherjee, A. (2016). Understanding deep neural networks with rectified linear units.

Balanis, C. A. (2016). *Antenna theory: analysis and design*. John wiley & sons.

Bayraktar, Z., Komurcu, M., Bossard, J. A., & Werner, D. H. (2013). The wind driven optimization technique and its application in electromagnetics. *IEEE Transactions on Antennas and Propagation*, *61*(5), 2745-2757.

Bianco, S., Napoletano, P., Raimondi, A., Feo, M., Petraglia, G., & Vinetti, P. (2020). AESA adaptive beamforming using deep learning. 2020 IEEE Radar Conference (RadarConf20).

Buttazzoni, G., Babich, F., Vatta, F., & Comisso, M. (2020). Geometrical synthesis of sparse antenna arrays using compressive sensing for 5G IoT applications. *Sensors*, *20*(2), 350.

Cai, S., Li, Y., Zhu, H., Wu, X., & Su, D. (2021). A Novel Electromagnetic Compatibility Evaluation Method for Receivers Working under Pulsed Signal Interference Environment. *Applied Sciences*, *11*, 9454.

Chen, K., Yun, X., He, Z., & Han, C. (2007). Synthesis of sparse planar arrays using modified real genetic algorithm. *IEEE Transactions on Antennas and Propagation*, *55*(4), 1067-1073.

Chowdhury, M. H., Hossain, Q. D., Hossain, M. A., & Cheung, R. C. C. (2019). Single feed circularly polarized crescent-cut and extended corner square microstrip antennas for wireless biotelemetry. *International Journal of Electrical and Computer Engineering*, *9*(3), 1902-1909.

Chu, C., Zhu, J., Liao, S., Zhu, A., & Xue, Q. (2019, 19-22 May 2019). 28/38 GHz Dual-band Dual-polarized Highly Isolated Antenna for 5G Phased Array Applications. 2019 IEEE MTT-S International Wireless Symposium (IWS).

Cui, C., Li, W. T., Ye, X. T., Rocca, P., Hei, Y. Q., & Shi, X. W. (2021). An effective artificial neural network-based method for linear array beampattern synthesis. *IEEE Transactions on Antennas and Propagation*, *69*(10), 6431-6443.

Darboe, O., Konditi, D. B. O., & Manene, F. (2019). A 28 GHz rectangular microstrip patch antenna for 5G applications. *International Journal of Engineering Research and Technology*, *12*(6), 854-857.

Deng, C., Liu, D., Yektakhah, B., & Sarabandi, K. (2020). Series-fed beam-steerable millimeter-wave antenna design with wide spatial coverage for 5G mobile terminals. *IEEE Transactions on Antennas and Propagation*, *68*(5), 3366-3376.

Elhabbash, T., & Skaik, T. (2019, 26-27 March 2019). Design of Dual-band Dual-polarized MIMO Antenna for mm-wave 5G Base Stations with Octagonal Prism Structure. 2019 IEEE 7th Palestinian International Conference on Electrical and Computer Engineering (PICECE).

Fabiani, B., Silveira, E., Pina, M., & Nascimento, D. (2018). Nonlinear constrained beamforming algorithm for circularly polarized phased arrays. *IEEE Antennas and Wireless Propagation Letters*, *17*(9), 1692-1696.

Fante, K. A., & Gemeda, M. T. (2020). Broadband microstrip patch antenna at 28 GHz for 5G wireless applications. *International Journal of Electrical and Computer Engineering*, *11*(3), 2238-2244.

Feng, B., Luo, T., Zhou, L., & Sim, C. Y. D. (2020). A dual-polarized antenna with low cross polarization, high gain, and isolation for the fifth-generation array/multiple-input multiple-output communications. *International Journal of RF and Microwave Computer-Aided Engineering*, *31*.

Fuchs, B., & Rondineau, S. (2016). Array pattern synthesis with excitation control via norm minimization. *IEEE Transactions on Antennas and Propagation, 64*(10), 4228-4234.

Fyfe, C. (2005). Artificial neural networks. In *Do smart adaptive systems exist? Best practice for selection and combination of intelligent methods* (pp. 57-79). Springer.

Ghaderi, M. R., & Amiri, N. (2023). Application of Machine Learning Techniques in Phased Array Antenna Synthesis: A Comprehensive Mini Review. J. Commun., 18(10), 629–642.

Gianfagna, C., Swaminathan, M., Raj, P. M., Tummala, R., & Antonini, G. (2015). Enabling antenna design with nano-magnetic materials using machine learning. 2015 IEEE Nanotechnology Materials and Devices Conference (NMDC).

Goodfellow, I. (2016). Nips 2016 tutorial: Generative adversarial networks.

Gorman, J. D. (2015). The application of optimisation algorithms in antenna array beampattern synthesis. 2015 26th Irish Signals and Systems Conference (ISSC).

Gregory, M. D., Bayraktar, Z., & Werner, D. H. (2011). Fast optimization of electromagnetic design problems using the covariance matrix adaptation evolutionary strategy. *IEEE Transactions on Antennas and Propagation*, *59*(4), 1275-1285.

Hammad, M. (2024). Deep Learning Activation Functions: Fixed-Shape, Parametric, Adaptive, Stochastic, Miscellaneous, Non-Standard, Ensemble.

He, M., Zheng, Z., Wang, W.-Q., & Kang, Z. (2022). Pattern synthesis for uniform linear array using genetic algorithm and artificial neural network. *Multidimensional Systems and Signal Processing*, 1-11.

He, Q.-Q., & Wang, B.-Z. (2008). Design of microstrip array antenna by using active element pattern technique combining with Taylor synthesis method. *Progress In Electromagnetics Research*, *80*, 63-76.

Hogg, D. C. (1993). Fun with the Friis free-space transmission formula. *IEEE Antennas and Propagation Magazine*, *35*(4), 33-35.

Hwang, I. J., Jo, H. W., Ahn, B. K., Oh, J. i., & Yu, J. W. (2019, 31 March-5 April 2019). Cavity-backed Stacked Patch Array Antenna with Dual Polarization for mmWave 5G Base Stations. 2019 13th European Conference on Antennas and Propagation (EuCAP).

Iye, T., van Wyk, P., Matsumoto, T., Susukida, Y., Takaya, S., & Fujii, Y. (2022). Neural network-based phase estimation for antenna array using radiation power pattern. *IEEE Antennas and Wireless Propagation Letters*, *21*(7), 1348-1352.

Jais, I. K. M., Ismail, A. R., & Nisa, S. Q. (2019). Adam optimization algorithm for wide and deep neural network. *Knowl. Eng. Data Sci.*, *2*(1), 41-46.

Jiang, W., Liao, S., Che, W., & Xue, Q. (2023). Millimeter-wave wideband±45° dual-polarized phased array antenna based on compact wideband widebeam dipole element antenna. *IEEE Antennas and Wireless Propagation Letters*, *22*(8), 1813-1817.

Johari, S., Abdul Jalil, M., & Ibrahim, S. I. (2018). 28 GHz Microstrip Patch Antennas for Future 5G. *Journal of Engineering Studies and Research*, *2*, 1-6.

Kaeib, A. F., Shebani, N. M., & Zarek, A. R. (2019). Design and analysis of a slotted microstrip antenna for 5G communication networks at 28 GHz. 2019 19th International Conference on Sciences and Techniques of Automatic Control and Computer Engineering (STA).

Kamath, S., Harsha, K. S., & Zihan, M. (2019). Design of Microstrip Antenna Array and Analysis of different Beamforming techniques for mm-wave MIMO Systems. 2019 3rd International Conference on Computing Methodologies and Communication (ICCMC).

Khalaf, A. A., El-Daly, A.-R. B., & Hamed, H. F. (2018). A hybrid NLMS/RLS algorithm to enhance the beamforming process of smart antenna systems. *Journal of Telecommunication, Electronic and Computer Engineering (JTEC)*, *10*(1-4), 15-22.

Khashman, A., Serakinci, N., & Kizilkanat, M. (2020). Metabolic Syndrome Risk Evaluation Based on VDR Polymorphisms and Neural Networks. 10th International Conference on Theory and Application of Soft Computing, Computing with Words and Perceptions-ICSCCW-2019.

Khattak, M. K., Khattak, M. S., Rehman, A., Lee, C., Han, D., Park, H., & Kahng, S. (2017). A flat, broadband and high gain beam-steering antenna for 5G communication. 2017 International Symposium on Antennas and Propagation (ISAP).

Kim, J. H., & Choi, S. W. (2020). A deep learning-based approach for radiation pattern synthesis of an array antenna. *IEEE access*, *8*, 226059-226063.

Kouhalvandi, L., & Matekovits, L. (2024). Beam-Steering Antenna Technique Using Operational Amplifiers for Sub-6 GHz. *IEEE access*, *PP*, 1-1.

Krishna, S., Mishra, G., & Sharma, S. K. (2018). A series fed planar microstrip patch array antenna with 1D beam steering for 5G spectrum massive MIMO applications. 2018 IEEE radio and wireless symposium (RWS).

Kummer, W. H. (1992). Basic array theory. *Proceedings of the IEEE*, *80*(1), 127-140.

Lee, S., Kim, S., & Choi, J. (2019, 31 March-5 April 2019). Dual-Band Dual-Polarized Proximity Fed Patch Antenna for 28 GHz/39 GHz 5G Millimeter-Wave Communications. 2019 13th European Conference on Antennas and Propagation (EuCAP).

Liang, Z., Gao, H., Jin, C., & Deng, J. (2023). Beam Steering for Array Antenna Based on Deep Learning. 2023 International Applied Computational Electromagnetics Society Symposium (ACES-China).

Liu, B., Aliakbarian, H., Ma, Z., Vandenbosch, G. A., Gielen, G., & Excell, P. (2013). An efficient method for antenna design optimization based on evolutionary computation and machine learning techniques. *IEEE Transactions on Antennas and Propagation*, *62*(1), 7-18.

Lovato, R., & Gong, X. (2019). Phased antenna array beamforming using convolutional neural networks. 2019 IEEE International Symposium on Antennas and Propagation and USNC-URSI Radio Science Meeting.

Lv, Q., Yang, Y.-H., Zhou, S.-G., Shao, C., Zhou, D., & Sim, C. Y. D. (2021). Design of a Single-Layer ±45° Dual-Polarized Directional Array Antenna for Millimeter Wave Applications. *Sensors*, *21*, 4326.

Mei, P., Zhang, S., & Pedersen, G. F. (2021). A Dual-Polarized and High-Gain X-/Ka-Band Shared-Aperture Antenna With High Aperture Reuse Efficiency. *IEEE Transactions on Antennas and Propagation*, *69*(3), 1334-1344.

Midasala, V., & Siddaiah, P. (2016). Microstrip patch antenna array design to improve better gains. *Procedia computer science*, *85*, 401-409.

Mohamed, M., Dini, A., Soliman, M. M., & Imran, A. (2020). *Design of 2x2 Microstrip Patch Antenna Array at 28 GHz for Millimeter Wave Communication*.

Mohamed, M. Y., Dini, A. M., Soliman, M. M., & Imran, A. Z. M. (2020). Design of 2x2 Microstrip Patch Antenna Array at 28 GHz for Millimeter Wave Communication. 2020 IEEE International Conference on Informatics, IoT, and Enabling Technologies (ICIoT).

Mohri, M. (2018). Foundations of machine learning. In: MIT press.

Montaser, A. M., & Mahmoud, K. R. (2021). Deep learning based antenna design and beam-steering capabilities for millimeter-wave applications. *IEEE access*, *9*, 145583-145591.

Mungur, D., & Duraikannan, S. (2018). Design and analysis of 28 GHz millimeter wave antenna array for 5G communication systems. *Journal of Science Technology Engineering and Management-Advanced Research & Innovation*, *1*(3), 10.

Ochoa, S., Haro-Baez, R., Vizcaíno, I. P., & Benítez, D. S. (2017). New design of T-type power divider network in microstrip technology for C-band downlink. 2017 IEEE URUCON.

Pandey, A. K., & Singh, M. (2024). Antenna Optimization using Machine Learning Algorithms and their Applications: A Review. *Journal of Engineering Science & Technology Review*, *17*(2).

Pant, M., Malviya, L., & Choudhary, V. (2020). Gain and Bandwidth Enhancement of 28 GHz Tapered Feed Antenna Array.

Parchin, N. O., Al-Yasir, Y. I. A., Ali, A. H., Elfergani, I., Noras, J. M., Rodriguez, J., & Abd-Alhameed, R. A. (2019). Eight-element dual-polarized MIMO slot antenna system for 5G smartphone applications. *IEEE access*, *7*, 15612-15622.

Paul, L. C., Hosain, M. S., Sarker, S., Prio, M. H., Morshed, M., & Sarkar, A. K. (2015). The effect of changing substrate material and thickness on the performance of inset feed microstrip patch antenna. *American Journal of Networks and Communications*, *4*(3), 54-58.

Pozar, D. M. (1994). The active element pattern. *IEEE Transactions on Antennas and Propagation*, *42*(8), 1176-1178.

Pralon, M. G., Del Galdo, G., Landmann, M., Hein, M. A., & Thomä, R. S. (2017). Suitability of compact antenna arrays for direction-of-arrival estimation. *IEEE Transactions on Antennas and Propagation*, *65*(12), 7244-7256.

Qi, Z., Bai, Y., & Zhang, X. (2019). Synthesis of linear and planar arrays via sequential convex optimizations. *IEEE access*, *8*, 6717-6728.

Razak, N. S., & Shah, S. M. (2022). Antenna for 5G mobile communication at 28 GHz. *Journal of Electronic Voltage and Application*, *3*(1), 33-44.

Sadiq, M., bin Sulaiman, N., Isa, M. M., & Hamidon, M. N. (2022). A review on machine learning in smart antenna: Methods and techniques. *Tem Journal*, *11*(2), 695.

Saeidi-Manesh, H., Saeedi, S., & Zhang, G. (2020). Dual-polarized perpendicularly fed balanced feed antenna with high polarization purity. *IEEE Antennas and Wireless Propagation Letters*, *19*(2), 368-372.

Shan, T., Li, M., Xu, S., & Yang, F. (2021). Phase synthesis of beam-scanning reflectarray antenna based on deep learning technique. *Progress In Electromagnetics Research*, *172*, 41-49.

Shan, Y., & Li, S. (2019). Discrete spherical image representation for cnn-based inclination estimation. *IEEE access*, *8*, 2008-2022.

Shi, D., Lian, C., Cui, K., Chen, Y., & Liu, X. (2022). An intelligent antenna synthesis method based on machine learning. *IEEE Transactions on Antennas and Propagation*, *70*(7), 4965-4976.

Shi, Q., Zheng, Z., & Sun, Y. (2021). Pattern Synthesis of Subarrayed Large Linear and Planar Arrays Using $ K $-Means Solution. *IEEE Antennas and Wireless Propagation Letters*, *20*(5), 693-697.

Shrestha, A., & Mahmood, A. (2019). Review of deep learning algorithms and architectures. *IEEE access*, *7*, 53040-53065.

Singh, J., & Banerjee, R. (2019). A study on single and multi-layer perceptron neural network. 2019 3rd International Conference on Computing Methodologies and Communication (ICCMC).

Soliman, M. M., Imran, A., & Ullah, K. (2019). *Highly Efficient 2x2 Antenna Array at 28 GHz and 38 GHz for 5G Applications*.

Stanley, M., Huang, Y., Wang, H., Zhou, H., Alieldin, A., Joseph, S., Song, C., & Jia, T. (2019, 2019). A dual-band dual-polarised stacked patch antenna for 28 GHz and 39 GHz 5G millimetre-wave communication.

Stutzman, W. L., & Thiele, G. A. (2012). *Antenna theory and design*. John Wiley & Sons.

Tan, X. W. (2019). *Design of Ka-Band Reflectarray for Space*.

Tokan, N. T., & Gunes, F. (2008). Support vector characterisation of the microstrip antennas based on measurements. *Progress In Electromagnetics Research B, 5*, 49-61.

Truong, D.-H., Deneire, L., & Ferrero, F. (2019). Hybrid Beamforming for dual-polarized antenna. 2019 IEEE Wireless Communications and Networking Conference (WCNC).

Xia, X., Wu, F., Yu, C., Jiang, Z. H., Lu, R., Yao, Y., & Hong, W. (2022). Millimeter-wave±45° dual linearly polarized end-fire phased array antenna for 5G/B5G mobile terminals. *IEEE Transactions on Antennas and Propagation*, *70*(11), 10391-10404.

Yadav, R., Parmar, A., Malviya, L., & Nitnaware, D. (2021). *28 GHz Inset Feed Circular Shaped Compact Patch Antenna Array for 5G Wireless Communication*.

Yong, Z. (2019, 27-30 Oct. 2019). A Transparent Dual-Band Dual-Polarized mm-Wave Antenna Array for 5G Smartphone Application. 2019 International Symposium on Antennas and Propagation (ISAP).

Yu, L. C., & Kamarudin, M. R. (2016). Investigation of patch phase array antenna orientation at 28 GHz for 5G applications. *Procedia computer science, 86*, 47-50.

Zeng, Z., Huang, J., Song, Z., & Zhang, Q. (2015). A Novel Miniaturized Dual Slant-Polarized UWB Antenna Array with Excellent Pattern Symmetry Property for

MIMO Applications. *International Journal of Antennas and Propagation*, *2015*(1), 801638.

Zhang, Y., Jin, H., Tu, H., Zuo, Y., Luo, Q., Li, P., Chen, Z., Jia, J., & Zhang, L. (2023). The characteristic impedance calculation method of microstrip line and application in embroidered microstrip line. *Journal of Industrial Textiles*, *53*, 15280837231188525.

Zhao, Y., & Zhao, A. (2019). End-fire dual polarized 5G millimeter-wave antenna array for mobile devices. 2019 IEEE Asia-Pacific Microwave Conference (APMC).

Zhu, Y., & Deng, C. (2021). Millimeter-wave dual-polarized multibeam endfire antenna array with a small ground clearance. *IEEE Transactions on Antennas and Propagation*, *70*(1), 756-761.

PUBLICATIONS

S. Z. M. Hamzah, N. Farihah Abdul Malek, S. Yasmin Mohamad, F. Nadia Mohd Isa, T. Surya Gunawan and K. -S. Chin, "Deep Learning-Driven Beam-Steering for Dual-Polarized 28 GHz Antenna Arrays in 5G Wireless Networks," in IEEE Access, vol. 13, pp. 80680-80694, 2025, doi: 10.1109/ACCESS.2025.3566252. (Scopus & ISI-IF: 3.40 Q2)

Siti Zainab Mohd Hamzah, Norun Farihah Abdul Malek, Sarah Yasmin Mohamad, Farah Nadia Mohd Isa, "Design and Fabrication of High-Gain Dual Linearly Polarized Patch antenna at 28 GHz", Under Publish Process in progress in Malaysia-Japan Workshop on Radio Technology 2024.

Hamzah, S. Z. M., Malek, N. F. A., Ahamad, F. T., Mohamad, S. Y., & Jamaluddin, M. H. (2023, October). Reflection Coefficient Variation based on the Configuration of Integrated Antenna and Reflecting Surface at 3.5 GHz. In 2023 IEEE International Symposium on Antennas and Propagation (ISAP) (pp. 1-2). IEEE.

Hamzah, S. Z. M., Malek, N. F. A., Isa, F. N. M., Mohammad, S. Y., Azman, A. W., & Islam, M. R. (2022, July). Design of Dual-Linearly Polarized Patch Antenna at Millimetrewaves. In 2022 IEEE International Symposium on Antennas and Propagation and USNC-URSI Radio Science Meeting (AP-S/URSI) (pp. 1184-1185). IEEE.

Hamzah, S. Z. M., Malek, N. F. A., Mohammad, S. Y., Isa, F. N. M., & Islam, M. R. (2021, June). Design of circular patch antennas at mmWave. In *2021 8th International Conference on Computer and Communication Engineering (ICCCE)* (pp. 144-149). IEEE.

Siti Zainab Mohd Hamzah, Norun Farihah Abdul Malek, Sarah Yasmin Mohamad, Farah Nadia Mohd Isa, Athirah Mohd Ramly "Enhanced Performance of Millimetre-Wave Dual-Polarized Antenna Through Reduced Element Spacing" *Under Review*

APPENDICES

APPENDIX A: AEP COMPUTATION

```
opts=detectImportOptions('AEP.xlsx');
data = readmatrix('AEP.xlsx','Sheet','Sheet1','Range','B2:E73');
AEP=data(1:72,:);
XX=-175:5:180;
X=XX*pi/180;
phase=(0:20:360)*pi/180;

    W=[1,phase(:,1),1,phase(:,1),1,phase(:,1),1,phase(:,1)];
        K=2*pi;
        D=2.159;%15.6 MM
        AF1=exp((1i.*(-1.5).*K.*D.*sin(X).*cos(W(1,2))));
        AF2=exp((1i.*(-0.5).*K.*D.*sin(X).*cos(W(1,4))));
        AF3=exp((1i.*(0.5).*K.*D.*sin(X).*cos(W(1,6))));
        AF4=exp((1i.*(1.5).*K.*D.*sin(X).*cos(W(1,8))));

W1=[W(1,1)*exp(1i.*W(1,2));W(1,3)*exp(1i.*W(1,4));W(1,5)*exp(1i.*W(1,6));W(1,7
)*exp(1i.*W(1,8))];

TOTAL=(AEP(:,1).*AF1'*W1(1,1))+(AEP(:,2).*AF2'*W1(2,1))+(AEP(:,3).*AF3'*W1(3,1
))+(AEP(:,4).*AF4'*W1(4,1));

AP=abs(TOTAL)/max(abs(TOTAL));
AP=AP';

writematrix([W(1,1),W(1,3),W(1,5),W(1,7),W(1,2),W(1,4),W(1,6),W(1,8),AP],'TRAI
NINGDATA1.xlsx','Sheet',1,'Range','A2');
```

APPENDIX B: ARRAY FACTOR COMPUTATION

```
array=linearArray(NumElements=4, ElementSpacing=0.0156, PhaseShift=[25 35 45
55]);
[af,azimuth,elevation]=arrayFactor(array,28e9,elevation=0,CoordinateSystem="re
ctangular");
```

APPENDIX C: PHASE DIFFERENCE COMPUTATION

```
x=5;
x=x*pi/180;
K=2*pi;
D=2.159;
B=K.*D.*cos(x);
```

APPENDIX D: AEP-DNN COMPUTATION

```
opts=detectImportOptions('TRAININGDATA.xlsx');
data =
readmatrix('TRAININGDATA.xlsx','Sheet','Sheet1','Range','I2:CB6860');
data1 =
readmatrix('TRAININGDATA.xlsx','Sheet','Sheet1','Range','E2:H6860');
XTrain=data(:,:);
YTrain=data1(:,:);
opts=detectImportOptions('ARRAYVALIDATIONDATA.xlsx');
data2 =
readmatrix('ARRAYVALIDATIONDATA.xlsx','Sheet','Sheet1','Range','I2:CB65');
data3 =
readmatrix('ARRAYVALIDATIONDATA.xlsx','Sheet','Sheet1','Range','E2:H65');
XValidate=data2(:,:);
YValidate=data3(:,:);
opts=detectImportOptions('DNNDATA.xlsx');
data4 = readmatrix('DNNDATA.xlsx','Sheet','Sheet8','Range','J37:CC37');
data5 = readmatrix('DNNDATA.xlsx','Sheet','Sheet8','Range','F37:I37');
XTest=data4(:,:);
YTest=data5(:,:);


inputSize=72;
numResponses=4;


layers=[sequenceInputLayer(inputSize)
fullyConnectedLayer(40)
reluLayer
dropoutLayer(0.5)
fullyConnectedLayer(10)
reluLayer
dropoutLayer(0.5)
fullyConnectedLayer(numResponses)];


options=trainingOptions("adam",...
    InitialLearnRate=1e-3,...
    ValidationData={XValidate YValidate}, ...
    LearnRateSchedule="none",...
    GradientThreshold=1,...
    GradientDecayFactor=0.9,...
    SquaredGradientDecayFactor=0.99,...
    L2Regularization=1e-7,...
    MaxEpochs=2000,...
    MiniBatchSize=50,...
    Shuffle="never",...
    Verbose=true,...
    Metrics="rmse",...
    Plots="training-progress");


net=trainnet(XTrain,YTrain,layers,"mse",options);
YPredicted=minibatchpredict(net,XTest);
figure
```

```
scatter(YPredicted,YTest,"b+");
xlabel("Predicted");
ylabel("Actual")
hold on
xlim([-100 100])
ylim([-100 100])
plot([-100 100],[-100 100],"r--"
```

APPENDIX E: MEASUREMENT FIGURES

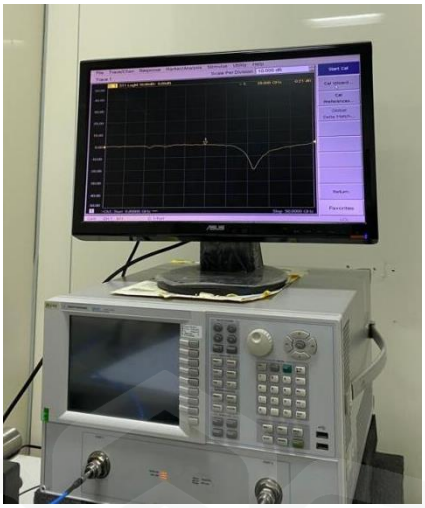

The Vector Network Analyzer at the Antenna Laboratory CGU, Taiwan

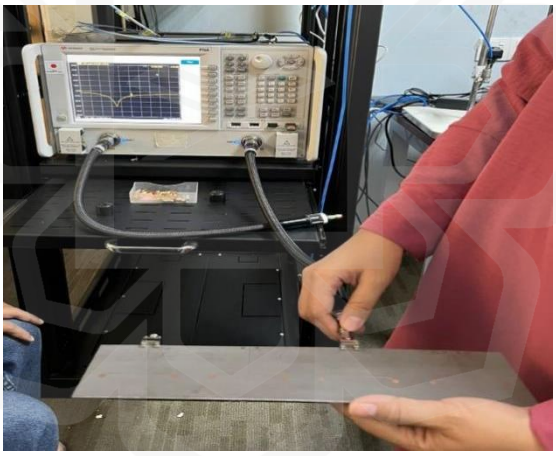

The Vector Network Analyzer at the Antenna Laboratory MJIIT UTM KL

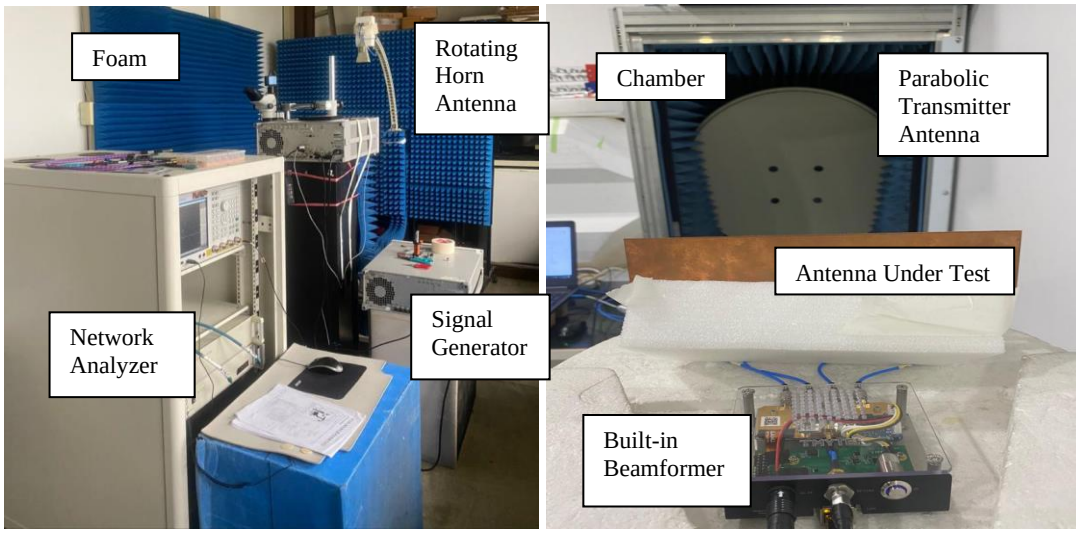

(a) (b)

(a) The Over-the-Air (OTA) and (b) the Compact Range Reflector (CATR) system

(a) (b)

(c)

The Calibration Procedures of (a) Open (b) Short and (c) Load Connectors

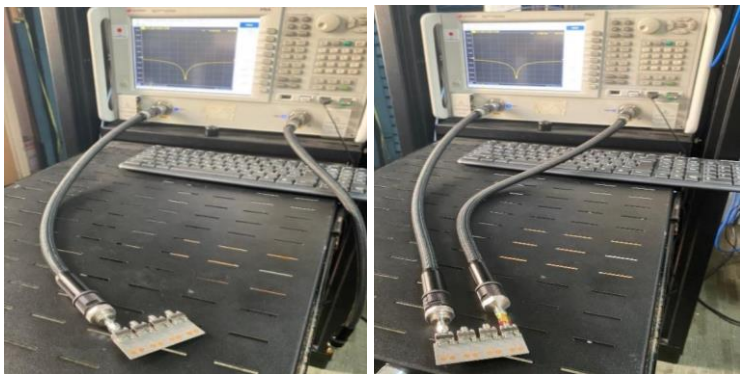

(a) (b)

The (a) S_{11} and (b) Mutual Coupling Measurement of the Proposed Antenna Array using VNA

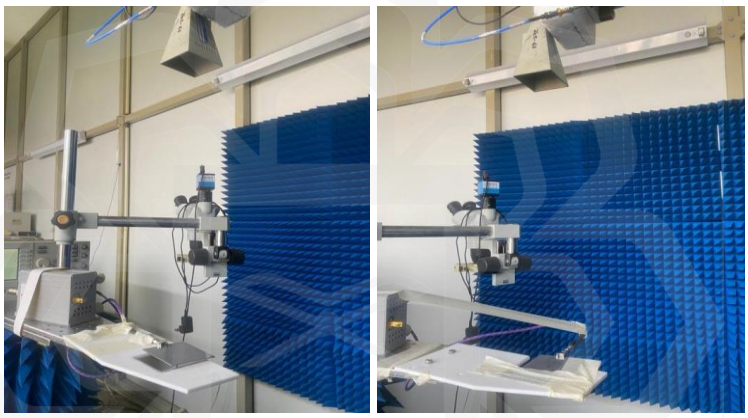

(a) (b)

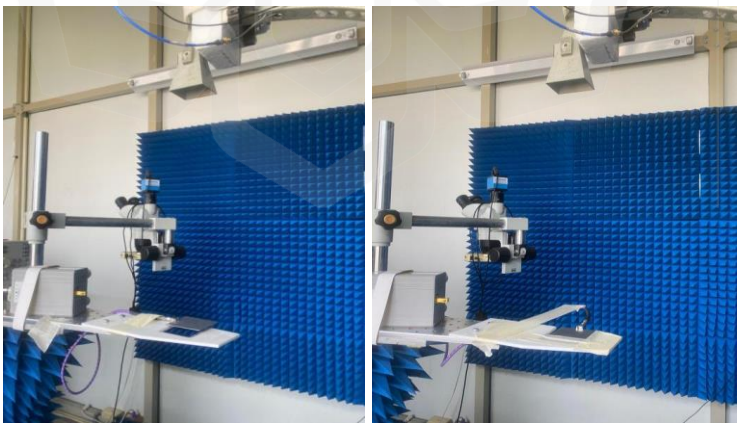

(c) (d)

An Example of an Antenna Measurement Setup at the Antenna Laboratory, Chang Gung University, Taiwan of (a) E-Plane Co-Polarised (b) H-Plane Co-Polarised (c) E-Plane Cross-Polarised (d) H-Plane Cross-Polarised of a slanted +45° Single Antenna

The Transmitter Horn Antenna (26.5-40 GHz)

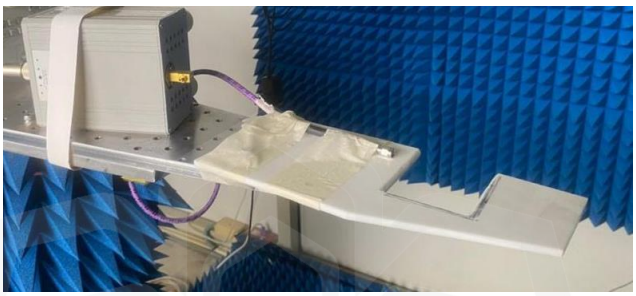

The Antenna Holder

The RF Signal Generators (E8257DSG)

The RF Microwave Absorber Pyramidal Foam Cones

The Mixer (11970A)

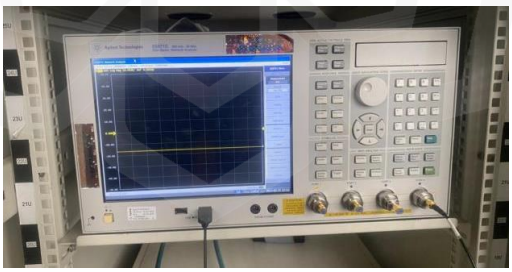

The E5071C Network Analyzer

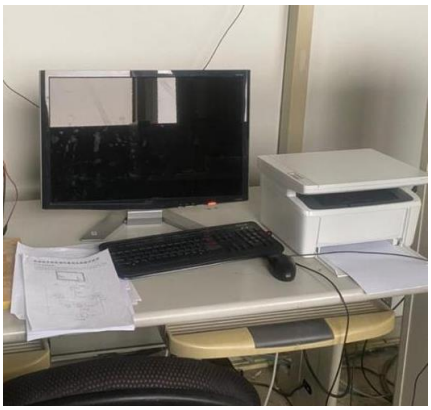

The Computer

The Whole Antenna Measurement Setup

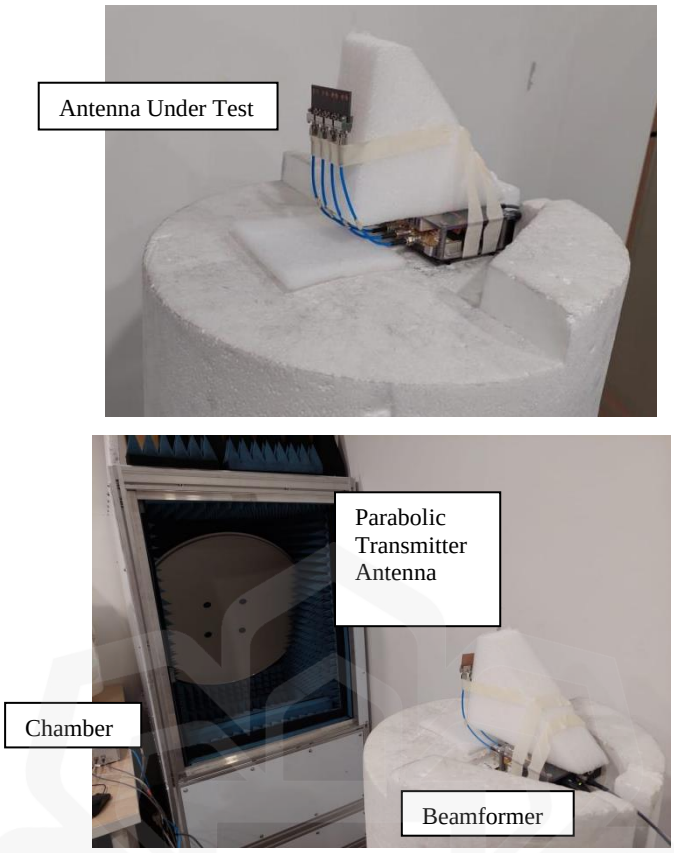

The Proposed Antenna Array Pattern Measurement Setup

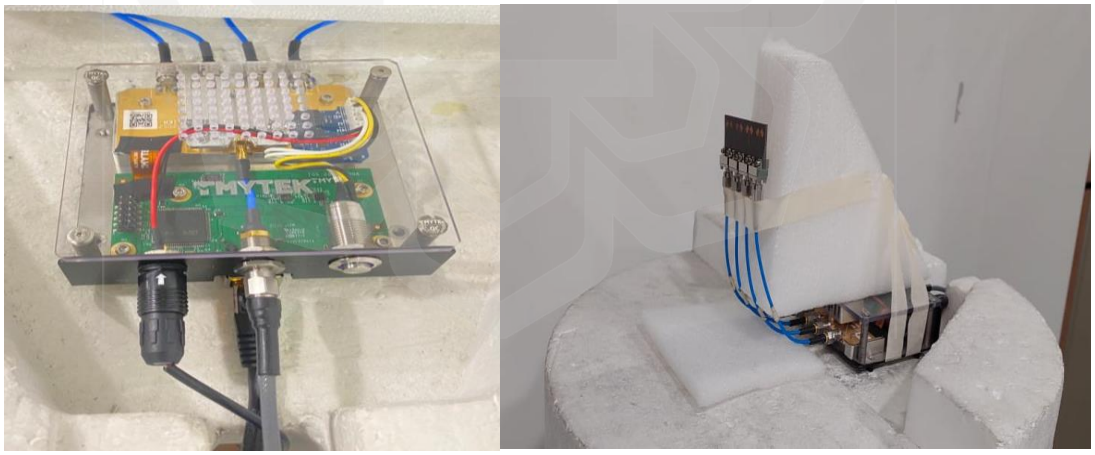

(a) (b)

(a) The Top View and (b) the Connection of the Proposed DLPAA with the Built-in Beamformer